

Helsinki University of Technology
Department of Electrical and Communications Engineering
Radio Laboratory

Studies on Specular and Non-specular Reflectivities of Radar Absorbing Materials (RAM) at Submillimetre Wavelengths

Jussi Säily, Antti V. Räsänen

Report S 258
February 2003

Abstract

The absorbing material studies presented in this Report are related to an ongoing project at the HUT Radio Laboratory for realising a submillimetre wave compact antenna test range (CATR) based on a hologram. Absorbing materials are needed in all indoor antenna test ranges, and an accurate knowledge of their properties is required for effective placement inside the range.

Measurements of both specular and non-specular scattering from several submillimetre wave absorber materials and low-cost carpet materials are presented. The carpets were included in the tests because some earlier publications noted that they can be used in non-critical areas to reduce material cost. The frequency range in specular scattering is 200–600 GHz, and 300–400 GHz in non-specular scattering measurements. The constructed bistatic test bench allows automatic testing of the full continuous angular range of 0° – 90° .

The measurement results show large differences in performance between materials. The best specular performance of -50 dB was measured for the pyramidal TK THz RAM. However, the same material scatters considerable amounts of power into non-specular angles. The scattered power from wedged-type TERASORB-500 and FIRAM-500 materials is concentrated close to the specular direction, and very little power is found at other angles if the wedges are properly oriented. Low-cost carpet materials have better than -15 dB reflectivities in most angles, and are very useful in the non-critical areas of the antenna range. The results presented in this Report can be used to optimise the absorber placement inside the antenna range, concerning both maximum performance and lowest cost.

Contents

ABSTRACT.....	2
CONTENTS	3
1 INTRODUCTION.....	4
2 DESIGN OF RADAR ABSORBING MATERIALS (RAM).....	5
2.1 INTRODUCTION	5
2.2 LOSS MECHANISMS.....	5
2.3 SINGLE-LAYER ABSORBERS	7
2.3.1 <i>The Salisbury screen and the Dällenbach layer</i>	7
2.4 MULTILAYER AND GEOMETRICAL TRANSITION ABSORBERS	8
2.4.1 <i>The Jaumann absorber</i>	8
2.4.2 <i>Graded dielectric absorbers</i>	9
2.4.3 <i>Geometrical transition absorbers</i>	9
2.5 OTHER TYPES OF RAM	9
3 SCATTERING THEORY	11
3.1 DEFINITION OF THE RADAR CROSS SECTION (RCS)	11
3.2 RAYLEIGH, RESONANT, AND OPTICS SCATTERING REGIONS	11
3.3 SIMULATION METHODS FOR SOLVING SCATTERING PROBLEMS.....	13
4 SPECULAR REFLECTIVITY MEASUREMENTS AT 200–600 GHZ	16
4.1 OVERVIEW OF THE TESTED MATERIAL SAMPLES	16
4.2 CONSTRUCTION OF THE TEST BENCH	19
4.3 MEASUREMENT RESULTS	21
4.3.1 <i>Measured reflectivities for the materials</i>	21
4.3.2 <i>Effect of non-idealities</i>	34
4.3.2.1 <i>Direct coupling between the horn antennas</i>	34
4.3.2.2 <i>Dynamic range limitations at 500 and 600 GHz</i>	34
4.3.2.3 <i>Pointing errors</i>	35
5 NON-SPECULAR REFLECTIVITY MEASUREMENTS AT	36
300–400 GHZ.....	36
5.1 CONSTRUCTION OF THE TEST BENCH	36
5.2 MEASUREMENT RESULTS	37
5.2.1 <i>Measured reflectivities for the materials</i>	37
5.2.2 <i>Effect of non-idealities</i>	53
5.2.2.1 <i>Direct coupling between the horn antennas</i>	53
5.2.2.2 <i>Pointing errors</i>	53
5.2.2.3 <i>Effect of the receiver’s distance on the results</i>	53
6 SUMMARY AND CONCLUSIONS.....	55
ACKNOWLEDGMENTS	57
REFERENCES.....	58

1 Introduction

High performance radar absorbing materials (RAM) are needed for antenna measurement ranges operating across different frequency bands. The commonly used indoor antenna test facilities include the compact antenna test range (CATR) and the various near-field scanners [1]. RAM materials are also used in quasioptical systems as beam dumps and black body calibration sources. The radar cross section (RCS) of military aircrafts and other targets [2,3] can be reduced by applying suitable RAM sheets in their structures.

Common requirements for the RAM materials are low reflectance (-30...-40 dB) over the operating frequency range and all angles of incidence, low evolution of dust and vapours, low weight, and no damage with light handling [1]. Vacuum compatibility of the RAM is also required in some space-borne instruments.

A literature search on the subject revealed that in the open literature only a few published results exist concerning submillimetre wave absorber materials [4–8]. Moreover, some of the reported studies were carried out either at a single frequency [6,7] or for a single material [4].

The purpose of the study presented in this report is to thoroughly characterise a set of suitable absorber materials for use in a large-sized submillimetre wave CATR facility. The results will be used in selecting suitable materials for the test range and as input data for a software that optimises the placement of absorbers inside the range. The material samples have been characterised across the frequency range of 200–600 GHz for specular and 300–400 GHz for non-specular reflectivities. In the bistatic specular reflectivity measurement setup, both the incident and receiving angles are swept continuously. In the bistatic non-specular measurement setup, the receiving angle is continuously swept for three different incident angles.

Chapter 2 discusses the design of RAM materials. Chapter 3 contains an introduction to scattering theory. A brief review of simulation methods for solving scattering problems serves merely as a starting point and tool for a possible future study aiming to improved performance of RAM materials. The specular reflectivity measurements at 200–600 GHz are presented in Chapter 4, and the non-specular measurements in Chapter 5. Summary and conclusions are in Chapter 6.

2 Design of radar absorbing materials (RAM)

2.1 Introduction

Radar absorbing materials (RAM) are commonly used to minimize electromagnetic scattering in various antenna test facilities, test equipment, and military targets. The RAM material should reflect the incident EM radiation as little as possible and provide sufficient loss within the allowed thickness. It must also operate over a broad frequency range. Basically, the RAM is a distributed lossy network, matching the free space impedance to the absorber material or to a conducting metal body behind it.

The RAM materials are typically designed to reduce reflections either in the specular or the non-specular directions. The absorber sheets are usually composites of dielectric and magnetic materials [2]. The different loss mechanisms involved in both specular and non-specular RAM design are discussed in the next section.

2.2 Loss mechanisms

Lossy materials attenuate electromagnetic waves that pass through them. This can be modeled with the refraction index, relative permittivity, or relative permeability which are all complex numbers. The imaginary component causes the loss in the material. Physically, the absorbed power is converted into heat. In practical engineering applications where only the cumulative loss is of interest, the different loss mechanisms are combined into one set of normalised complex permittivity and permeability values ϵ_r and μ_r , given as [2]

$$\epsilon_r = \epsilon_r' + j\epsilon_r'' \quad (2.1)$$

$$\mu_r = \mu_r' + j\mu_r'' \quad (2.2)$$

In the above equations, the real parts showing the energy storage are denoted by single primes, and the complex parts showing the loss with double primes. If we specify the electric and magnetic loss tangents as [2]

$$\tan \delta = \frac{\epsilon_r''}{\epsilon_r'} \quad (\text{electric}) \quad (2.3)$$

$$\tan \delta_m = \frac{\mu_r''}{\mu_r'} \quad (\text{magnetic}) \quad (2.4)$$

equations (2.1) and (2.2) can be written in polar form as

$$\epsilon_r = |\epsilon_r| e^{j\delta} \quad (2.5)$$

$$\mu_r = |\mu_r| e^{j\delta_m} \quad (2.6)$$

The refraction index between free-space and a lossy material is

$$n = k / k_0 = \sqrt{\mu_r \epsilon_r}, \quad (2.7)$$

where k and $k_0 = 2\pi f \sqrt{\mu_0 \epsilon_0}$ are the wavenumbers in a lossy material and in free space, respectively. If $Z_0 = 120\pi$ is the free-space impedance, the intrinsic impedance of a material with $\epsilon_r \neq 1$ and/or $\mu_r \neq 1$ can be defined as

$$Z = Z_0 \sqrt{\frac{\mu_r}{\epsilon_r}}. \quad (2.8)$$

For normal incidence, the reflection coefficient of the material interface is calculated as

$$R = \frac{Z - Z_0}{Z + Z_0} = \frac{Z / Z_0 - 1}{Z / Z_0 + 1}. \quad (2.9)$$

In many practical applications, the dielectric absorbing material (with thickness d) has a metal backing, and its normalised input impedance (for normal incidence) can be shown to be [2]

$$Z_{mb} = \sqrt{\frac{\mu_r}{\epsilon_r}} \tanh(-jk_0 d \sqrt{\mu_r \epsilon_r}). \quad (2.10)$$

In most cases we are only interested in the amplitude of the reflection coefficient in decibels, i.e.,

$$|R| \text{ (dB)} = 20 \log |R|. \quad (2.11)$$

However, the phase angle of R is important in some narrowband RAM applications where resonant energy cancellation is used.

The design of a RAM is a compromise between the front-face reflection coefficient and the loss per unit thickness. If low reflection is desired, then the material thickness will become large in wavelengths. In practice, multilayer structures are used to obtain the desired loss and low reflection inside the RAM sheet. These along with the use of geometrical transitions are discussed in Section 2.4.

Scattering into non-specular directions is caused by surface traveling waves, edge waves, creeping waves, and diffraction from edges and non-continuities like gaps and cracks in the material [2]. The optical analogies present in specular scattering do not apply to non-specular returns. The non-specular returns can be addressed by applying magnetic and dielectric coatings to reduce surface currents, and by the use of tapered resistive strips to attenuate edge diffractions and control the non-specular sidelobes. Since these techniques are difficult to apply at submillimetre wavelengths, they are not discussed in more detail in this report, and the interested reader is directed to reference [2].

2.3 Single-layer absorbers

2.3.1 The Salisbury screen and the Dällenbach layer

The simplest form of RAM is the single layer resonant absorber like the Salisbury screen and the Dällenbach layer (Figure 2.1) [2]. In the Salisbury screen, a thin sheet of resistive material is separated from the metal backing by a foam or honeycomb dielectric spacer with a thickness of d . Typical permittivity of the spacer is close to that of free-space, i.e. $\epsilon_r \approx 1$. The Salisbury screen can be analysed with transmission line analogy. It can be shown [2] that the Salisbury screen works as a perfect absorber (no power is reflected) for normal incidence, if the sheet resistance of the infinitely thin resistive sheet is $377 \Omega/\text{sq}$ (same as the free space impedance) and the spacer thickness is an odd multiple of the quarter wavelength, i.e.

$$d = \frac{\lambda}{4} + \frac{n\lambda}{2}, \quad n = 0, 1, 2, \dots \quad (2.12)$$

Similarly, the Salisbury screen works as a perfect reflector for thicknesses that are multiples of half wavelength. The reflectivity of the structure increases for non-normal incidences, and can provide reflectivities below -20 dB for off-normal angles of up to 35° . Practical applications of the simple Salisbury screen are nominal because of its narrowband nature, but has effectively been used as part of multilayer absorbers [9–13] at microwaves. No publications of submillimetre use of Salisbury screens were found in the open literature.

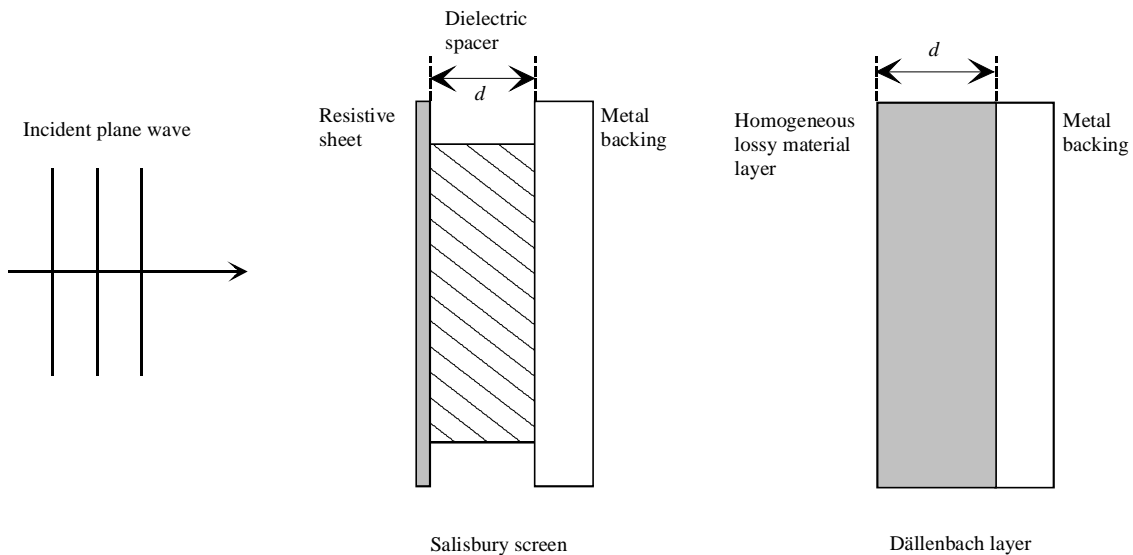


Figure 2.1 Single layer resonant absorbers: the Salisbury screen and the Dällenbach layer.

The Dällenbach layer consists of a layer of homogeneous lossy material on top of the metal backing. The reflection at the material surface occurs due to the impedance mismatch between free space and the material's intrinsic impedance according to equation (2.9) for normal incidence. It is evident from (2.8) that if a material with $\mu_r =$

ε_r can be found, no reflection will occur at the interface. For normal incidence, the reflection coefficient of the metal-backed Dällenbach layer is found by substituting the normalised input impedance $Z_{mb} = Z/Z_0$ from (2.10) into (2.9):

$$R = \frac{\sqrt{\mu_r / \varepsilon_r} \tanh(-jkd) - 1}{\sqrt{\mu_r / \varepsilon_r} \tanh(-jkd) + 1}. \quad (2.13)$$

Dällenbach layers have many applications at submillimetre wavelengths, e.g. in RAM, quasioptical beam dumps, and emitting surfaces for black body radiation sources. Design of submillimetre Dällenbach-type RAM materials using artificial dielectric coatings constructed from metal flake loaded resins (like vinyl acetate, silicone, and polyurethane) is described in [6]. The coatings exhibit optical properties of homogeneous media because of the small size of the metal flakes compared to the wavelength. Measurement results of the coatings across 300–3000 GHz indicate that the layers can be optimized for any frequency in the THz range with the developed heuristic models. For example, a reflectivity of -27 dB was obtained at 584 GHz with normal incidence. Performance of the Dällenbach layers for non-normal incidences is not described in [6].

A more recent study on the properties of single and multilayer absorbing coatings is described in [8]. In the study, the dielectric layers are loaded with SiC (silicon carbide) grains of different sizes. The specular and non-specular reflectivities across 300–3000 GHz are compared with commercial absorbing materials Marconi LAO5 and Thomas Keating’s THz RAM. The reflectivity of the absorbing coatings increases with increasing wavelength, angle of incidence, and diminishing surface roughness. In this study, no reflectivity modelling of the layers is attempted. A large batch of test samples have been manufactured with different surface paints, layer thicknesses and combinations, and SiC grain sizes.

2.4 Multilayer and geometrical transition absorbers

The operating bandwidth of single layer absorbers can be extended by applying two or more layers. The idea is to provide a slowly changing effective impedance profile with distance into the material. The most important multilayer types are the Jaumann and graded dielectric absorbers [2]. Also the geometrical transition absorbers like pyramidal, wedge, and convoluted absorbers provide a smooth effective impedance profile for the incident wave.

2.4.1 The Jaumann absorber

The Jaumann absorber is a modification of the Salisbury screen having multiple thin resistive layers separated with spacers on top of the metal backing. The cost of the increased bandwidth is the increased thickness of the absorber. The resistivity of the layers should vary from high at the front face to low at the back. Examples of realised microwave Jaumann absorbers are found e.g. in [11] and [12]. The reported

reflectivity in incidence angles of $0\text{--}60^\circ$ for a four-layer Jaumann absorber in [12] is below -20 dB across $4\text{--}17$ GHz.

At short millimetre wavelengths, however, producing thin homogeneous and isotropic dielectric layers is very difficult, and the performance of Jaumann absorbers is likely to be worse. Submillimetre wave applications of Jaumann absorbers are not described in the open literature.

2.4.2 Graded dielectric absorbers

The graded dielectric absorbers use a tapered conductivity value with distance into the material. Different tapering models including linear and exponential, or discrete layers can be used [2]. Commercial graded dielectric absorbers are available e.g. from Emerson & Cuming Microwave Co. with a conductivity gradient (Eccosorb HR-series $5\text{--}27$ GHz), and with discrete sandwiched layers of different conductivity (Eccosorb AN-series $0.6\text{--}40$ GHz) [14]. The THz-range multilayer absorbing coatings developed and tested in [8] are, in effect, graded dielectric absorbers made by applying several dielectric layers on top of each other.

2.4.3 Geometrical transition absorbers

The geometrical transition absorbers are a subset of graded dielectric absorbers. They use a geometrical transition as the effective dielectric gradient from free space to the lossy material. The commonly used geometries include pyramidal, convoluted, and wedged surfaces. Reflectivity performance of the geometrical transition absorbers can be different for other polarisations. The pyramidal and convoluted absorbers work equally well with both horizontal and vertical polarisations, but the wedged absorber requires the polarisation to be along the groove direction for optimum performance. Broadband millimetre wave RAM materials with guaranteed reflectivities below -50 dB upto 100 GHz are commercially available e.g. from Emerson&Cuming Microwave Co. [15].

The measured reflectivities of some commercially available pyramidal and wedged absorbers specially developed for submillimetre wave applications are shown in Chapters 4 and 5 of this report.

2.5 Other types of RAM

In addition to the widely used RAM types discussed above, several other types intended for use in special applications exist. The design methodology for specular RAM uses transmission line analogy to match the incoming wave to the metal backing. By using resistive sheets in Salisbury and Jaumann type materials, only the real part of their admittance can be used in matching. More flexibility in the design can be achieved if the imaginary part of the admittance (susceptance) can also be tailored. This can be done by replacing the continuous resistive sheet with a specially patterned surface [2]. In the so-called circuit analog RAM, the geometrical patterns

(dipoles, crosses, triangles, etc.) are described in terms of their resistance, capacitance, and inductance. With circuit analog RAM, significant improvements in both the bandwidth and absorption compared to the Salisbury and Jaumann absorbers can be achieved. The penalty is that the optimisation of the patterns is a complex and time consuming task.

Another application of the circuit analog patterns is the so-called frequency-selective surface (FSS). The FSS consists of conductive patterns placed on dielectric medium. By using materials with different conductivities, the FSS can be used for making absorbers, bandpass, or bandstop filters. Applications of FSS filters are in e.g. antenna radomes and dual-frequency antenna duplexers [2]. The design and measurement results across 5–18 GHz for a FSS deposited on a Dällenbach layer are described in [13]. The added FSS layer facilitated wider absorption bandwidth compared to the single Dällenbach layer, and with minimal added thickness. A more complex absorbing structure based on an embedded FSS layer inside dielectric media is described in [16]. The design of the composite material comprising of four dielectric layers and one FSS layer is done by using a binary-coded genetic algorithm. The simulations across 19–36 GHz predict reflectivities between $-30\dots-40$ dB for normal incidence and $-18\dots-34$ dB for an incidence angle of 45° .

Instead of using only electric loss, also magnetic loss can be used in absorbing materials as indicated in (2.4). Absorbing materials with relative permeabilities differing from that of free space are referred to as magnetic RAM [2]. The practical RAM materials consist of dielectric material loaded with small particles having magnetic properties. The magnetic materials most commonly used are carbonyl iron and ferrites like iron oxide. The magnetic RAM materials are especially useful at low frequencies because of the close to 1/10 reduction in thickness compared to ordinary absorbers. Commercial magnetically loaded RAM are available e.g. from Emerson & Cuming Microwave Co. for 0.8–30 GHz in the Eccosorb series of absorbers [14]. The FIRAM-500 submillimetre wave absorber manufactured by Lowell Research Foundation is also made by applying magnetic iron oxide particles in silicon [6], although the dielectric losses are the main loss mechanism at high frequencies.

A combination of two or more basic absorber types is usually referred to as a hybrid RAM [2]. The FSS/Dällenbach composite mentioned above is essentially a hybrid RAM structure. Hybrid RAM materials can achieve better absorption performance with given thickness constraints. The term radar absorbing structure (RAS) is sometimes used to describe embedded absorbers in e.g. military vehicles, where the RAM is an integral part of the structure and not just a lossy paint.

3 Scattering theory

3.1 Definition of the radar cross section (RCS)

The radar cross section (RCS) is a measure of a target's reflectivity in a given direction [2,3]. RCS is normalised to the incident power at the target, and it is independent of the power and distance of the transmitter. Furthermore, RCS does not depend on the sensitivity and distance of the receiver. Assuming far-field conditions, RCS or σ of a target (in units of square meters) can be presented as

$$\sigma = 4\pi R^2 \frac{P_s}{P_i}, \quad (3.1)$$

where R is the distance (assumed very large or infinite) of the measurement point P from the target, P_s the scattered power density due to the target, and P_i the incident power density at the target [2]. Practically, the radar cross section is a function of the angular orientation of the transmitter relative to the target, target geometry and composition, wavelength, and the polarisation of the transmitted signal.

Three different cross section definitions based on the radar system geometry are commonly used: the monostatic or backscatter, bistatic, and forward cross sections [2]. The monostatic cross section is the usual case in radar systems, where the same antenna is used by both the transmitter and the receiver. In the monostatic case, only a single set of angular coordinates is required. In the case of bistatic cross section, the transmitter and receiver antennas are located in separate places, and the angular locations of both relative to the target must be specified. The absorber reflectivity measurements reported later in this study are based on the bistatic principle. Finally, the forward cross section is defined as the measure of scattered power along the direction of incidence.

3.2 Rayleigh, resonant, and optics scattering regions

The scattering process which takes place when an electromagnetic wave encounters a material object can be characterized in two ways [2]. The simple specular reflection model assumes that the angle of incidence is the same as the angle of reflection. A more general (and physical) approach is to consider the interaction in detail, involving induced charges and currents on the object. The incident waves induce charges and currents on the surface that re-radiate electromagnetic fields which can emanate also into non-specular directions.

Generally, when an electromagnetic wave propagating in free space encounters different media characterized by ϵ and μ , energy is reflected, transmitted or absorbed. Calculation of the scattered fields requires solving of the Maxwell equations, and analytical solutions exist only for some simple surfaces like cylinders and spheres. However, powerful numerical methods are available, and these are discussed in the next section. An introduction to the theory of electromagnetic scattering can be found in [17].

Three characteristic scattering regions can be distinguished depending on the ratio of wavelength to object size: Rayleigh, resonant, and optics scattering regions. These regions and the associated scattering mechanisms are illustrated in Figure 3.1 [2]. In the figure, the normalized RCS of a metallic sphere (radius = a) as a function of its circumference in wavelengths is shown.

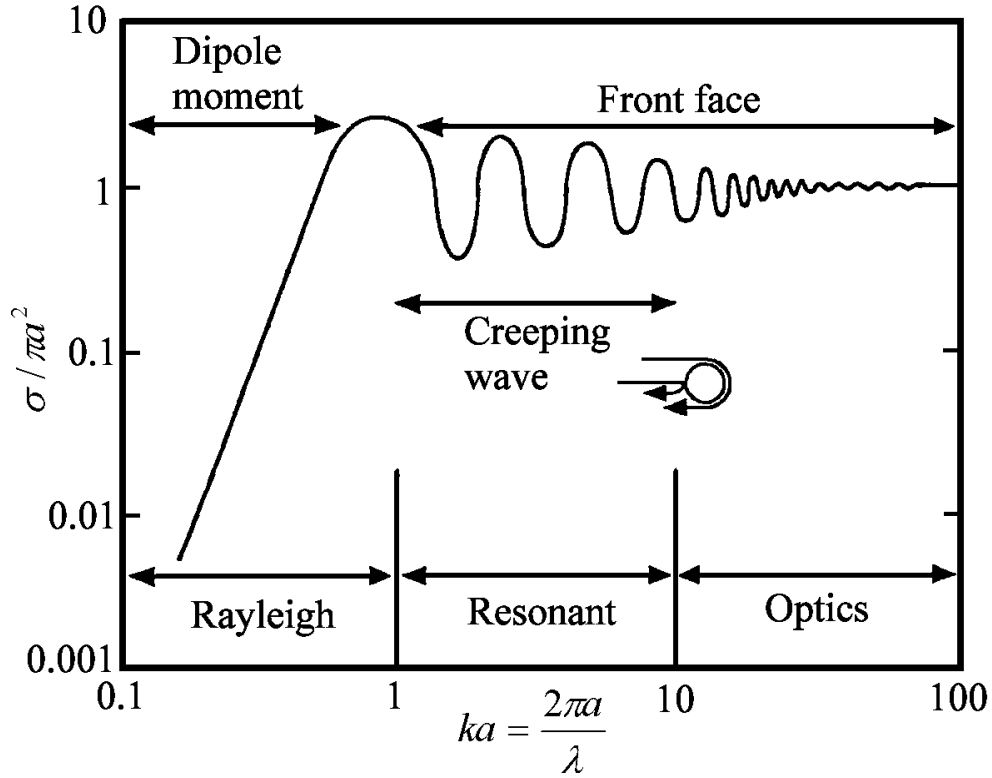


Figure 3.1 Normalized RCS of a metallic sphere (radius = a) as a function of its circumference in wavelengths [2].

The region where the wavelength λ of the incident electromagnetic wave is considerably larger than the object size L , i.e., $\lambda \gg L$, is called the low-frequency or Rayleigh scattering region [2,17]. In this case, the phase of the incident field over the object surface can be considered to be the same at each time instant. The dominant scattering mechanism in the Rayleigh region is induced dipole moment scattering. The strengths of the induced dipole moments and thus the scattered fields depend on the size and orientation of the object with respect to the incident vector electromagnetic field. Characteristics of the Rayleigh scattering are that the scattering cross-section is proportional to the fourth power of the frequency, and that it does not depend on the object's detailed shape [2]. Rayleigh scattering problems can be solved with the scalar analysis methods developed for electrostatics. Rayleigh scattering is of little practical interest to most applied electromagnetic problems, because usually the objects are large measured in wavelengths.

In the resonant scattering region, where the wavelength is comparable to the object's dimension, i.e., $L \leq \lambda \leq 10 L$, surface wave and front-face optics-like scattering

mechanisms dominate [2]. The surface wave types present are traveling, creeping, and edge traveling waves. Surface wave scattering is relatively independent of the objects size, and the scattering cross-section produced is proportional to the square of frequency. Also, the overall geometry of the object has a great effect on the observed scattered fields in this region, since the field at any part of the object surface is a sum of the incident field and the scattered fields from any other part of the object. The optics-like scattering occurs in the specular direction from the objects front-face. Calculation of the scattered fields in the resonant region requires an exact solution of the Maxwell's equations [2]. As mentioned earlier, analytical solutions exist only for simple, separable geometries, and numerical methods like the method of moments discussed in Section 3.3.2 must be used for any realistic object surface.

The optics scattering region begins when the wavelength becomes much smaller than the objects dimensions, i.e., $\lambda < 10 L$. In this region, scattering from individual local scattering centers due to detailed object surface geometry dominates [2]. The observed scattered field is a complex sum of the contributions from the individual scattering centers. The dominant scattering mechanisms in the optics region are specular (mirror-like) scattering, end-region scattering, edge diffraction, and multiple-bouncing. Specular scattering is the major scattering mechanism for many radar targets [2].

3.3 Simulation methods for solving scattering problems

Modeling of scattering problems usually involve objects of arbitrary geometry in free space. An integral equation formulation of the Maxwell's equations in conjunction with the free-space Green's function has been found convenient for solving scattered field problems. Equations (3.2) – (3.3) are called the Stratton-Chu equations. The free-space Green's function is given in (3.4).

The Stratton-Chu equation for scattered electric field (electric field integral equation, EFIE) is [2]

$$\begin{aligned} \bar{E}^s = \int_V \left(-j\omega\mu\bar{J}\psi - \bar{M} \times \nabla\psi + \frac{\rho}{\epsilon} \nabla\psi \right) dV \\ + \oint_S \left[-j\omega\mu(\hat{n} \times \bar{H})\psi + (\hat{n} \times \bar{E}) \times \nabla\psi + (\hat{n} \cdot \bar{E}) \nabla\psi \right] dS. \end{aligned} \quad (3.2)$$

Correspondingly, the equation for scattered magnetic field (magnetic field integral equation, MFIE) is

$$\begin{aligned} \bar{H}^s = \int_V \left(-j\omega\epsilon\bar{M}\psi + \bar{J} \times \nabla\psi + \frac{\rho^*}{\mu} \nabla\psi \right) dV \\ - \oint_S \left[-j\omega\epsilon(\hat{n} \times \bar{E})\psi - (\hat{n} \times \bar{H}) \times \nabla\psi - (\hat{n} \cdot \bar{H}) \nabla\psi \right] dS. \end{aligned} \quad (3.3)$$

In equations (3.2) and (3.3), \bar{J} is the electric current density, ρ the electric charge density, \bar{M} the fictitious magnetic current density, ρ^* the fictitious magnetic charge

density, \hat{n} the surface unit normal vector, and $\hat{n} \times \bar{E}$ and $\hat{n} \times \bar{H}$ the tangential electric and magnetic fields on the surface. The free-space Green's function is

$$\psi = \frac{e^{-j\bar{k} \cdot \bar{R}_{fs}}}{4\pi|\bar{R}_{fs}|}, \quad (3.4)$$

where \bar{k} is the wave vector, and \bar{R}_{fs} the vector between field and source points.

In the resonant scattering region, the Stratton-Chu integral equations are usually solved by numerical methods like the method of moments (MoM). In the optics scattering region, where the object is large in wavelengths, the required MoM-matrices quickly become too large for even the most modern computers with several gigabytes of memory. A commonly used method is the so-called physical optics (PO) approximation of the Stratton-Chu equations. PO can overcome the memory limitations of MoM, when the approximation is valid. Another possibility of calculating an exact solution for the Maxwell's equations is to use time domain differential equation methods, like the finite difference time domain (FDTD) method [2]. A useful comparison of different computational methods for electromagnetics and their application areas can be found in [18].

The method of moments is a technique for solving integral equations, e.g. the Stratton-Chu equations in the frequency domain. In MoM, the object surface is divided into small enough patches, so that the phase of the induced currents are constant on each patch [2,17]. A practical value is in the order of 7–10 patches per wavelength. Interactions between all the patches relative to each other are calculated in a matrix. The MoM system matrix depends on frequency and the objects geometry. Once the matrix has been computed and solved at one frequency, the surface currents can be calculated for any angle of incidence by simple back-substitution. Each new frequency requires formulation and solving of the matrix, however. MoM is especially suitable for resonant scattering region calculations, since it is able to accurately predict the surface wave scattering phenomena. However, the matrix size and the number of calculations required quickly escalate with increasing object size to wavelength ratio. Commercial software packages which use MoM include Agilent Technologies' ADS (Momentum) and EM Software & Systems' FEKO.

In the optics scattering region, the MoM system matrix and the number of calculations become very large when the object size is large in wavelengths. Solving of the Stratton-Chu integrals (3.2) and (3.3) can be made easier by applying the physical optics (PO) approximation. In PO, the tangent plane approximation is used, i.e., the surface fields of individual surface patches have the values they would have if the surface was perfectly smooth and flat [2,18]. The total scattered far-field is calculated by integrating the fields generated by all the individual scatterer patches. PO is inherently a high frequency approximation, and no interactions between the individual scattering patches are calculated. Also, the edge diffraction and surface traveling wave effects are not predicted by PO. The non-modeled edge diffraction causes the calculated scattered field to be increasingly erroneous when moving away from the specular direction. Extensions for the PO method exist allowing modeling of the edge currents and the surface wave effects [2]. More optics or ray-like approximations for

predicting scattering fields exist, like the geometrical theory of diffraction (GTD) [19] and the uniform theory of diffraction (UTD) [20]. Sometimes a hybrid method like MoM/PO or MoM/UTD gives accurate enough results within a reasonable time. In the hybrid methods, the critical parts of the object (like antennas) are modeled with MoM and the less-critical with the other method. Like in all computer simulations, understanding of the problem and the underlying assumptions of the simulation methods is essential for obtaining accurate results.

4 SPECULAR REFLECTIVITY MEASUREMENTS AT 200–600 GHz

4.1 Overview of the tested material samples

The tested materials include three commercially available submillimetre wave absorbers (TK THz RAM, FIRAM-500, TERASORB-500), a high performance millimetre wave absorber (Eccosorb VFX-NRL-2), and four wool and synthetic floor carpet materials for comparison. The floor carpet materials were included in the tests encouraged by the good results at 500 GHz obtained earlier in [6]. The sample dimensions in the plane of rotation are all close to 10 cm.

The wedged-type absorbers FIRAM-500 and TERASORB-500 manufactured by the Lowell Research Foundation in the USA are shown in Figure 4.1. The FIRAM-500 is made from iron oxide loaded silicon rubber by injection molding and has a thickness of 7.6 mm. The TERASORB-500 is made of carbon loaded EVA (ethylene vinyl acetate) with injection molding and has a thickness of 7.6 mm. The opening angle in both materials is 22.5° , with groove spacings of 1.55 mm, and groove depths of 3.8 mm. The opening angle is designed so that a plane wave with normal incidence encounters 8 surfaces before backscattering to the receiver [6]. The FIRAM-500 is available as sheets of $61 \times 61 \text{ cm}^2$ (2' x 2'), and the TERASORB-500 as interlocking tiles sized $10 \times 10 \text{ cm}^2$ (4'' x 4'').

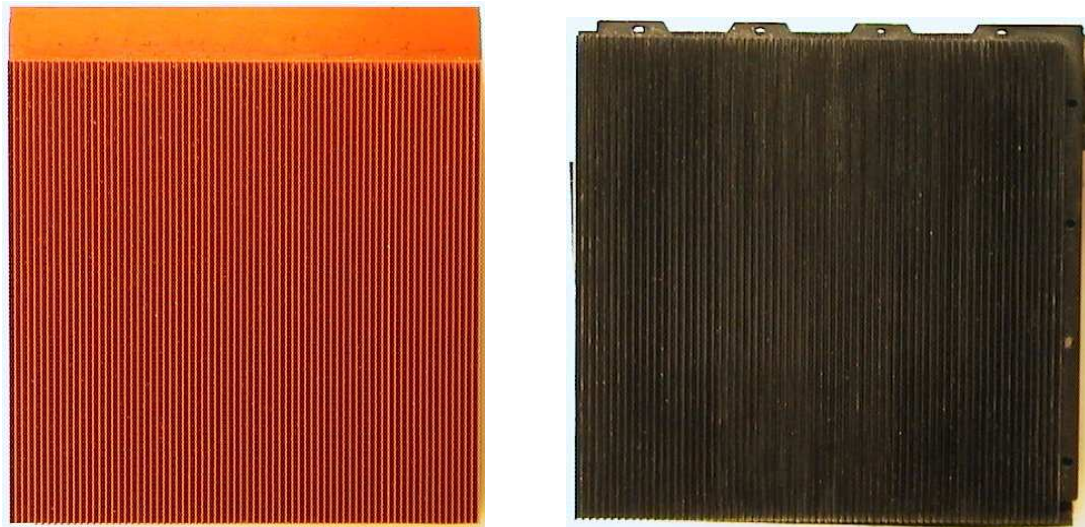


Figure 4.1 Wedged-type absorbers FIRAM-500 (left) and TERASORB-500 (right).

The $10 \times 10 \text{ cm}^2$ test sample created by joining 16 pieces of TK THz RAM pyramidal absorbers manufactured by Thomas Keating Engineering Physics, Inc. in the UK is shown in the left side of Figure 4.2. Each tile consists of 25×25 small pyramids with heights of about 1.5 mm and spacing of 1.0 mm. The opening angle is thus close to 33.7° . The absorbers are manufactured by injection molding from carbon loaded polypropylene plastic. The size of the interlocking tile is $2.5 \times 2.5 \text{ cm}^2$, with a thickness of 7.5 mm.

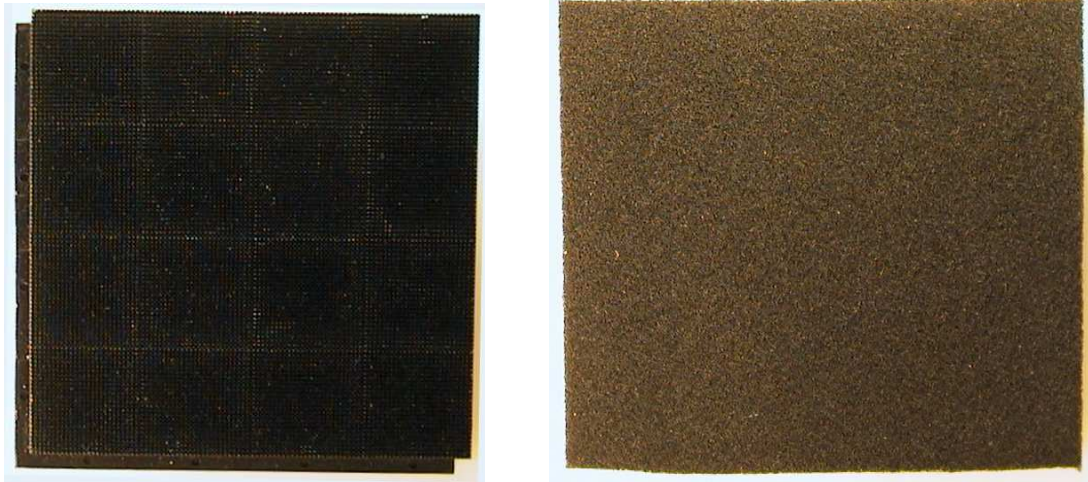


Figure 4.2 Pyramidal absorber TK THz RAM (left) and the flat side of Eccosorb VFX-NRL-2 (right).

The Eccosorb VFX-NRL-2 is a pyramidal carbon loaded polyurethane absorber manufactured by Emerson & Cuming Microwave, Co. in Belgium. The absorber is intended for millimetre wave frequencies, and the pyramids are 38 mm high with a spacing of 19 mm. The material is available in standard sheet sizes of 60 x 60 cm², with or without a protective blue paint. The protective paint is known to increase the reflectivity at higher frequencies, so the samples were ordered without it. The penalties are increased fragility and production of carbon dust. The size of the pyramids is too high for any meaningful results with the short-range measurement system described in the next section, so the flat side of the absorber was used in the measurements. The flat surface of the tested material is shown in the right side of Figure 4.2. The thickness of the test sample without the pyramids is 20 mm.

Two wool carpet materials (labeled #1 and #2 in Figure 4.3) from Bauhaus Home Store were also selected for the tests. The front surfaces of both carpets have woven knots with a separation of about 2 mm. The knots are bound to an intermediate layer which in turn is glued to a wool base layer. The sizes of the test samples are 10 x 15 cm², with thicknesses of 5 mm.

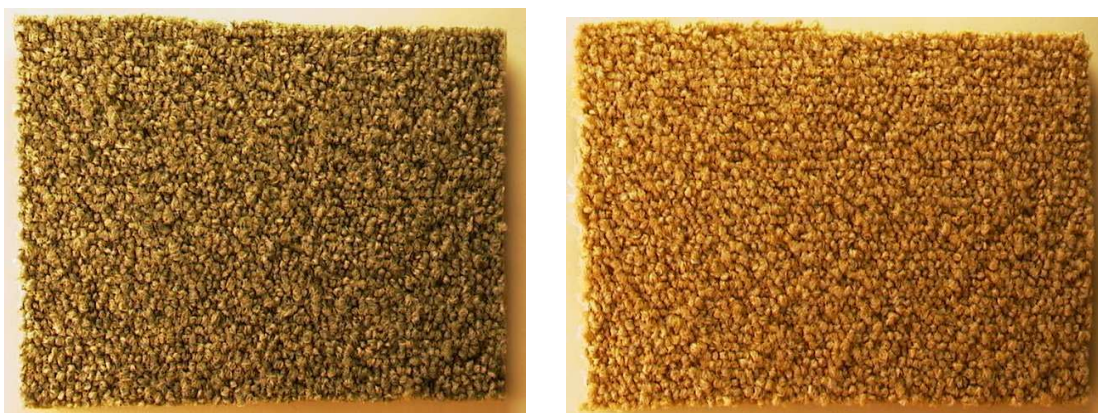


Figure 4.3 Bauhaus wool carpet #1 (green, left) and Bauhaus wool carpet #2 (brown, right).

A floor mat from Bauhaus Home Store was also included in the reflectivity measurements. The material consists of three layers: knots woven from plastic strings, glue, and synthetic rubber backing. The 10 mm long knots are arranged on the surface with 5 mm separation to each other, as can be seen from Figure 4.4 (left side). Thickness of the composite is 9 mm (6 mm knots and 3 mm glue+rubber). Size of the test sample is 10 x 15 cm².

The last material in the tests was a green-coloured synthetic floor carpet ‘synthetic grass’ from Etola (Figure 4.4, right side). The front surface is made of woven plastic strings, which are held together by glue. The back side has rubber bumps separated 13 mm from each other. Thickness of the material without the bumps is 8 mm. The bump height is 2 mm.



Figure 4.4 Bauhaus floor mat (left) and Etola synthetic carpet (right).

Transmission losses through all the materials were measured at 200–600 GHz in order to be able to better understand their scattering behaviour and especially the contribution of the reflection from the metal backing (sample holder). The material samples were placed between the transmitter and receiver facing each other at a distance of 14 cm (like in Figure 5.6 but without sample holder and $\theta_i = 90^\circ$). The transmission losses compared to free space propagation are shown in Table 4.1. Some of the tabulated values have a range, which means that the material is non-homogeneous.

Table 4.1 The measured transmission losses through the materials as a function of frequency.

Loss [dB]	200 GHz	300 GHz	400 GHz	500 GHz	600 GHz
FIRAM-500	15	20-25	40	40-50	>45
TERASORB-500	25	30-35	60	>60	>45
TK THz RAM	30	45	45	60	>45
ECCOSORB	70	>72	>70	>60	>45
Bauhaus wool #1	10-15	15	22	15-20	20-30
Bauhaus wool #2	10-15	15	22	15-20	20-30
Floor mat	10-25	20	25-40	25-40	30-35
Etola synthetic	2-15	3-20	10-15	8-30	10-20

4.2 Construction of the test bench

The need for an adequate dynamic range at 600 GHz, the small size of the test samples, and the beamwidths of the antennas set the maximum distance between the antennas and the sample center. A distance of 7 cm (path length of 14 cm between the transmitter and received horns) was selected, as it provided a comfortable dynamic range of 45 dB even at 600 GHz. An illustration of the sample illumination with the 300 and 600 GHz corrugated horns (-3 dB beamwidths of 20°) is shown in Figure 4.5. The dynamic ranges at other frequencies are evident from Table 4.1, being over 70 dB across 200–400 GHz and about 60 dB at 500 GHz.

The test instrumentation is based on the AB Millimetre MVNA-8-350 vector network analyzer with submillimetre wave extensions ESA-1 and ESA-2. The operating principle and the dynamic range of the analyser are discussed e.g. in [21]. The ESA-1 extension uses a phase-locked Gunn oscillator followed by a frequency multiplier to provide a stable signal with power levels decreasing from 1 mW at 200 GHz to a couple of microwatts at 600 GHz. The multiharmonic receiver extension ESA-2 uses a similar phase-locked Gunn oscillator as the LO source for a whisker-contacted Schottky harmonic mixer. The conversion loss of the receiver increases from about 25 dB at 300 GHz to 35 dB at 600 GHz. A simpler Schottky diode mixer (ABmm HM-D) pumped with a microwave signal was used at the 200 GHz measurements as the receiver (conversion loss is about 45 dB).

The used horn antennas included two 6×4.5 mm² pyramidal horns with WR-5 flange (used at 200 GHz), a 300 GHz corrugated horn antenna with WR-3 flange (transmit horn at 300 & 400 GHz), a 10.5×8 mm² pyramidal horn antenna with WR-4 flange (receive horn at 300 & 400 GHz), and two 600 GHz corrugated horn antennas (used at 500 & 600 GHz). The direct coupling between the horns causes problems at high incident angles. The measured directly coupled signal levels are indicated in the reflectivity figures, and their effects are discussed in Chapter 4.3.2.

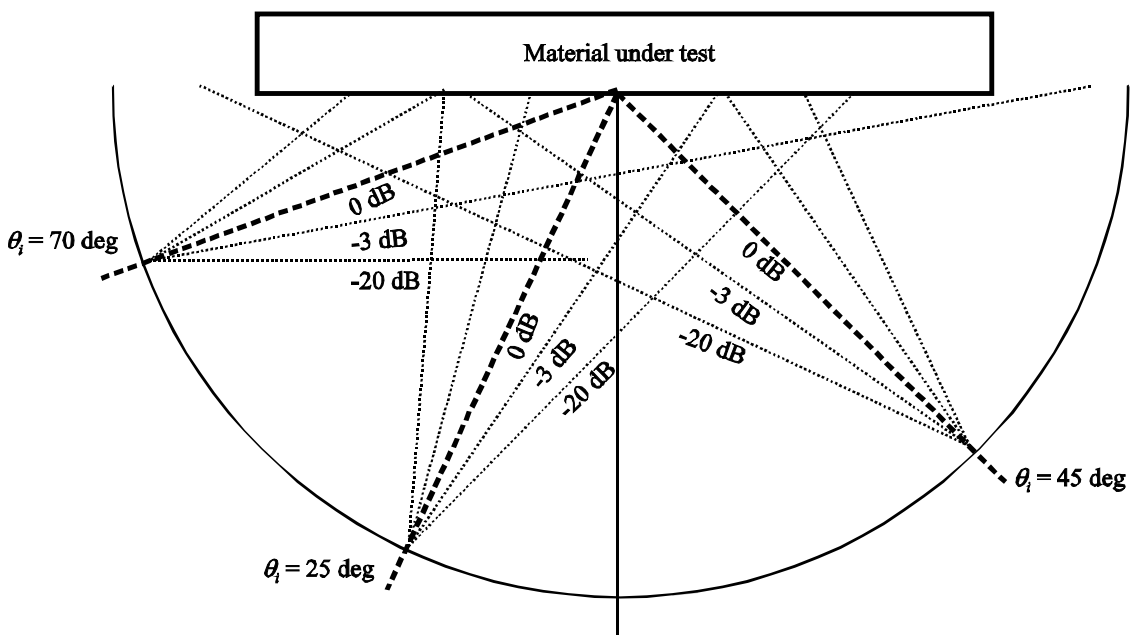


Figure 4.5 Illustration of the sample illumination from the corrugated horns.

The bistatic test bench for the specular scattering measurements was constructed on a large optical table. The transmitter and receiver are mounted on special arms which are made out of lapped wooden laminate and bolted together on one end. The sample holder is mounted on the geometrical center point of the arm assembly (some adjustment is necessary to compensate different sample thicknesses). An automated incident angle sweep, controlled by the vector analyzer, is facilitated with a linear scanner, which pulls the sample holder and arm assembly along a pair of guide pins. Tensioning springs are used to keep the metal rails on the side of the arms in contact with the guide pins. A schematic view of the test bench is shown in Figure 4.6 and a photograph in Figure 4.7. Repeatability of the angle sweep and return to origin angle was measured to be about 0.5° . The small uncertainty is caused by the clearances in the scanner screw drive and ball bearings, but it does not add up since origin angle calibration is performed each time the sample material is changed.

The relation between the linear movement t and the resulting incident angle θ_i is a nonlinear function. The angle calibration was done by using a digital angle meter (Bosch DWM 40L) with a certified reading accuracy of $\pm 0.1^\circ$. The linear movement range was divided into 20 points, where angle readings were recorded. The angle scale for the RF measurements was calculated with a computer by using curve fitting.

The calibration curve resembles an exponential function, so it was natural to use exponential regression. The exponential regression method (for example, the LOGEST –function in an Excel spreadsheet) fits an exponential curve in the form of $y(x) = bm^x$ to the calibration points. The fitted curve is $y(x) = 68.27725 * 0.994812^x$, and it shows an excellent fit to the calibration points. The missing angle points between the calibration points are then easily calculated.

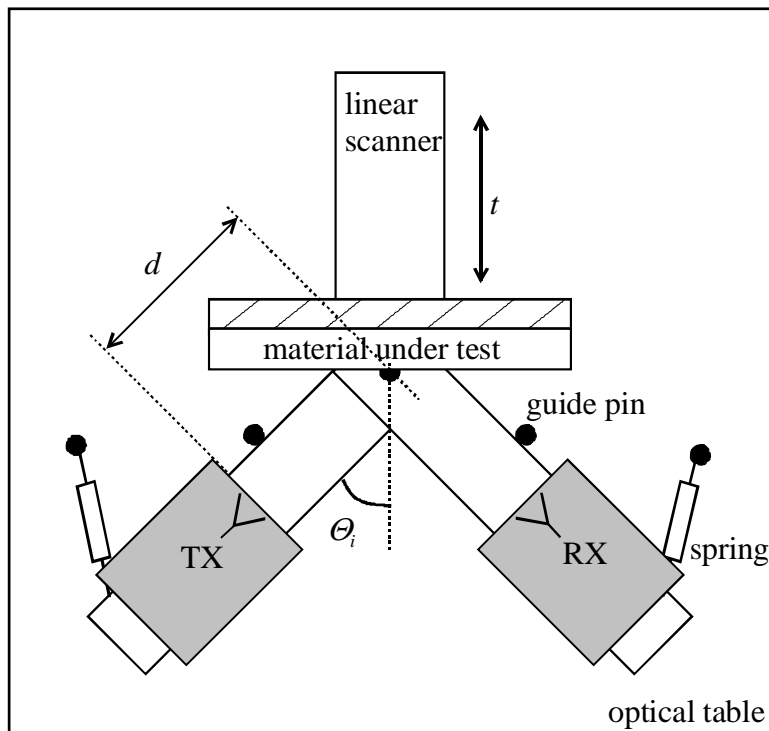


Figure 4.6 Schematic view of the test bench.

The samples are attached to the sample holder with two velcro strips according to the alignment marks. Good repeatability is ensured by pressing the sample hard and verifying the surface flatness by an angle gauge. Another possibility would have been to use a vacuum sample holder, but this was not available for the measurements. Also, the use of vacuum would have required some additional backing material to be glued to some of the materials in order to provide a compatible surface.

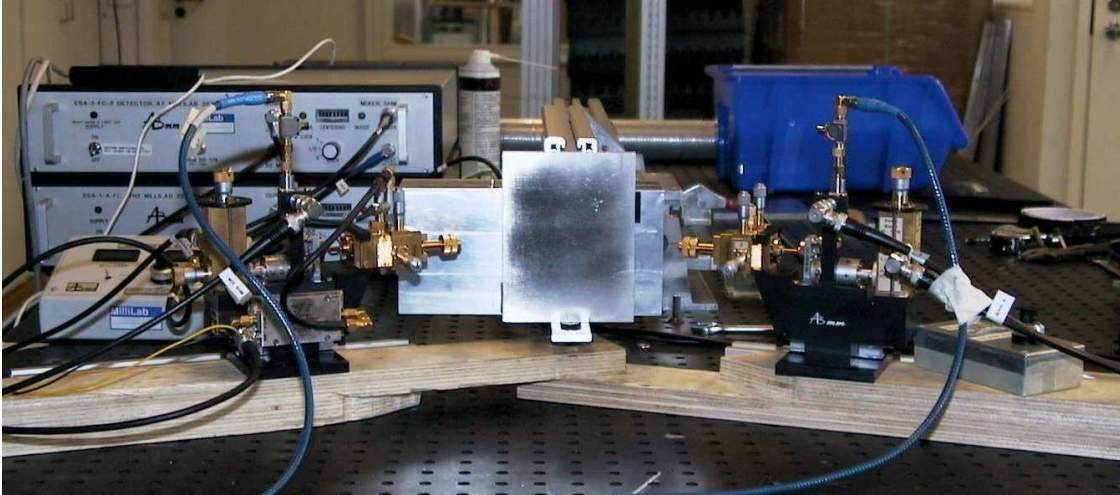


Figure 4.7 Photograph of the test bench with surrounding absorbers removed (calibration target at 600 GHz, vertical polarisation).

4.3 Measurement results

4.3.1 Measured reflectivities for the materials

The reflectivities were measured at both vertical and horizontal polarisations for all the materials. At each frequency and polarisation, the reflection from a polished flat aluminium plate (calibration target) was measured first. The measured reflection maximum from this target set the 0 dB level in the measurements and in the following figures. The calibrated reflectivities at 200–600 GHz are shown in Figures 4.8–4.17. The wedged-type absorbers FIRAM-500 and TERASORB-500 were tested with the grooves in both vertical (gv) and horizontal (gh) directions. The bistatic angular range was limited by the transmitter and receiver geometries to 25° – 69° . Monostatic measurements at normal incidence were also attempted with an existing WR-3 waveguide directional coupler (20 dB coupling) at 300 GHz, but the leaking signal was too strong and masked out most of the scattered power from the target.

At 200 GHz and at vertical polarisation, the lowest overall reflectivity (below -40 dB across 25° – 52°) is observed from TK THz RAM. The wedged-type materials provide over 10 dB lower reflectivity with the groove direction perpendicular to the polarisation, when compared to the situation where grooves are in the same direction. The Eccosorb material shows quite good reflectivities of -30 ... -40 dB at angles below 50° . The reflectivities of the floor carpets depend not so much on the incident angle (as expected from a nearly random surface), and vary between -10 ... -30 dB. The results

for the horizontally polarised case are corrupted by the directly coupled power between the horn antennas, and not much can be concluded from the figures.

The directly coupled power is much less a problem at 300 GHz, although at horizontal polarisation it is 10–15 dB higher than at vertical. This is caused by the pyramidal horn used at the receiver, as it has a wider beam at horizontal polarisation. Again, the TK THz RAM shows the lowest overall reflectivity at both vertical and horizontal polarizations. The observed scattering maxima at 53° and 64° at vertical polarisation are caused by multiple reflections from the pyramid sides. At horizontal polarisation, a maxima is observed at 44° . The regular sharp tips of the absorber form, in fact, a 2-dimensional diffraction grating, thus grating lobes are expected at all frequencies [7,8]. Furthermore, the non-symmetry of the polarised responses is evident. Visual inspection of the material shows that the individual molded absorber pieces (the test sample consists of 16 pieces) are not exactly symmetrical and the absorber tips are not level with each other. Some of the pieces are curved, some others are not, due to material molding tolerances. The measured reflectivities for TK THz RAM compare very well with [8], where reflectivities of $-60\dots-20$ dB were measured between 50° – 75° at 337 GHz. FIRAM-500 and TERASORB-500 behave smoothly at vertical polarisation, with reflectivities below -25 dB up to 55° with horizontal groove direction. At horizontal polarisation, the vertical groove direction gives lower reflectivity up to about 45° , after which horizontally directed grooves work better.

At 400 GHz and with both polarisations, the TK THz RAM again shows best performance. The same scattering maxima as at 300 GHz are observed, although slightly shifted. Its reflectivity is below -37 dB up to 60° . The performance of the FIRAM and TERASORB materials is very similar to the 300 GHz curves, being below -25 dB in a wide angular range if the grooves are aligned perpendicular to the polarisation. Direct coupling at horizontal polarisation is 10–20 dB higher than at vertical polarisation, and it limits the measurement accuracy between 55° – 70° , which is seen as increased fast ripple or noise in the measured scattered power.

At 500 GHz, direct coupling between the horns at both polarisations limits the useful maximum incident angle to about 60° . TK THz RAM has the best specular performance with below -30 dB reflectivity over a wide angular range. Regular grating lobes are observed in the scattering patterns. Specular reflectivity for this material with normal incidence has been measured in [7] to be -58 dB. Diffraction grating lobes are observed also for FIRAM and TERASORB with vertical groove directions. Similar effects were noticed in [7] for the FIRAM material, where its monostatic specular reflectivity at normal incidence was measured to be about -45 dB (grooves vertical) and -41 dB (grooves horizontal) with both polarisations. It is evident from the measurement results that the wedged-type materials work better at 500 and 600 GHz than at lower frequencies, and they approach in performance the TK THz RAM at both polarisations. However, the TK THz RAM has some problems with non-specular scattering which will be discussed in Chapter 5. Eccosorb also has good reflectivity values below -20 dB over a wide angular range.

The limited dynamic range of about 45 dB at 600 GHz causes the increase in measurement uncertainty at reflectivities below -30 dB. The same grating peaks for FIRAM and TERASORB are observed in the vertical groove direction measurements.

The TK THz RAM and FIRAM-500 have reflectivities below -30 dB in a wide angular range at vertical polarisation. At horizontal polarisation, the reflectivity of TK THz RAM stays below -30 dB up to 60° , whereas the FIRAM and TERASORB have about 5 – 10 dB higher reflectivity. Comparing the results for TK THz RAM to [8], where reflectivities of -65 ... -25 dB between 40° – 75° were measured at 604 GHz, reveals that a higher dynamic range would have been useful. Monostatic specular scattering results for FIRAM-500 measured at 584 GHz are presented in [6]. Similar strong grating lobes reaching -20 dB level are observed with grooves vertical, and reflectivities reaching -60 dB with grooves horizontal. The used polarisation was not specified. The floor carpet materials (except the Etola synthetic) have also quite good reflectivities, below -15 dB, over the whole tested angular range.

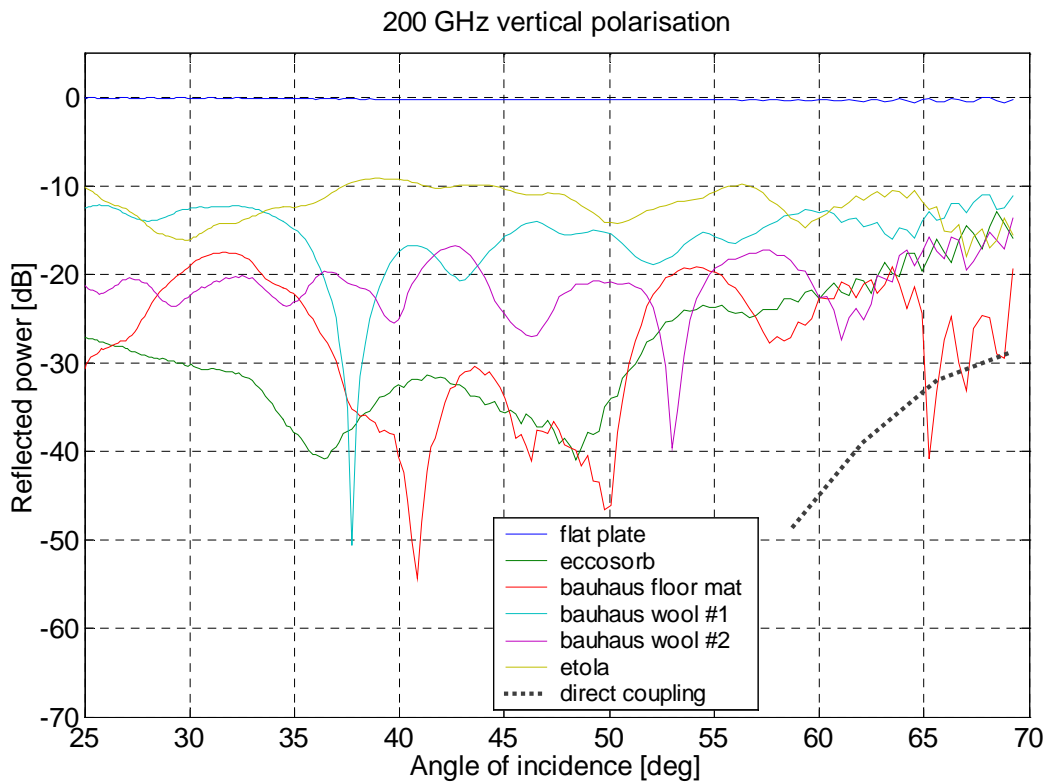
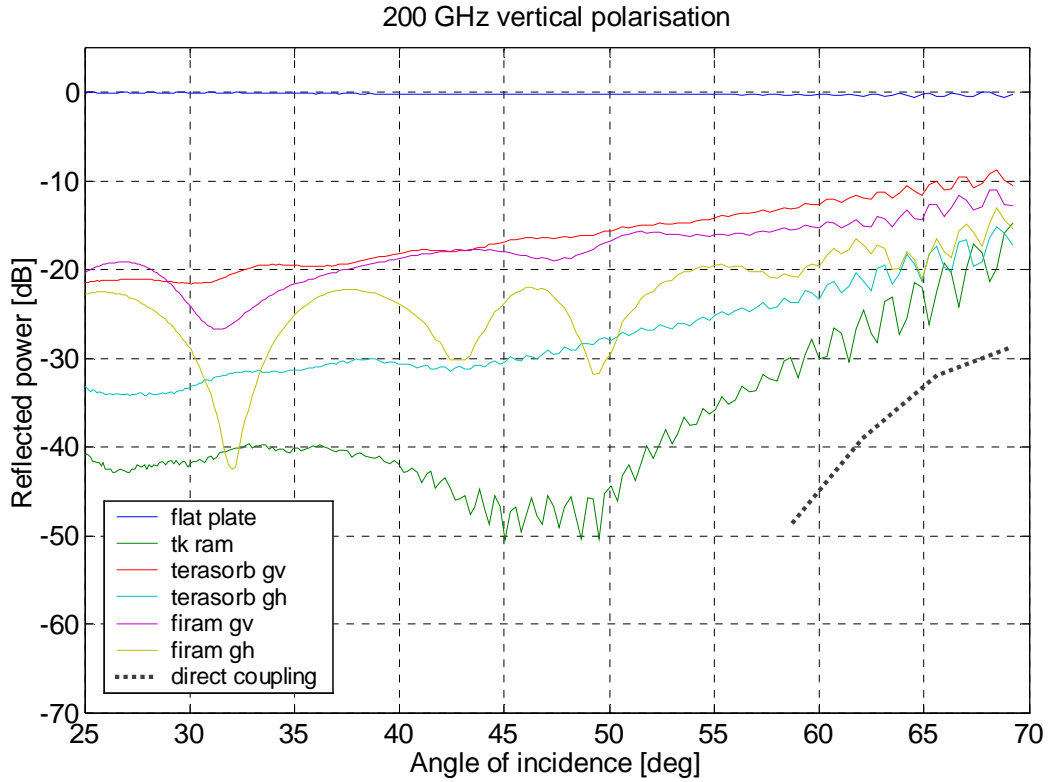


Figure 4.8 Reflectivity as a function of the specular angle at 200 GHz and vertical polarisation.

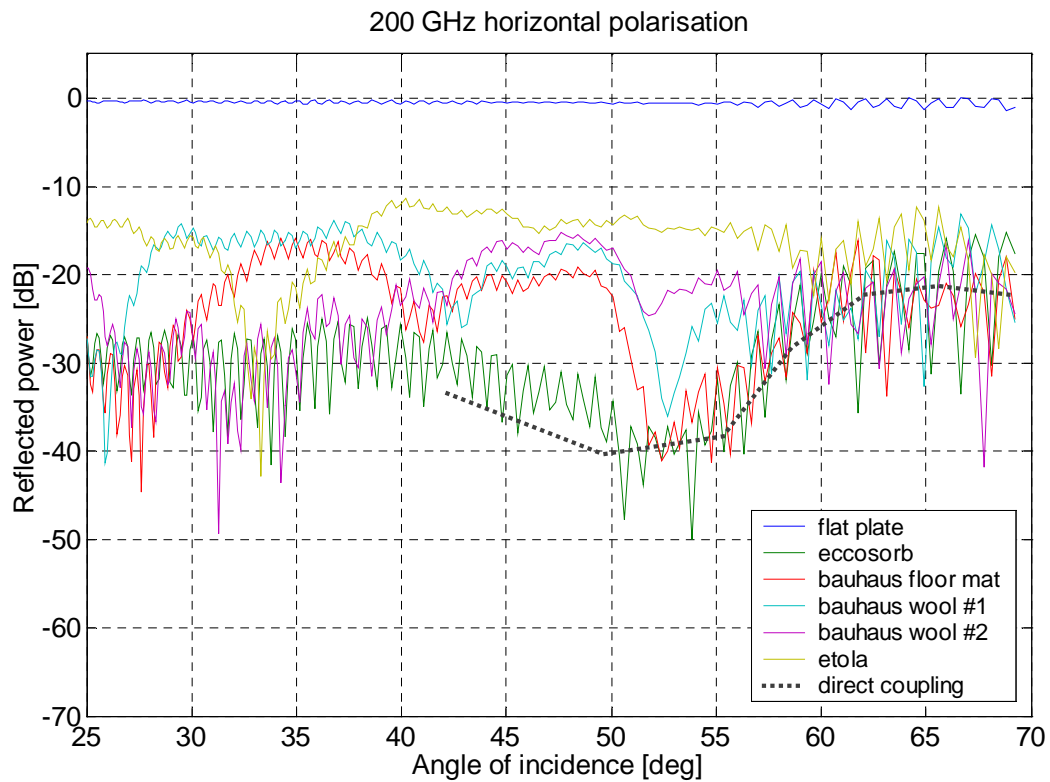
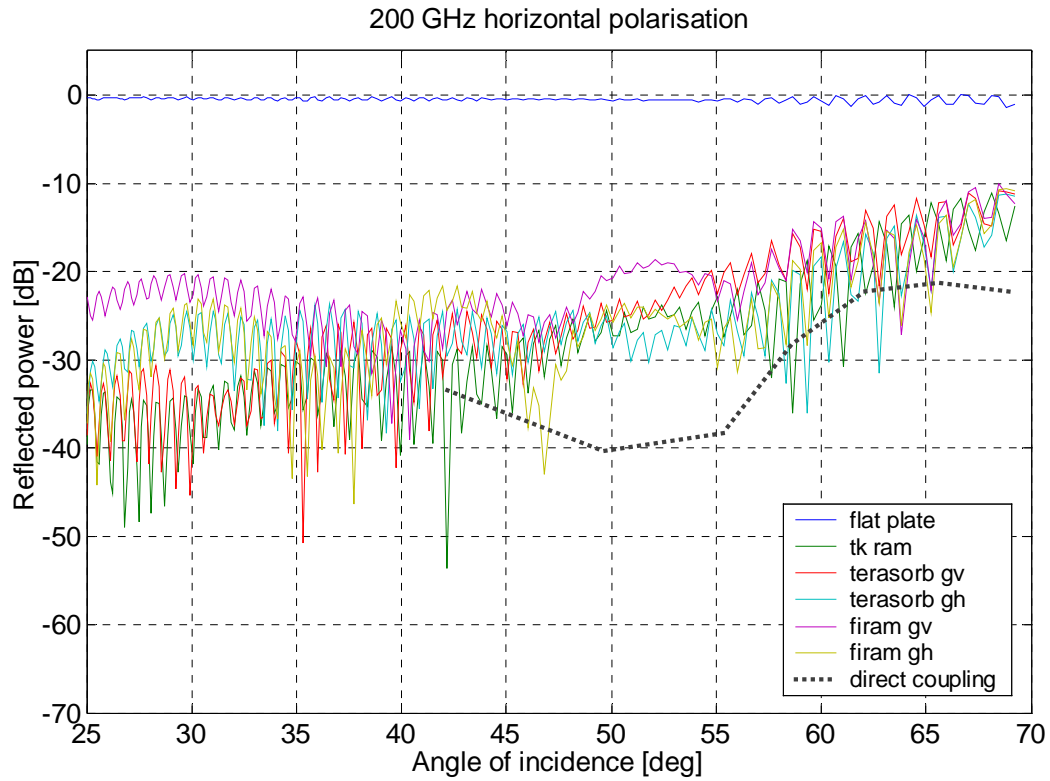


Figure 4.9 Reflectivity as a function of the specular angle at 200 GHz and horizontal polarisation.

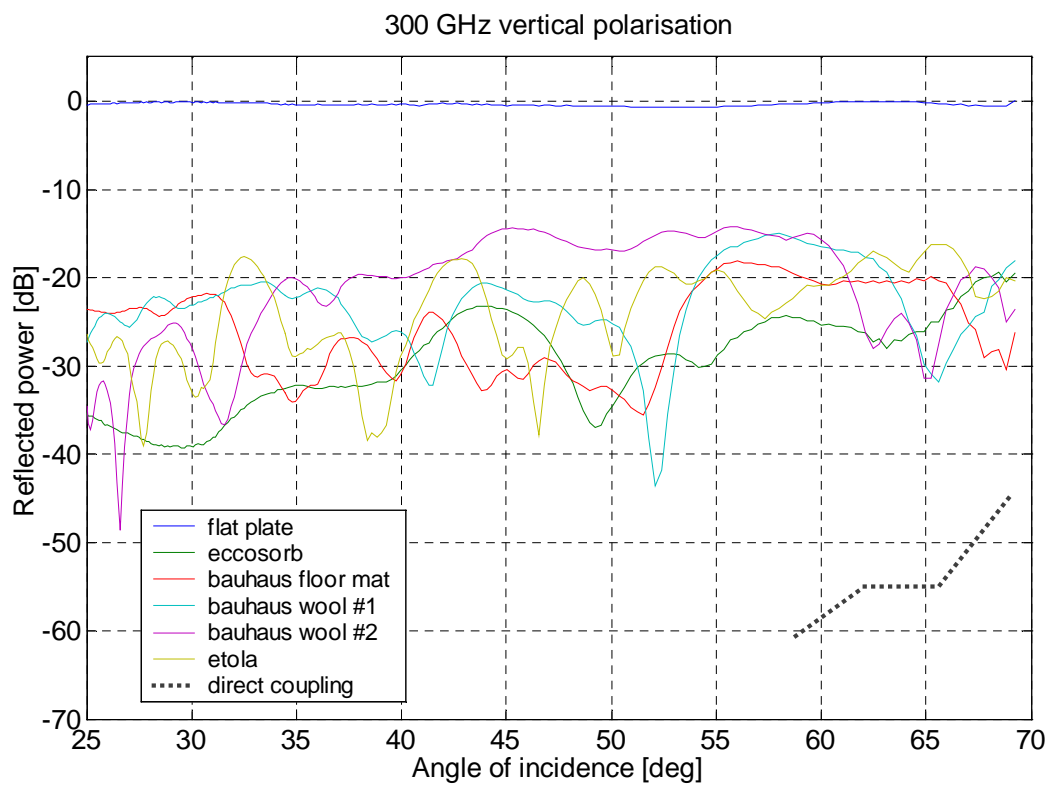
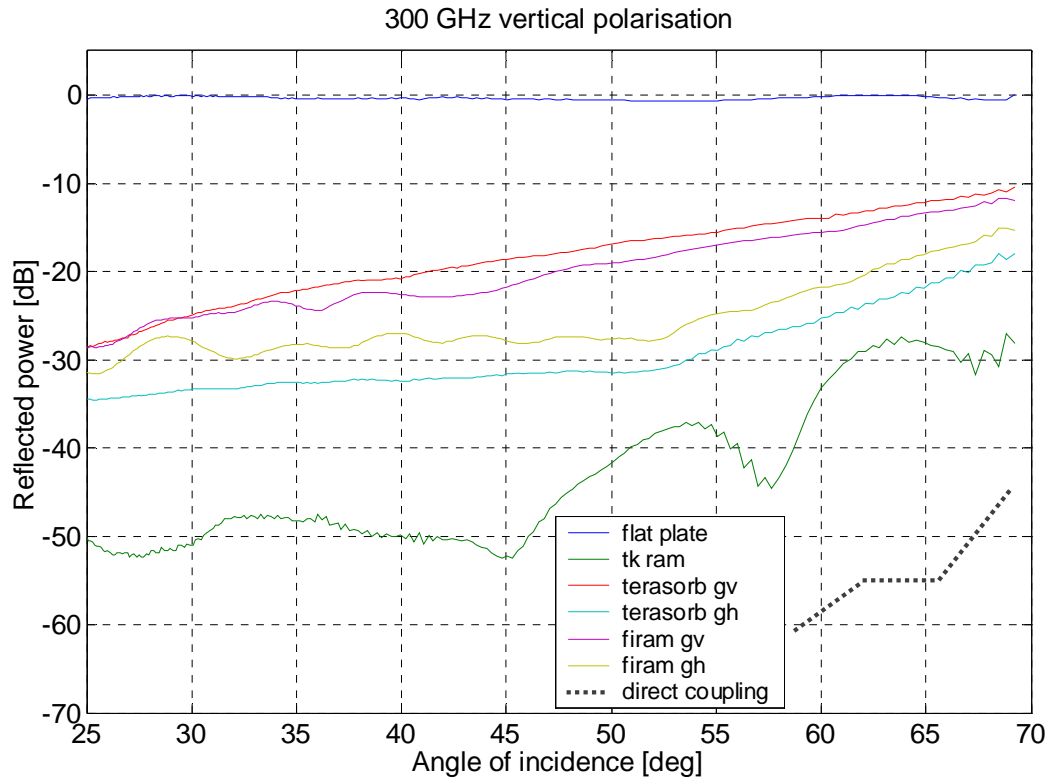


Figure 4.10 Reflectivity as a function of the specular angle at 300 GHz and vertical polarisation.

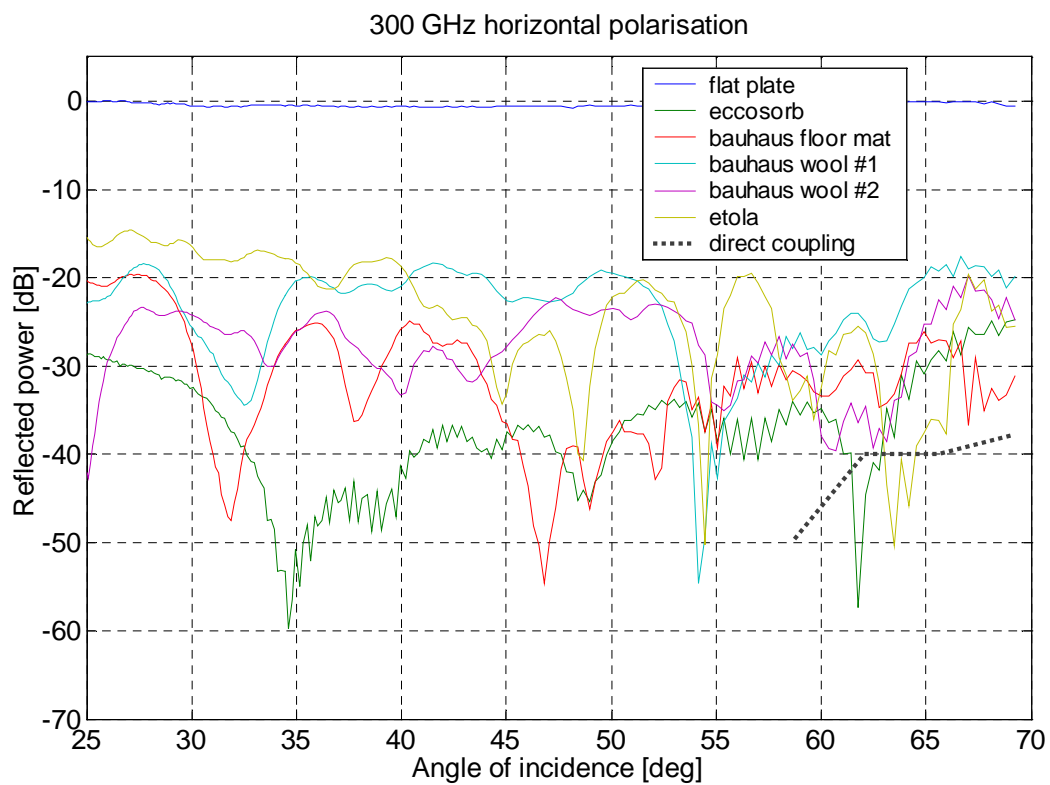
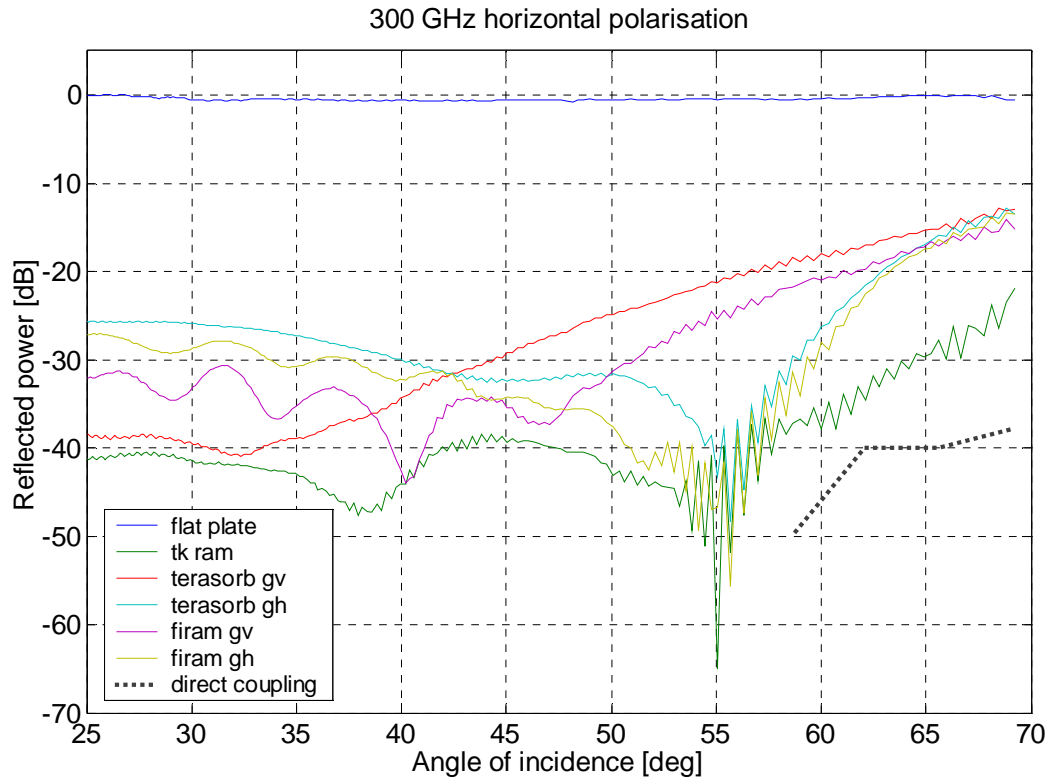


Figure 4.11 Reflectivity as a function of the specular angle at 300 GHz and horizontal polarisation.

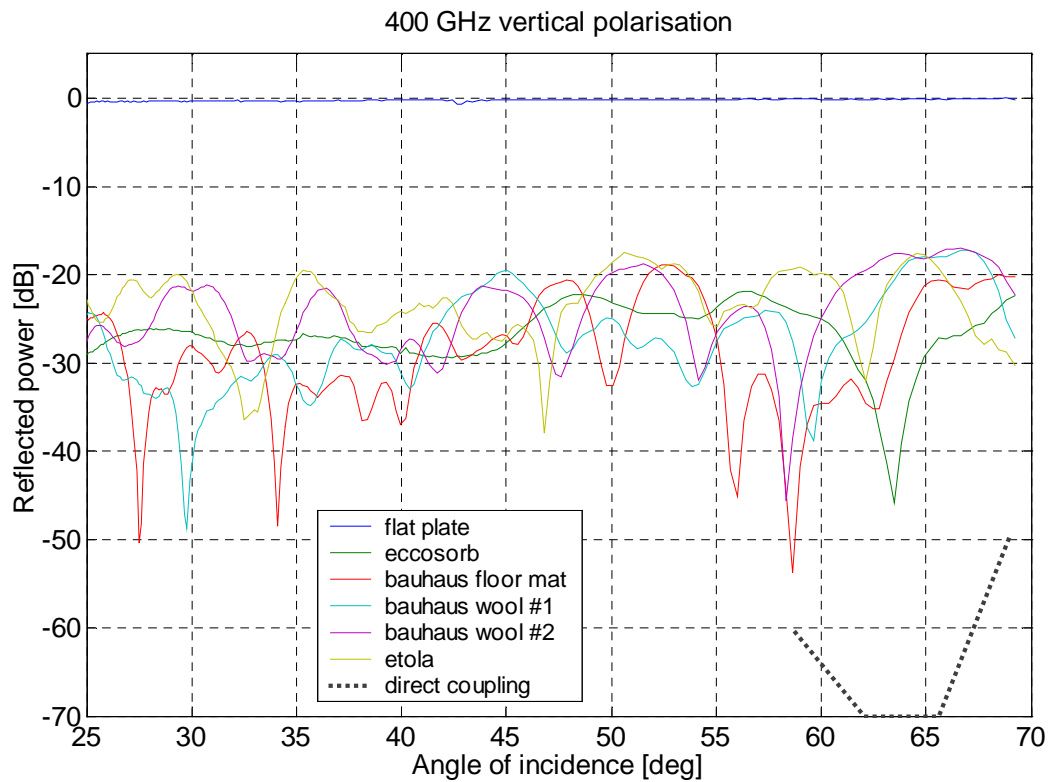
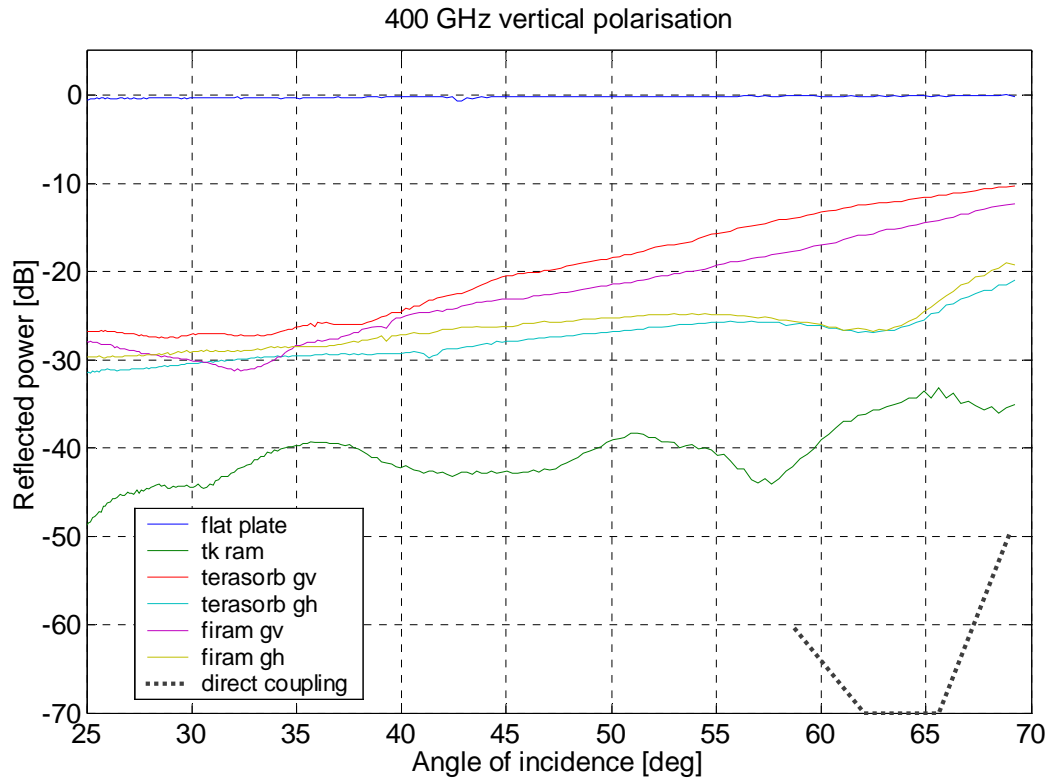


Figure 4.12 Reflectivity as a function of the specular angle at 400 GHz and vertical polarisation.

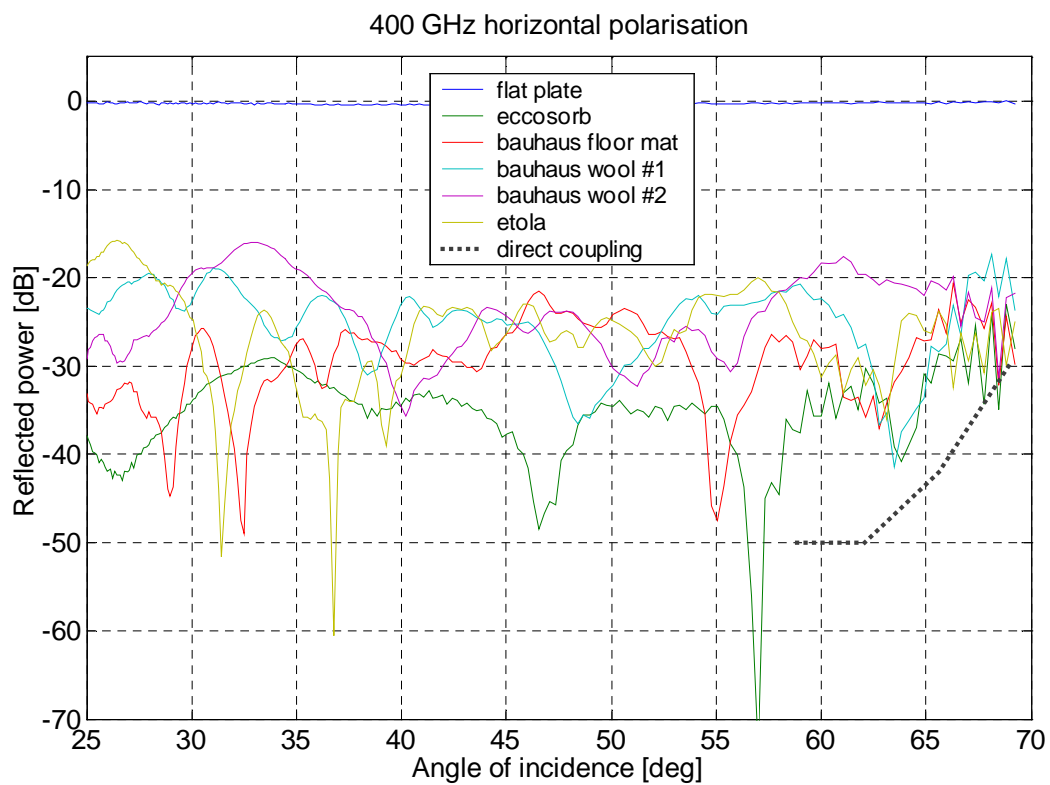
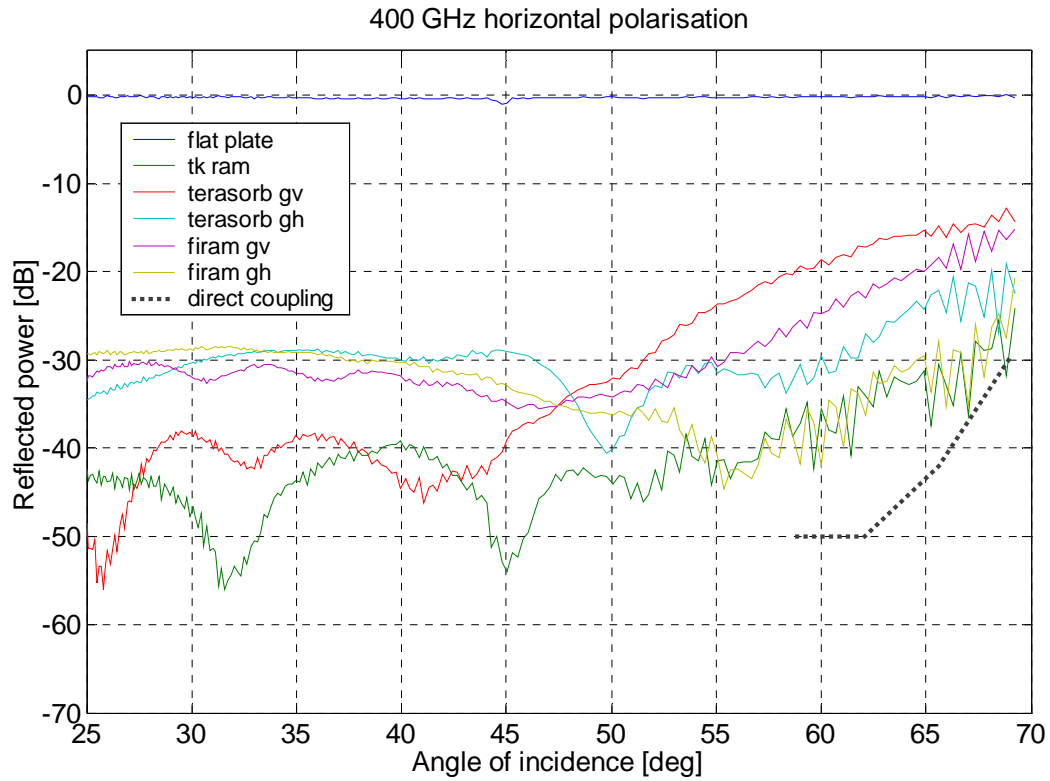


Figure 4.13 Reflectivity as a function of the specular angle at 400 GHz and horizontal polarisation.

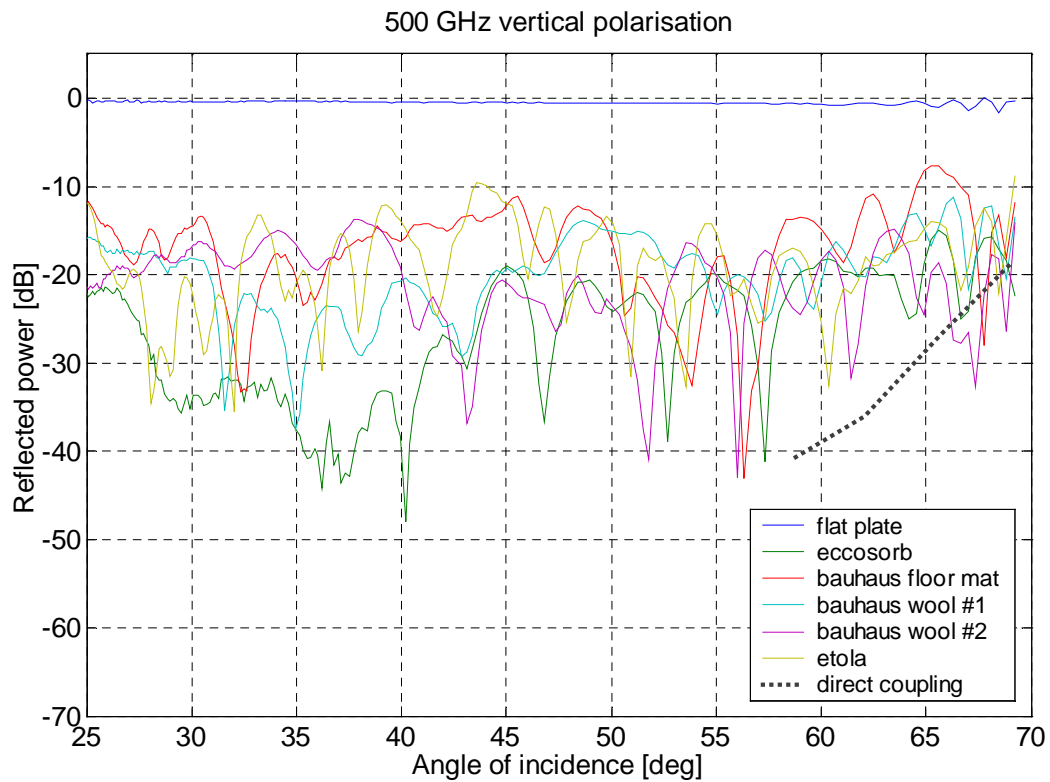
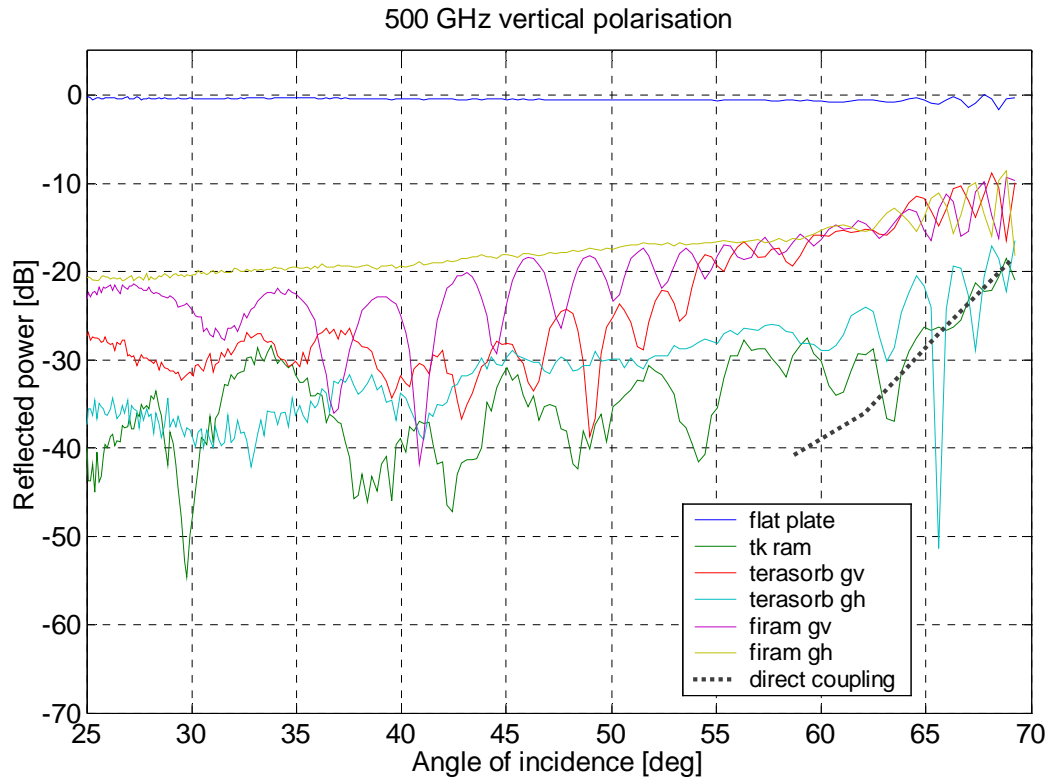


Figure 4.14 Reflectivity as a function of the specular angle at 500 GHz and vertical polarisation.

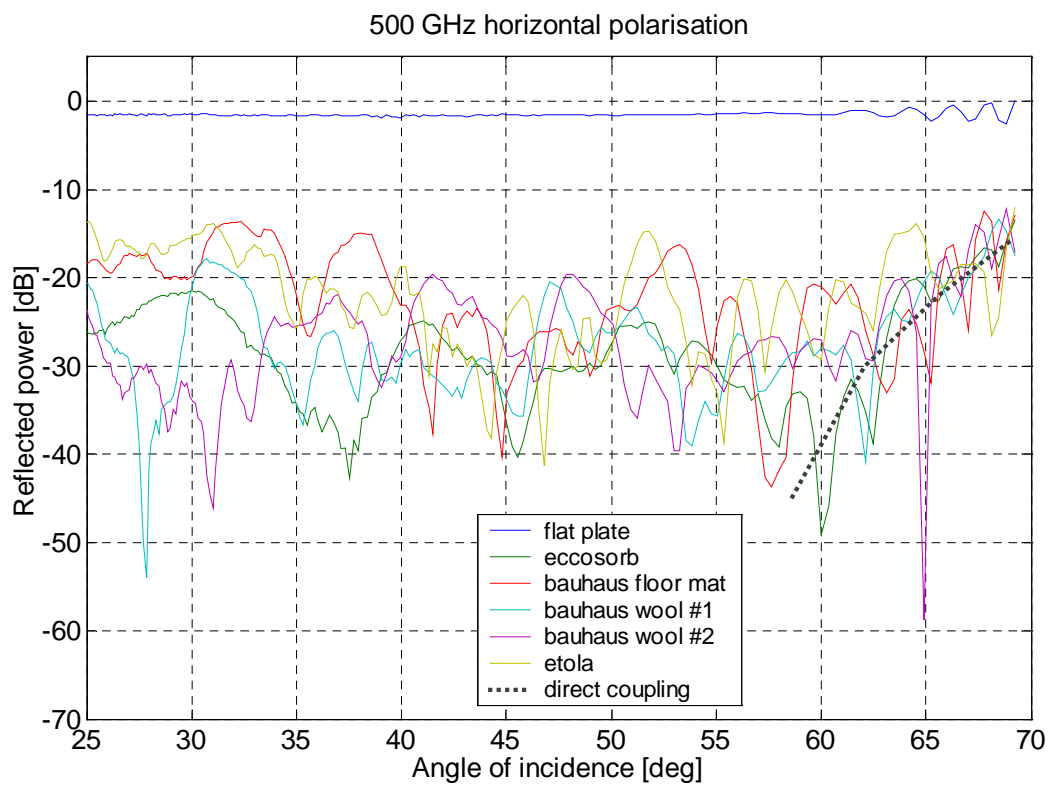
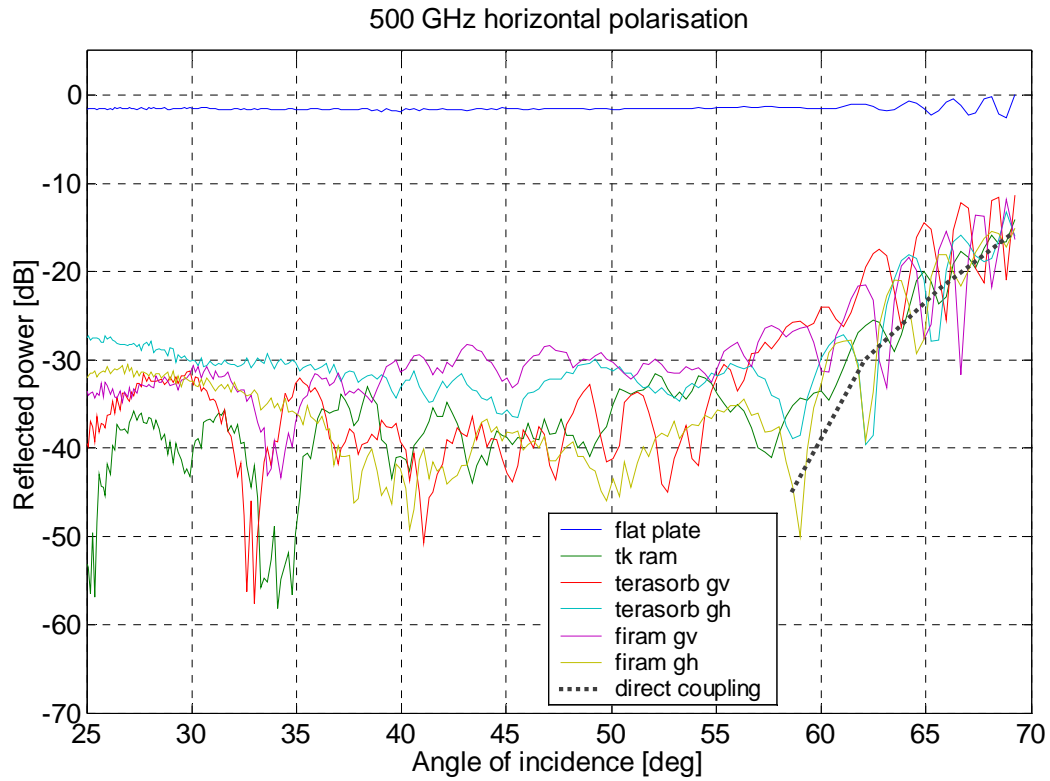


Figure 4.15 Reflectivity as a function of the specular angle at 500 GHz and horizontal polarisation.

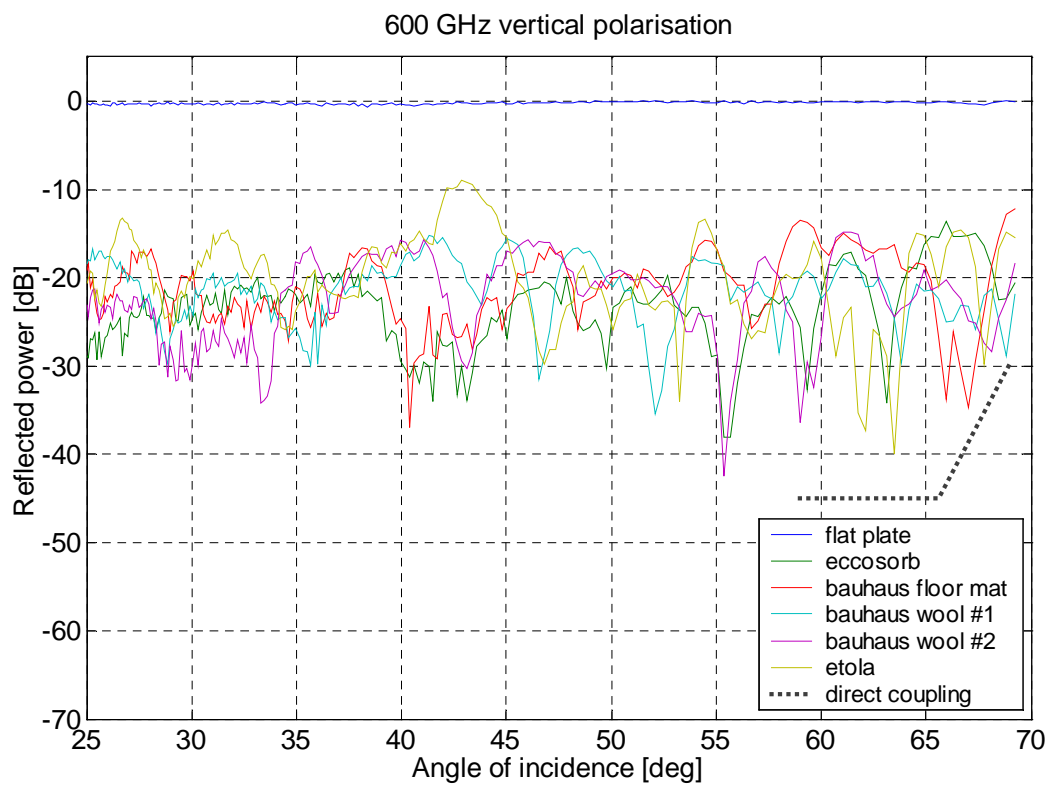
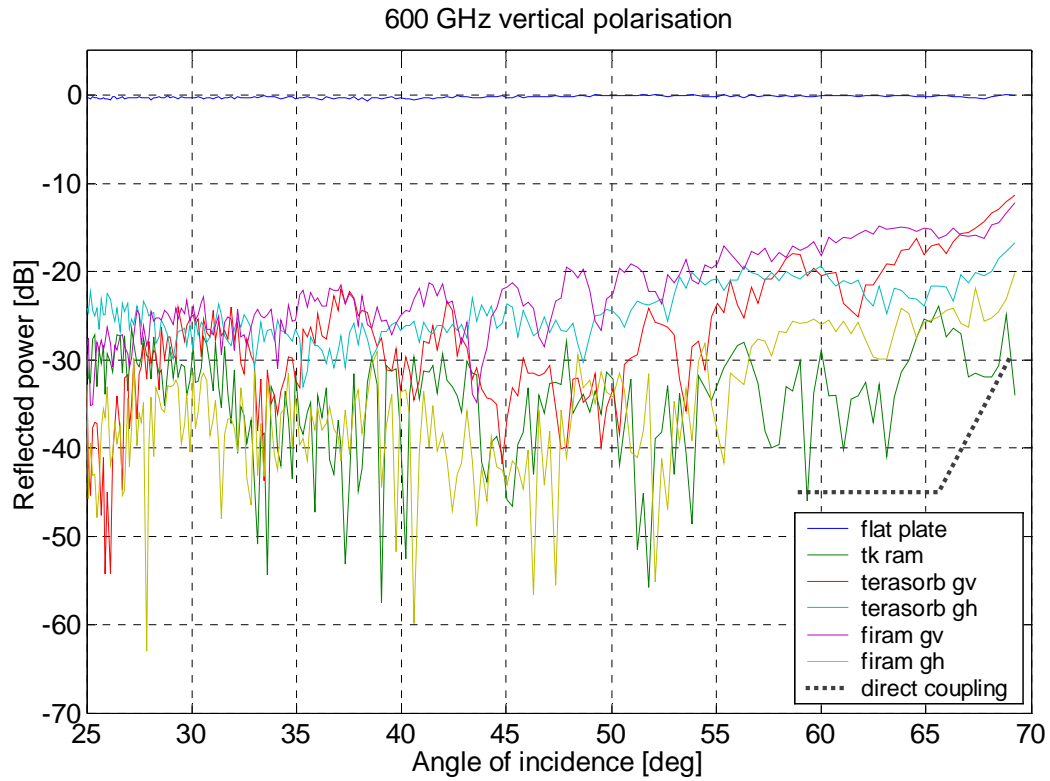


Figure 4.16 Reflectivity as a function of the specular angle at 600 GHz and vertical polarisation.

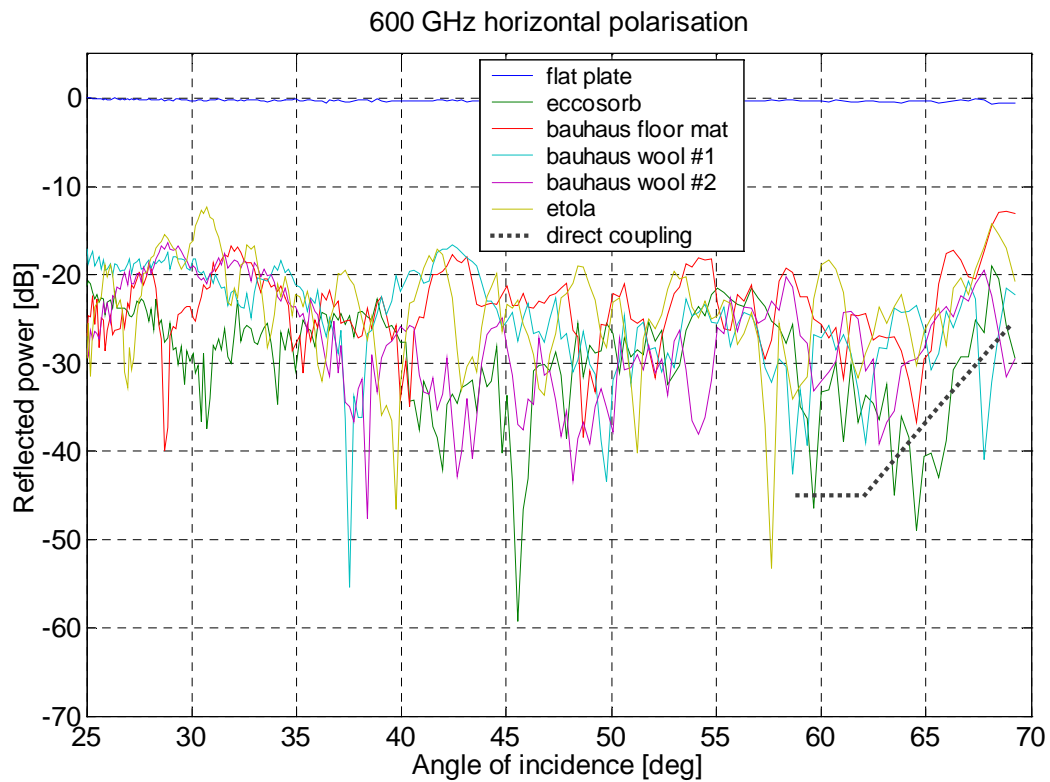
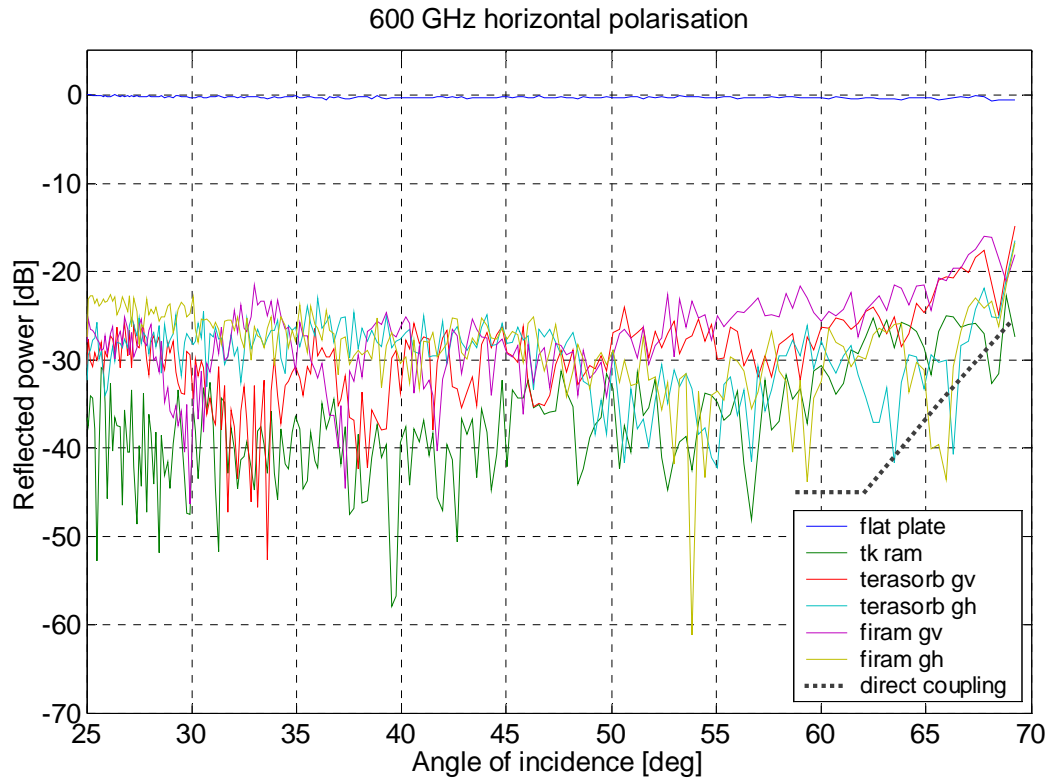


Figure 4.17 Reflectivity as a function of the specular angle at 600 GHz and horizontal polarisation.

4.3.2 Effect of non-idealities

4.3.2.1 Direct coupling between the horn antennas

Direct coupling is a serious problem with horizontal polarisation at 200 GHz. The small aperture ($6 \times 4.5 \text{ mm}^2$) pyramidal horns have strong sidelobes at horizontal polarisation. Figure 4.18 shows the calculated theoretical E-plane (vertical) and H-plane (horizontal) directional patterns for this horn. The pattern was calculated with the horn and reflector antenna analysis package Sabor [22]. The observed sidelobes in the H-plane pattern at 24.1° and 51.5° correspond to the directly coupled power maxima at 66° (-20 dB) and 38.5° (-30 dB) in Figure 4.8.

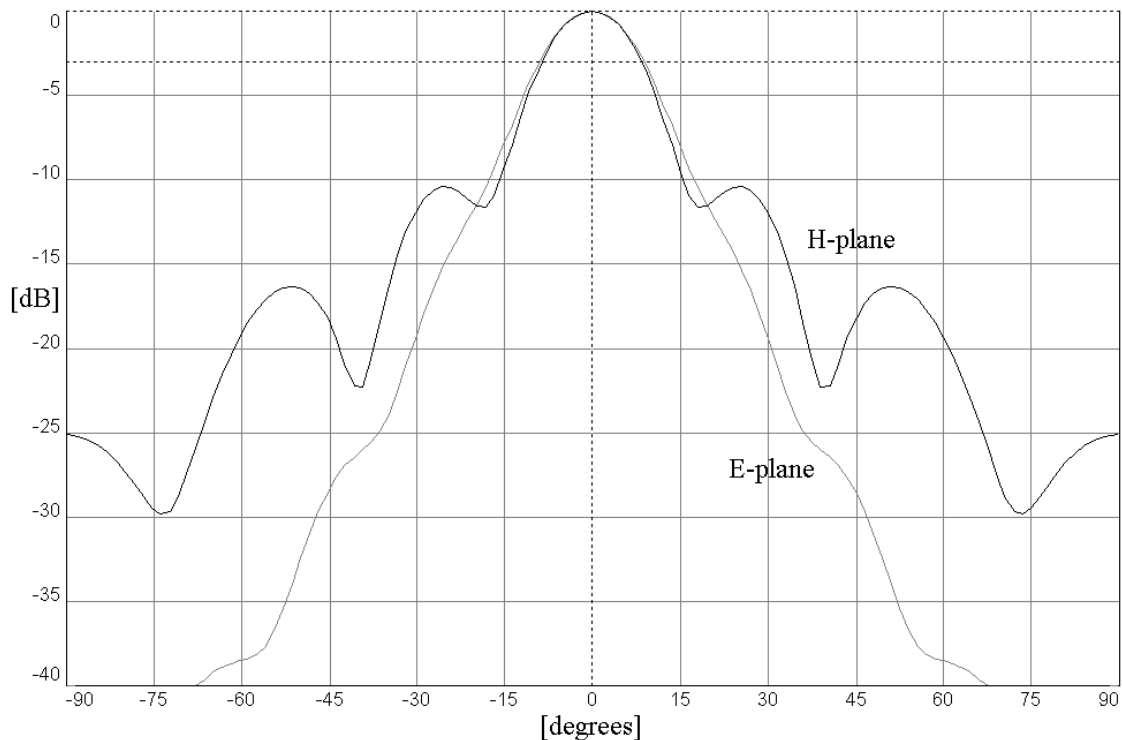


Figure 4.18 Theoretical E- and H-plane directional patterns of the 200 GHz horns.

4.3.2.2 Dynamic range limitations at 500 and 600 GHz

The dynamic range of the test bench at 500 GHz is limited to about 60 dB, and at 600 GHz to 45 dB. The decreased range is caused by rapid degradation of the output power from the transmitters multiharmonic multiplier with increasing harmonic number. Increased noise is observed at the 600 GHz measurements. The real reflectivity from, say, TK THz RAM, probably follows the upper envelope of the noisy curve.

4.3.2.3 Pointing errors

Although great care was used when positioning the sample materials to the sample holder, small deviations between adjacent measurements are observed. Repeatability of the reflectivity measurements was studied by executing three 'cycles' consisting of mounting a sample, measuring its reflectivity, and taking it out. The repeatability was measured to be within ± 2 dB, which consists of the effects of sample positioning errors and vector analyzer measurement uncertainty. The initial angle of the angle sweep was calibrated between each measurement. In addition to amplitude errors, the sample positioning inaccuracy causes angular shifting of scattering features (minima and maxima) up to a few degrees.

5 NON-SPECULAR REFLECTIVITY MEASUREMENTS AT 300–400 GHz

5.1 Construction of the test bench

The scattering from the absorber materials into non-specular angles was also studied. In this experiment, the incident angle θ_i was kept constant and the receiving angle θ_o was swept: starting from a minimum angle set by geometry up to 90° . Suitable incident angles were chosen to be 26.5° , 45° , and 63.4° . The tests were carried out at 300 and at 400 GHz because of the available dynamic range of over 70 dB. The transmitting antenna was a corrugated horn with WR-3 flange. The 26.5° incident angle tests were done with the WR-4 pyramidal horn antenna as the receiving antenna. A second, identical corrugated horn was received for the 45° and 63.4° tests. The sidelobes of the corrugated horns are at a much lower level than those of the pyramidal horn at horizontal polarisation. Unfortunately, the tight schedule for making the measurements prevented repeating the 26.5° incident angle measurements with the new horn.

The test bench was modified from the specular setup in order to facilitate a computer controlled receiving angle sweep, and is shown in Figures 5.1 and 5.2. The linear scanner is connected to the receiver arm through two joints and a connecting rod. The maximum receiving angle range with this system is -10° ... $+100^\circ$. Repeatability of the angle sweep is the same as for the specular setup, i.e., 0.5° . The TX & RX assemblies limit the maximum receiving angle range for each incident angle. With incident angles of 26.5° , 45° , and 63.4° , the maximum receiving angle ranges are 22° – 90° , 5° – 90° , and 0° – 90° , respectively.

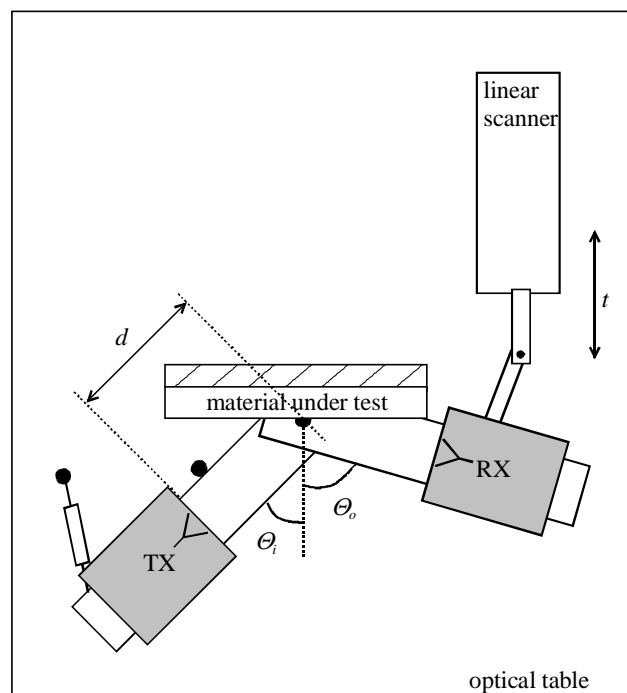


Figure 5.1 Schematic layout of the non-specular reflectivity measurement system.

The linear travel distance t and the receiving angle θ_o are nonlinearly related. As with the specular setup, the angle calibration was done with a digital angle gauge. The linear travel range was divided into 20 points, where angle readings were recorded. The calibration curve resembles a linear function, so it was decided to use linear curve fitting. First, fitting a line to all the points was tried, but the deviation of the calibration points from the fitted line was unacceptable. Linear interpolation between adjacent calibration points provided much more accurate results. The Excel spreadsheet's TREND –function fits a line between two adjacent calibration points and calculates the required angle points between them. The procedure is repeated until all the angle points are known.

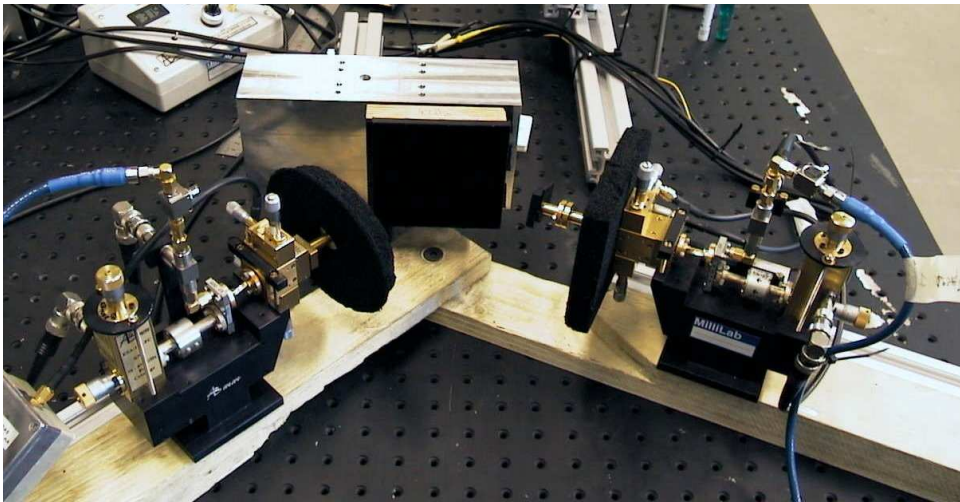


Figure 5.2 Photograph of the non-specular reflectivity measurement system (300 GHz, TK THz RAM, $\theta_i = 45^\circ$ and horizontal polarisation).

5.2 Measurement results

5.2.1 Measured reflectivities for the materials

The absorber material samples included in the non-specular tests are TK THz RAM, TERASORB-500, FIRAM-500, Eccosorb VFX-NRL-2, and Bauhaus floor mat. Again, a polished flat aluminium plate is used as the calibration reference. The measured reflectivities shown in Figures 5.3–5.14 are all normalised to the reflection maxima from the flat plate. In order to be able to distinguish the directly coupled power from the scattered power, each figure also shows the ‘no target’ –curve measured with the horns facing free space.

The measured scattered powers into non-specular angles by the absorbers bring out much more information about their real performance than just the specular reflectivity measurements. This knowledge is essential in planning the orientation of the absorber panels in a large CATR facility or a RCS model range.

At 300 GHz with an incident angle of 26.5° and vertical polarisation (Figure 5.3), the TERASORB and FIRAM materials with horizontal grooves have the best

performance. TERASORB has a maximum scattered power level of -30 dB at normal incidence, after which it decreases constantly. The scattered power from FIRAM is always below -27 dB. TK THz RAM has scattered power levels below -25 dB, with a sharp dip of -55 dB at 34° . Several resonant maxima are observed at higher receiving angles. The wedged absorbers mounted with vertical groove direction, Eccosorb, and Bauhaus floor mat behave like diffuse scatterers, and have wide angular power spectrum with periodic minima and maxima. The directly coupled power between the antennas limits the highest useful receiving angle to 80° .

At horizontal polarisation (Figure 5.4), the strong directly coupled power level of -40 ... -50 dB masks out most scattering details. However, it is clear that the wedged absorbers with vertical grooves perform better than horizontal grooves near the specular angle, but scatter power over the whole measured angular range. The TK THz RAM curve is distorted by the directly coupled power, and not much can be said about it. The Eccosorb and Bauhaus floor mat scatter power over all the measured angular range, with periodic minima and maxima between -20 dB and -40 dB.

Figure 5.5 shows the results with an incident angle of 45° and vertical polarisation. The TK THz RAM has a deep scattering minimum of -42 dB near the specular angle, but strong maxima of -25 dB at $\pm 10^\circ$ separation. In addition, periodic maxima are observed at low and high angles. This material is clearly optimised for specular reflection only. The TERASORB with horizontal grooves shows scattered powers lower than -30 dB at all angles. The scattered power decreases smoothly on both sides of the specular angle. With vertical grooves, TERASORB's performance degrades by over 10 dB and maxima appear at both high and low angles. The FIRAM with horizontal grooves shows almost similar performance as TERASORB, but with 2–3 dBs higher measured scattering maximum. The Eccosorb and Bauhaus floor mat have periodic minima and maxima between -20 and -40 dBs. Directly coupled power limits the useful receiving angle to about 75° .

The low sidelobes of the corrugated horn pair are evident from Figure 5.6, which shows the horizontally polarised results for incident angle of 45° . The directly coupled power spectrum is almost identical to the one at vertical polarisation, and limits the useful receiving angle to 70° . TK THz RAM has a deep minimum of -57 dB at the specular angle. The measured curve also has several periodic maxima, the highest of which reaches -25 dB near 60° . TERASORB with horizontal grooves shows scattered powers below -30 dB, which in addition decrease smoothly. The same material with vertical grooves has a wide nonsymmetrical scattering response, which stays below -27 dB over the tested angles. Scattered power from FIRAM with horizontal grooves stays below -33 dB, and has a smoothly decreasing behaviour. The measured curve for FIRAM with vertical grooves is quite similar to that for TERASORB, and stays below -30 dB over the tested angles. Again, Eccosorb and Bauhaus floor mat have wide angular spectra with periodic minima and maxima.

Figure 5.7 shows the measured scattered powers with an incident angle of 63.4° and vertical polarisation. The directly coupled power increases rapidly after 70° , and limits the useful maximum receiving angle to 75° . TK THz RAM has several periodic scattering minima and maxima between -16 dB and -60 dB, and local minimum of -27 dB at the specular angle. TERASORB with horizontal grooves has the best

performance in this case, and its measured scattered power level stays below -20 dB over the tested angular range. The scattered power from TERASORB with vertical grooves stays below -10 dB, but at small angles has considerably higher power levels than that with horizontal grooves. FIRAM with horizontal grooves shows power levels below -15 dB, and good performance (below -50 dB) at low angles. The measured curve with vertical grooves is almost identical to the one for TERASORB, staying below -12 dB and has wide angular spectrum. Eccosorb and Bauhaus floor mat have strong periodic minima and maxima between $-15\dots-50$ dB over the tested angles.

The horizontally polarised results for an incident angle of 63.4° are shown in Figure 5.8. Again, direct coupling between the antennas limits the maximum receiving angle to about 75° . The scattered power from TK THz RAM stays always below -15 dB, and several maxima and minima are observed. Reflectivity into the specular direction is -25 dB. TERASORB with horizontal grooves has a scattered power maximum of about -18 dB at 75° , and it decreases rapidly when going to smaller angles. TERASORB with vertical groove direction has the same maximum power, but the received power level stays 10-15 dB higher at small angles than with horizontal grooves. FIRAM with horizontal grooves performs the best in this figure, the power level of which staying always below -20 dB and decreasing rapidly at smaller angles. The same with vertical grooves stays below -18 dB, but has strong scattering at small angles. Bauhaus floor mat and Eccosorb have periodic minima and maxima between $-20\dots-50$ dB.

At 400 GHz, the beams patterns of the corrugated horns at vertical and horizontal polarisations are not identical. The horizontally polarised pattern is considerably wider, causing the directly coupled power level to increase at larger angles. Figure 5.9 shows the vertically polarised results for an incident angle of 26.5° . TERASORB and FIRAM with horizontal grooves have the best performance, the scattered signals of which stay below -28 dB (FIRAM) and -31 dB (TERASORB) and decrease rapidly. The same materials with vertical grooves scatter power into a wide angular range at levels below -22 dB. Scattering from TK THz RAM stays below -30 dB, but power is spread to a wide angular range. Periodic minima and maxima from Eccosorb and Bauhaus floor mat are observed between $-22\dots-50$ dB.

The horizontally polarised results for an incident angle of 26.5° are shown in Figure 5.10. The directly coupled power limits the useful maximum angle to 85° . Again, TERASORB and FIRAM with horizontal grooves have the best performance, with scattered power levels below -30 dB and decreasing rapidly. The same materials with vertical grooves have scattered powers below -30 dB, but also high 'sidelobes' at angles between $70\dots80^\circ$ and resonant-like periodic minima and maxima between $30\dots50^\circ$. TK THz RAM has scattered powers below -31 dB, and has several periodic minima and maxima between $-31\dots-65$ dB in the tested angular range. The scattering maximum is to an angle of 37° which is ten degrees off from the specular angle. Bauhaus floor mat has periodic scattering minima and maxima between $-19 \dots-46$ dB, and Eccosorb between $-24\dots-60$ dB.

Figure 5.11 shows the measured scattered powers for an incident angle of 45° and vertical polarisation. Direct coupling between the horns limits the useful angular range to $5^\circ \dots 85^\circ$. TK THz RAM has strong periodic minima and maxima between $-60\dots-30$

dB. A local scattering minimum from the sample is observed in the specular direction of 45° , and maximum at 52° . TERASORB and FIRAM with horizontal grooves have similar scattering properties; the scattered power levels stay below -29 dB and -27 dB, respectively, and decrease rapidly when moving away from the specular direction. The same materials with vertical grooves have scattered power levels below -20 dB and -23 dB, and have strong 'sidelobes' at $10^\circ \dots 20^\circ$. Eccosorb has periodic minima and maxima between $-22 \dots -48$ dB, and Bauhaus floor mat between $-19 \dots -45$ dB.

Results for horizontal polarisation and incident angle of 45° are shown in Figure 5.12. Strong direct coupling is observed at large angles, and the useful maximum angle is limited to about 65° . TK THz RAM has periodic minima and maxima between $-35 \dots -60$ dB. TERASORB with horizontal grooves has scattered power levels below -27 dB which decrease quickly to the noise level. The same material with vertical grooves stays below -30 dB, and has a wide angular spectrum. FIRAM with horizontal grooves has scattered power levels below -29 dB which decrease quickly. Scattered power distribution from FIRAM with vertical grooves is wide and non-symmetrical, the maximum of which is -28 dB at 15° . Eccosorb has periodic minima and maxima between $-19 \dots -55$ dB, and Bauhaus floor mat between $-15 \dots -40$ dB.

Figure 5.13 shows the scattering results for 400 GHz, vertical polarisation, and an incident angle of 63.4° . The useful angle range is limited to $0^\circ \dots 80^\circ$, again by the direct coupling effects. TK THz RAM has scattered powers below -20 dB, and strong periodic peaks, e.g., at 2° , 57° , 74° , and 83° . The scattered power by TERASORB with horizontal grooves stays below -27 dB, and decreases rapidly to smaller angles. TERASORB with vertical grooves scatters power levels below -11 dB, and a wide angular power spectrum. FIRAM with horizontal grooves features scattered powers below -20 dB which rapidly decrease close to noise level at small angles. Eccosorb and Bauhaus floor mat scatter power over a wide angular range, and periodic minima and maxima are observed between $-15 \dots -46$ dB.

Finally, the horizontally polarised results for incident angle of 63.4° are shown in Figure 5.14. The results are meaningful up to about 70° , after which the strong directly coupled signal masks out any scattering phenomena. TK THz RAM has several periodic peaks in the measured angular power spectrum, the highest of which are at a level of -15 dB. Scattered power from TERASORB with horizontal grooves stays below -22 dB, and decreases rapidly to the noise level at small angles. The same material with vertical grooves has scattered powers below -15 dB. FIRAM with horizontal grooves performs better than TERASORB, the scattering staying below -30 dB and decreasing rapidly to noise level at small angles. FIRAM with vertical grooves scatters below -20 dB. Eccosorb and Bauhaus floor mat have periodic minima and maxima between $-20 \dots -60$ dB.

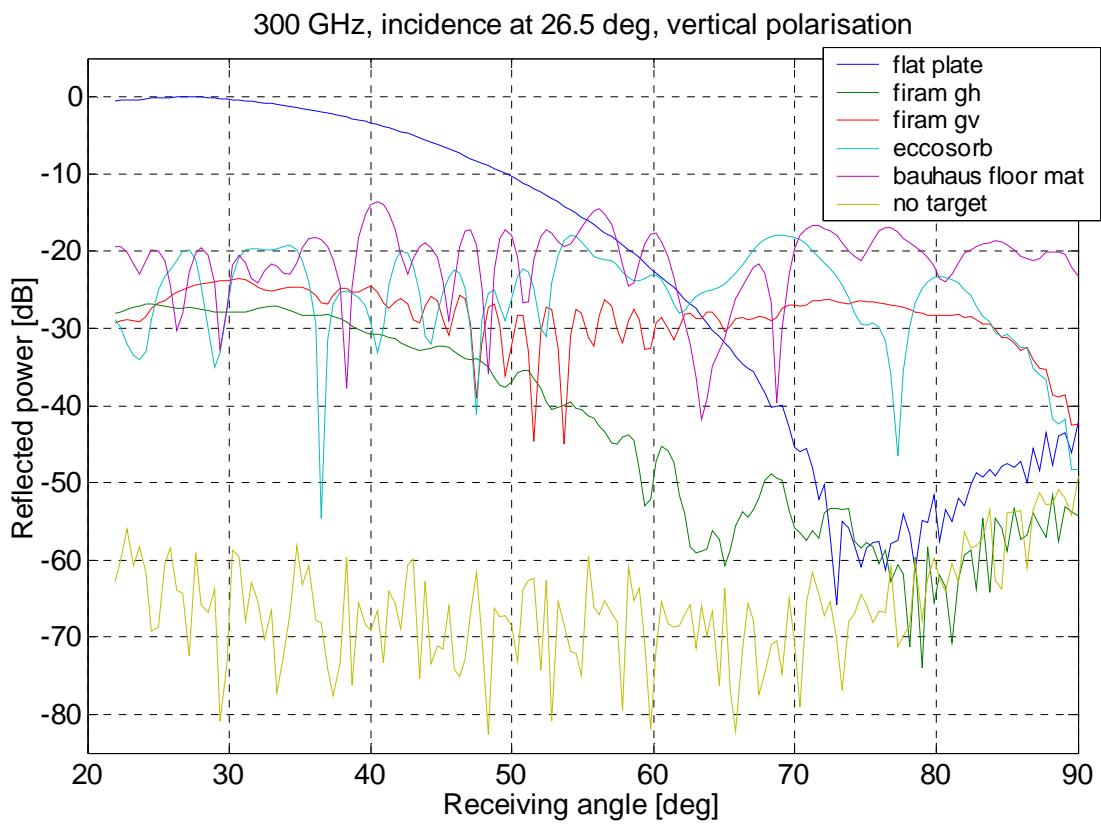
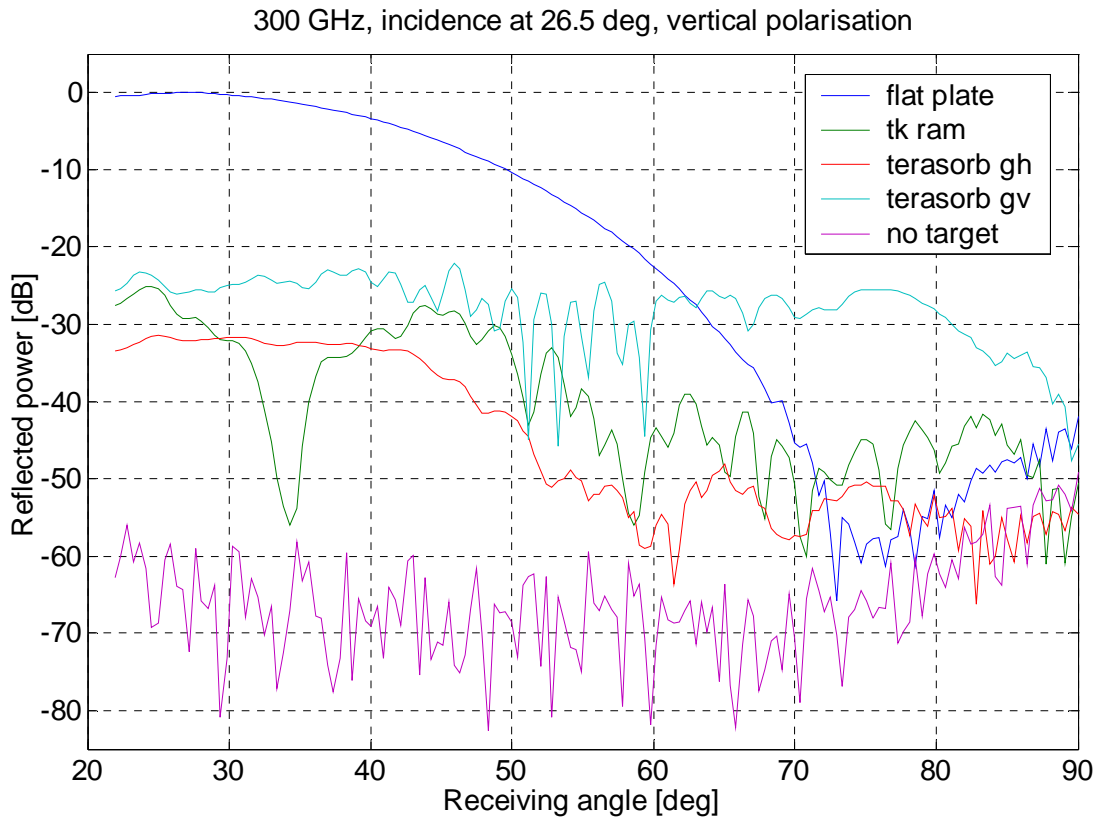


Figure 5.3 Scattered power as a function of the receiving angle (vertical polarisation at 300 GHz, $\theta_i = 26.5^\circ$).

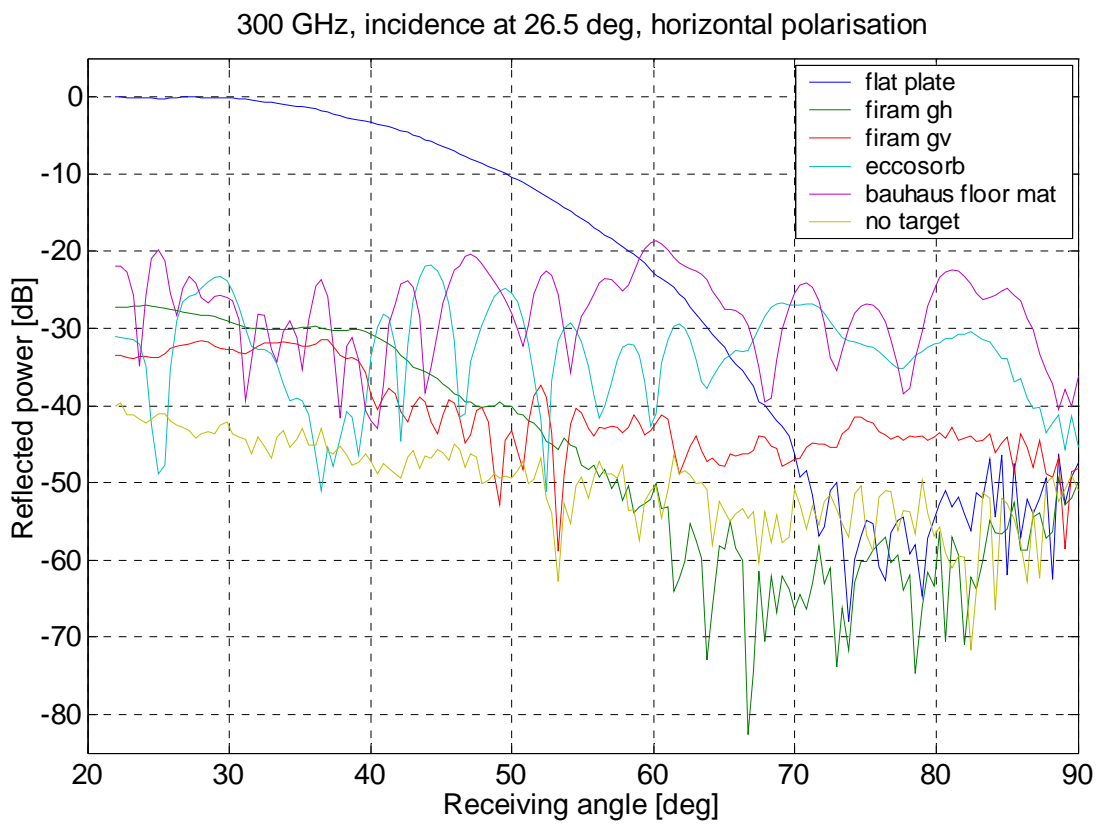
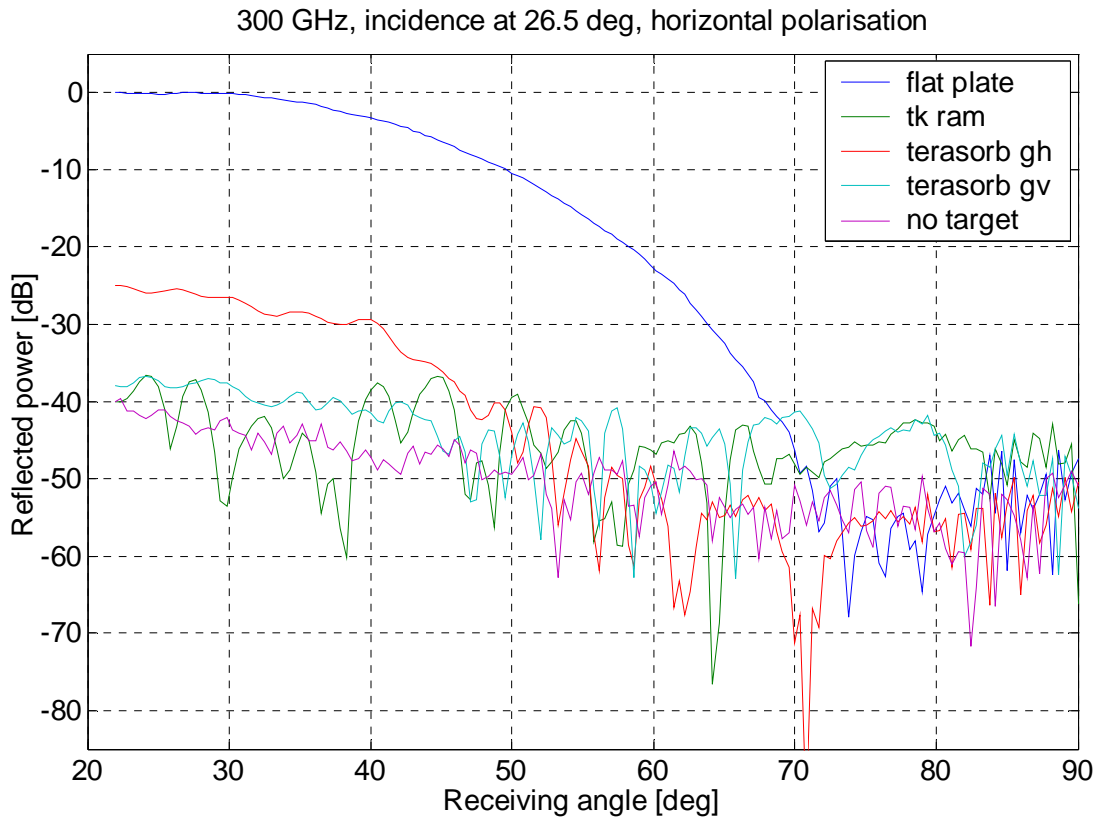


Figure 5.4 Scattered power as a function of the receiving angle (horizontal polarisation at 300 GHz, $\theta_i = 26.5^\circ$).

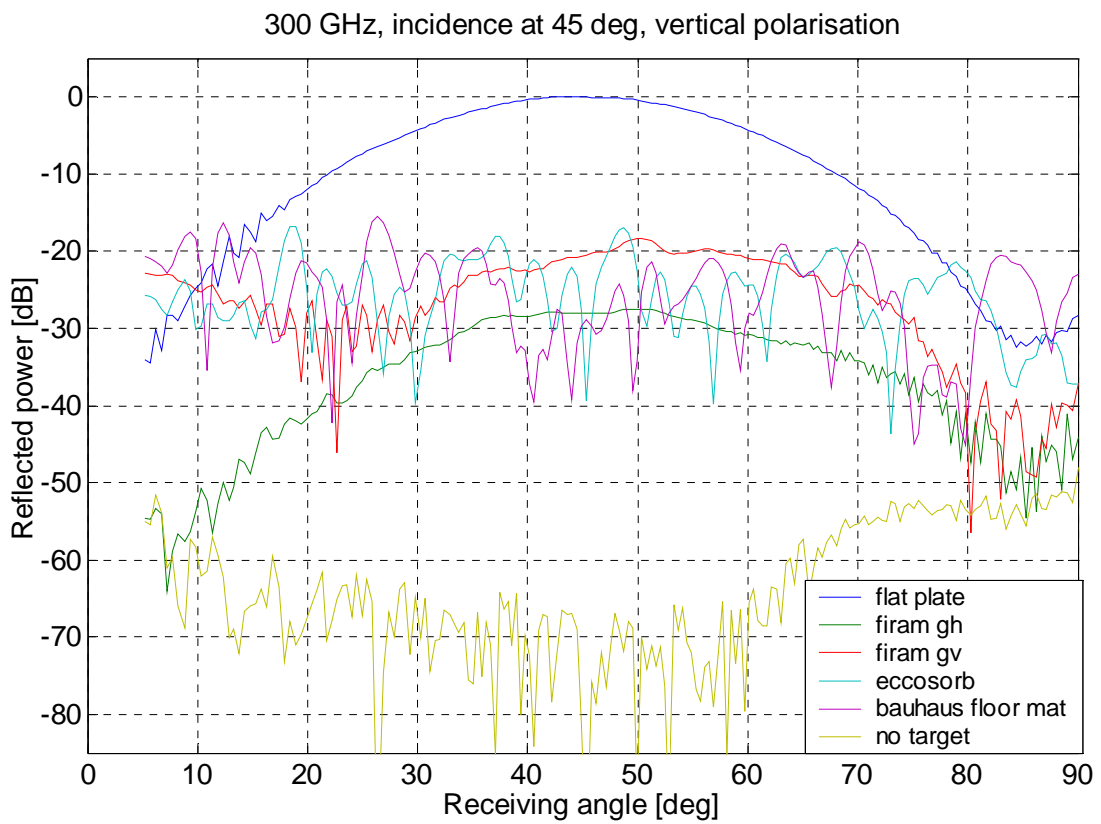
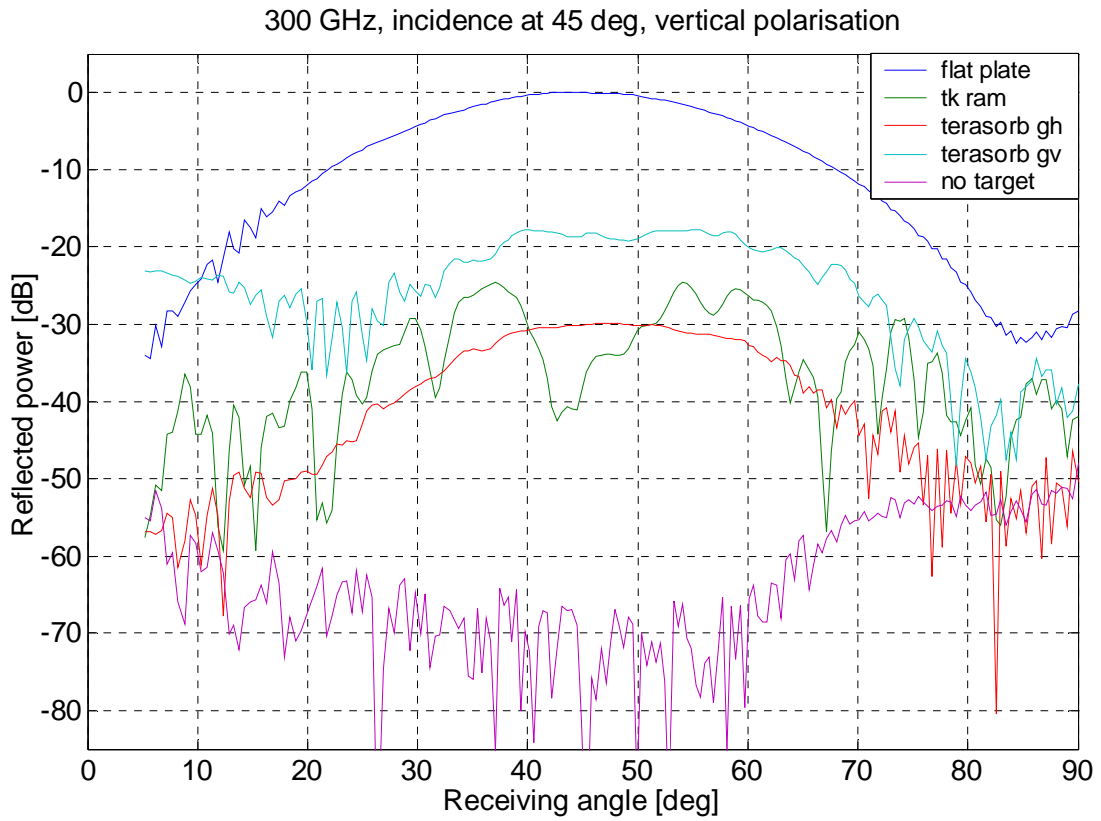


Figure 5.5 Scattered power as a function of the receiving angle (vertical polarisation at 300 GHz, $\theta_i = 45^\circ$).

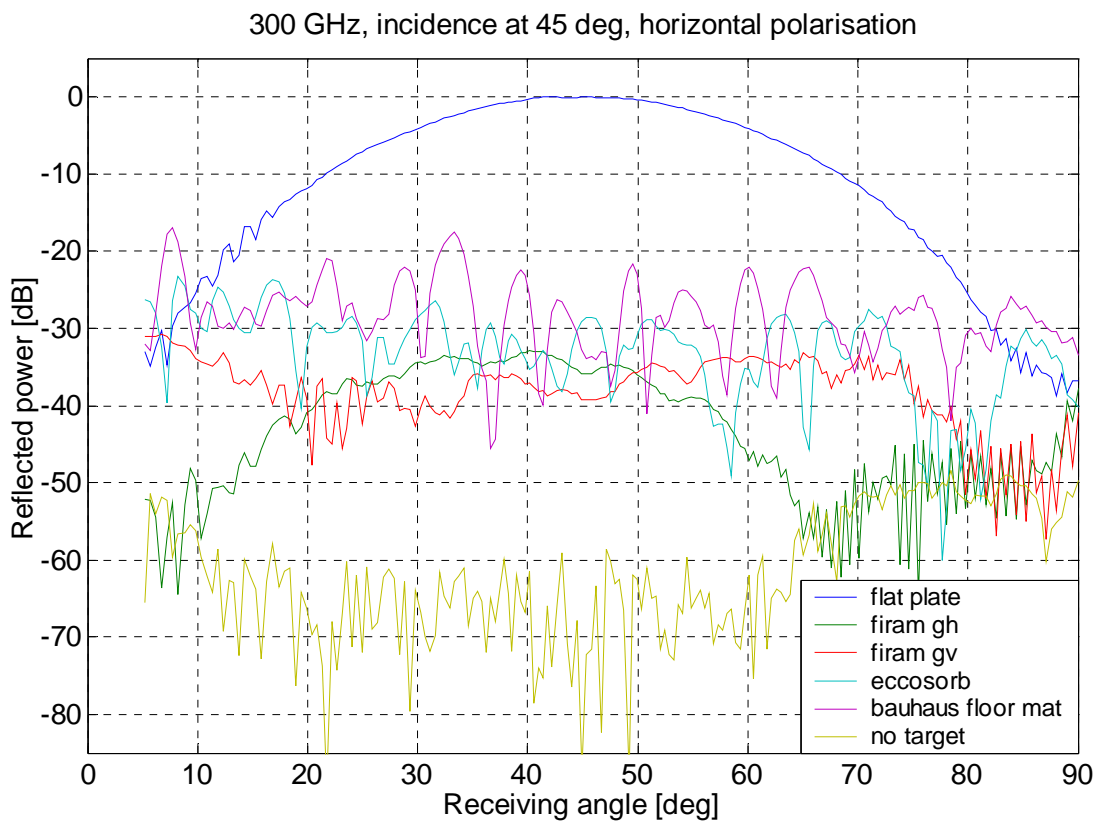
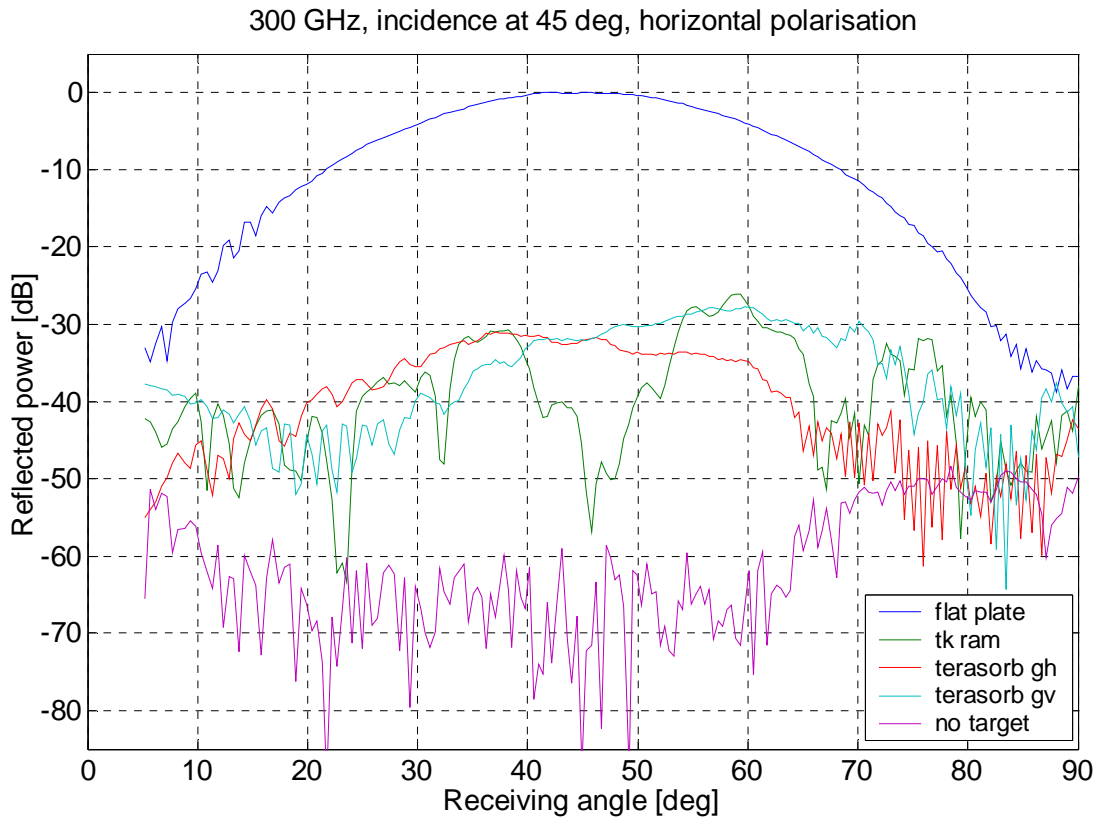


Figure 5.6 Scattered power as a function of the receiving angle (horizontal polarisation at 300 GHz, $\theta_i = 45^\circ$).

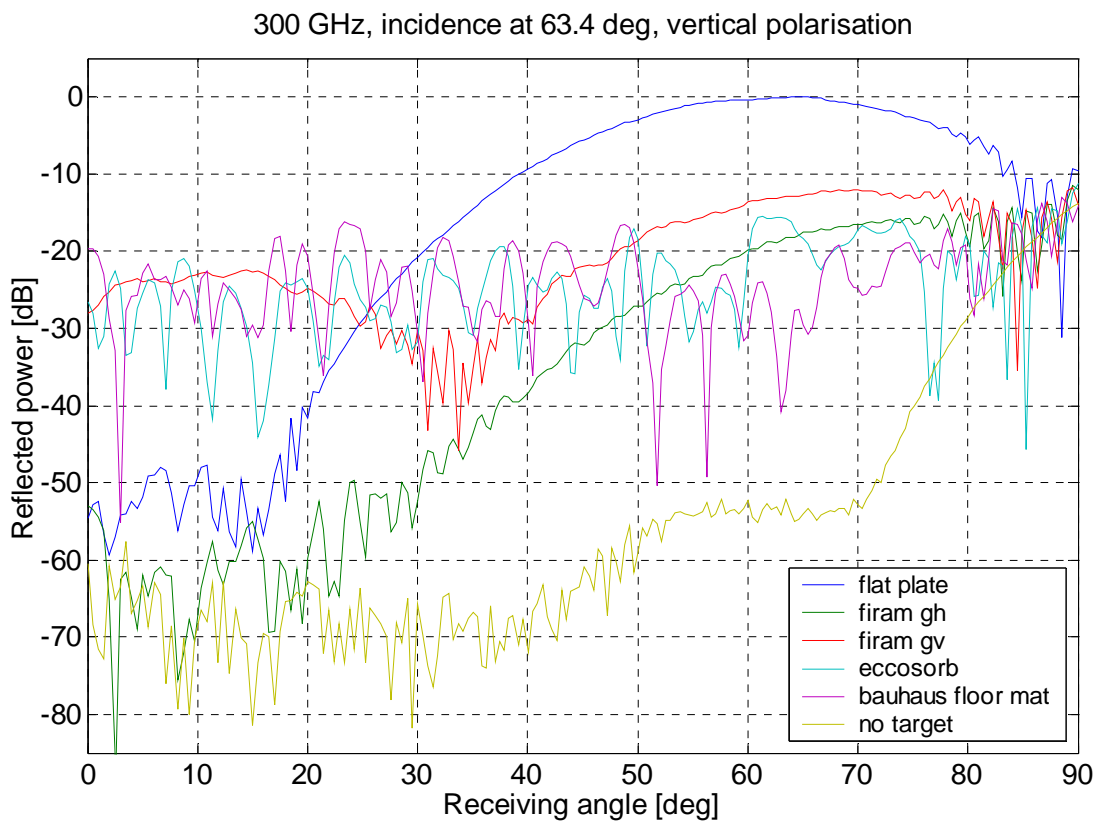
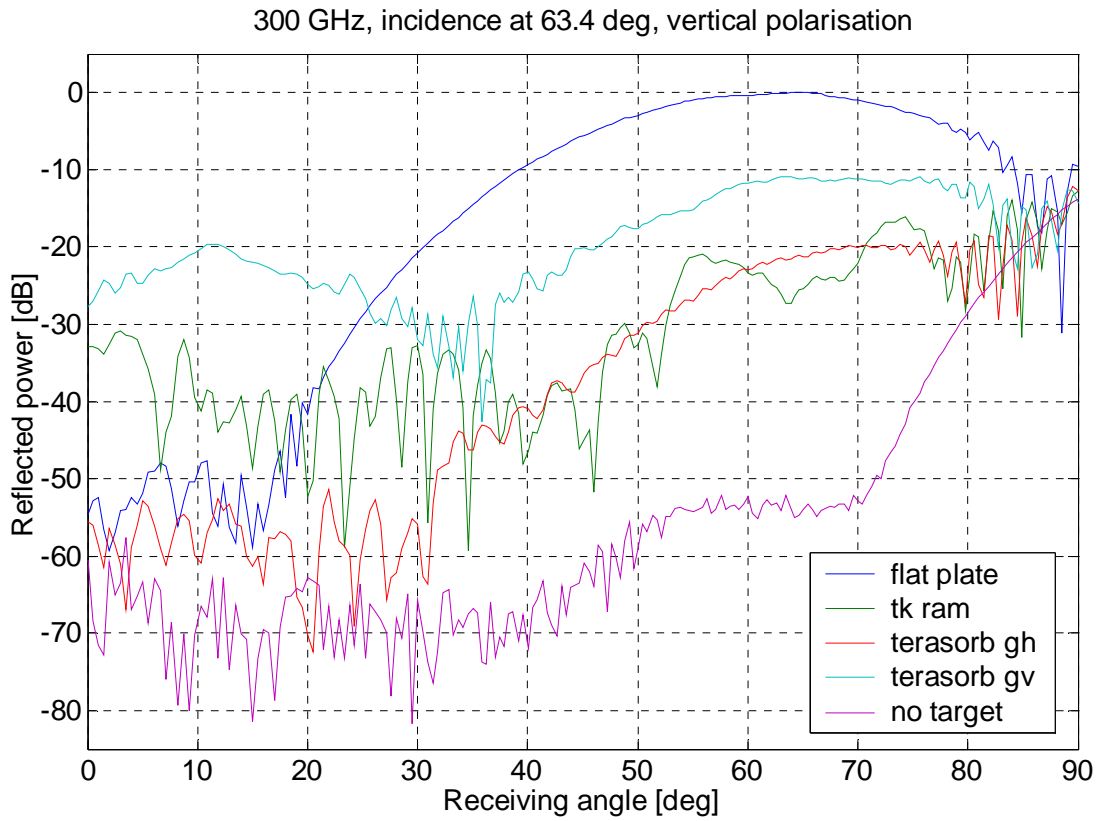


Figure 5.7 Scattered power as a function of the receiving angle (vertical polarisation at 300 GHz, $\theta_i = 63.4^\circ$).

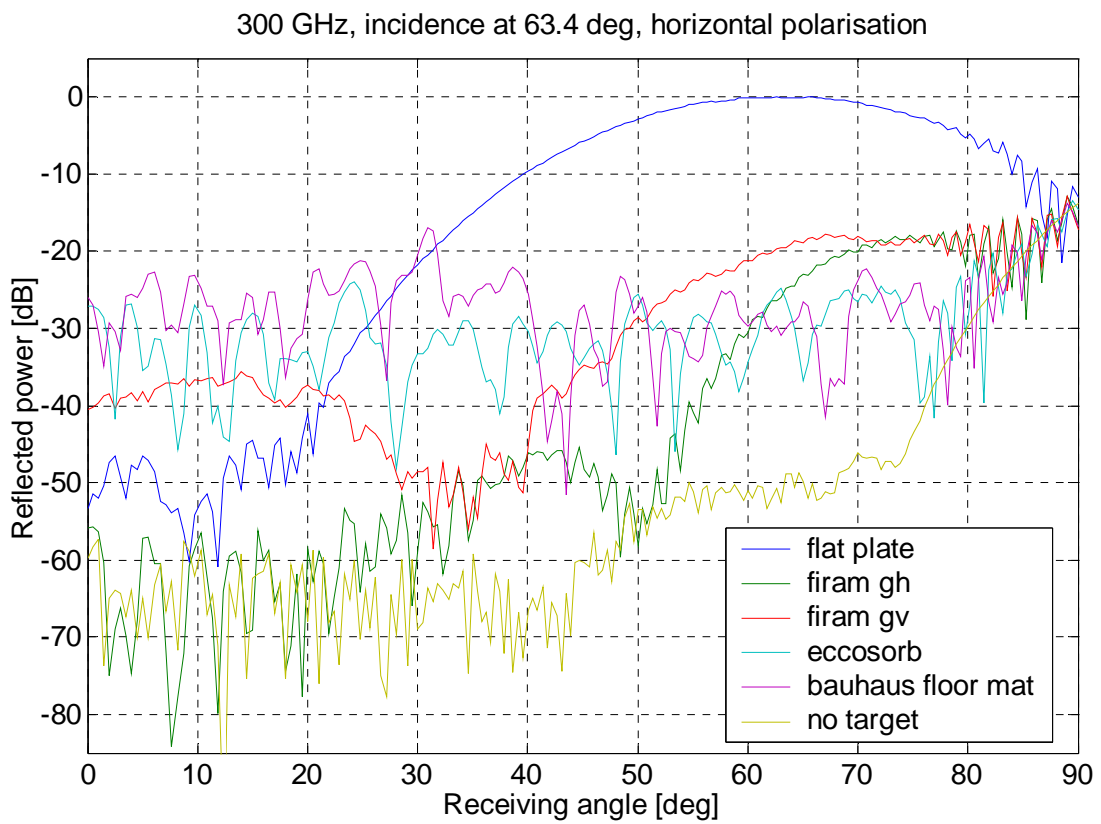
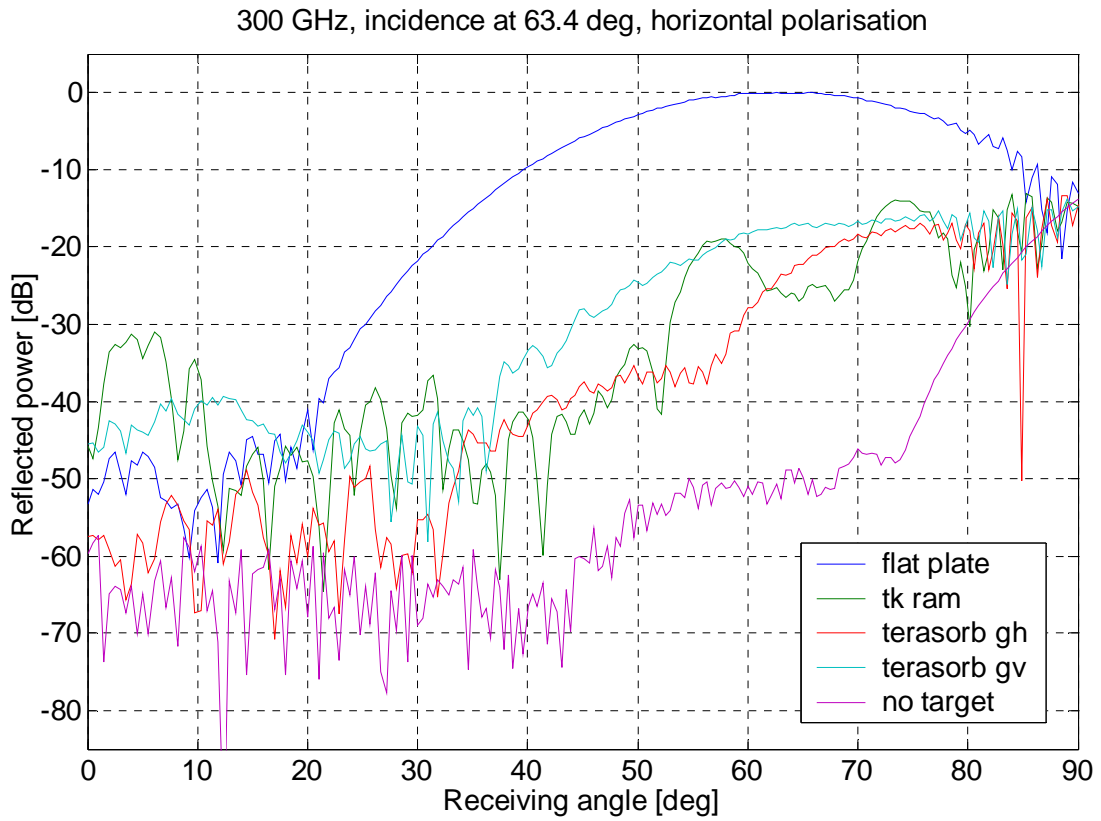


Figure 5.8 Scattered power as a function of the receiving angle (horizontal polarisation at 300 GHz, $\theta_i = 63.4^\circ$).

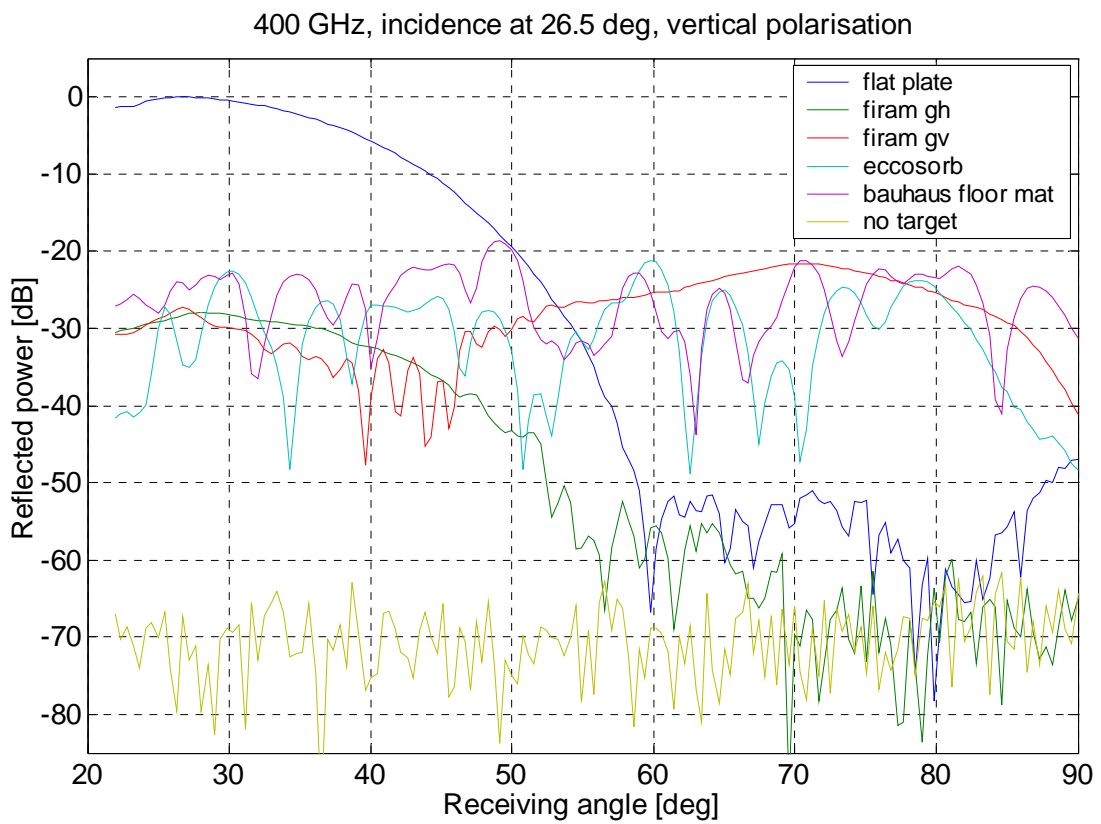
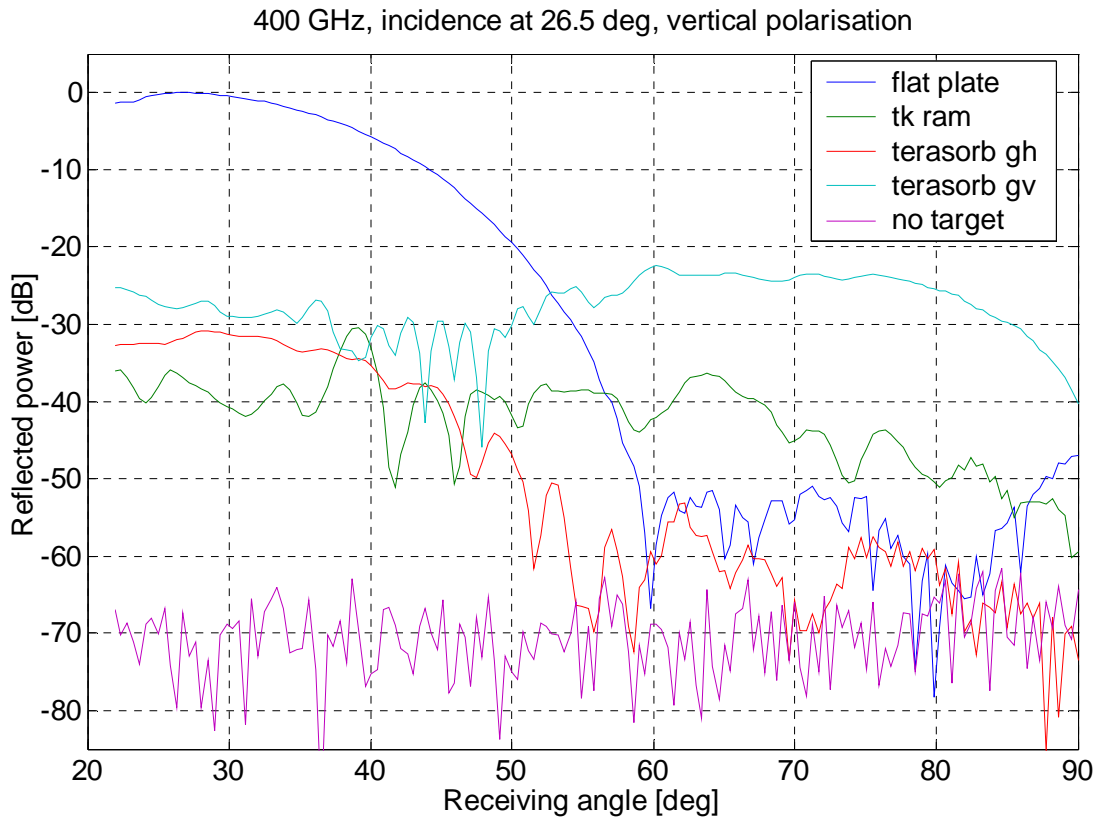


Figure 5.9 Scattered power as a function of the receiving angle (vertical polarisation at 400 GHz, $\theta_i = 26.5^\circ$).

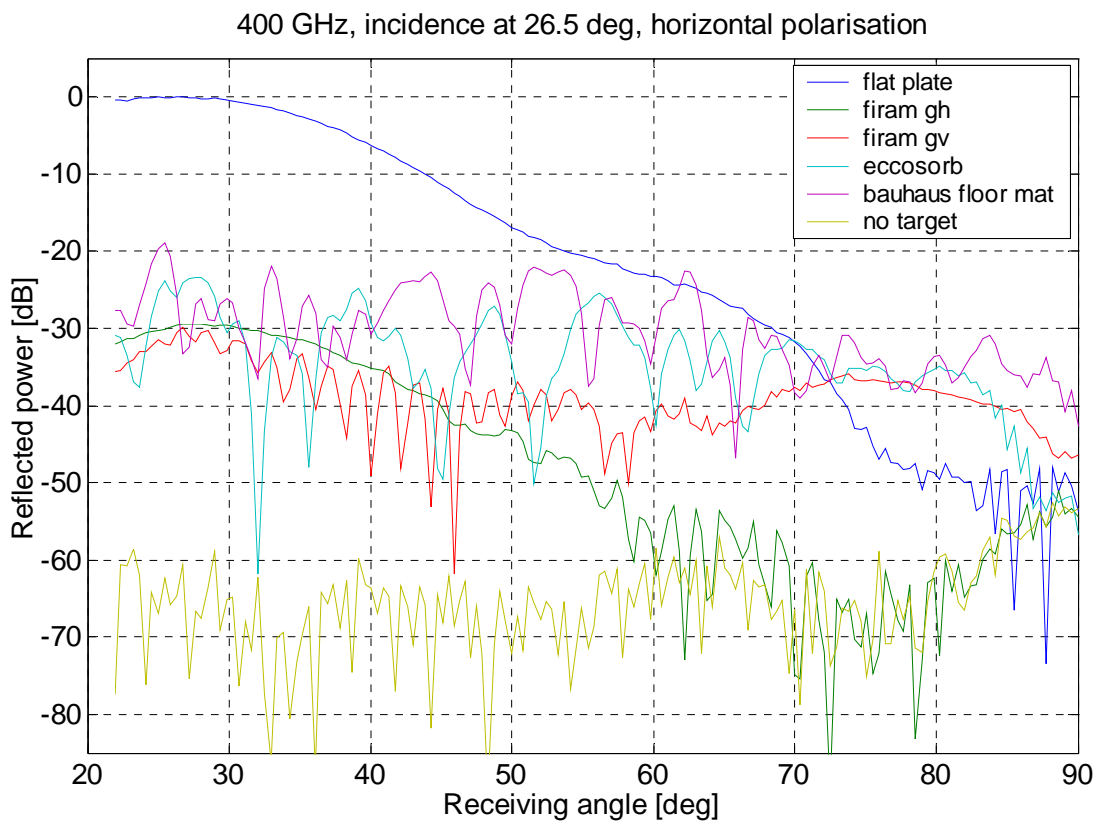
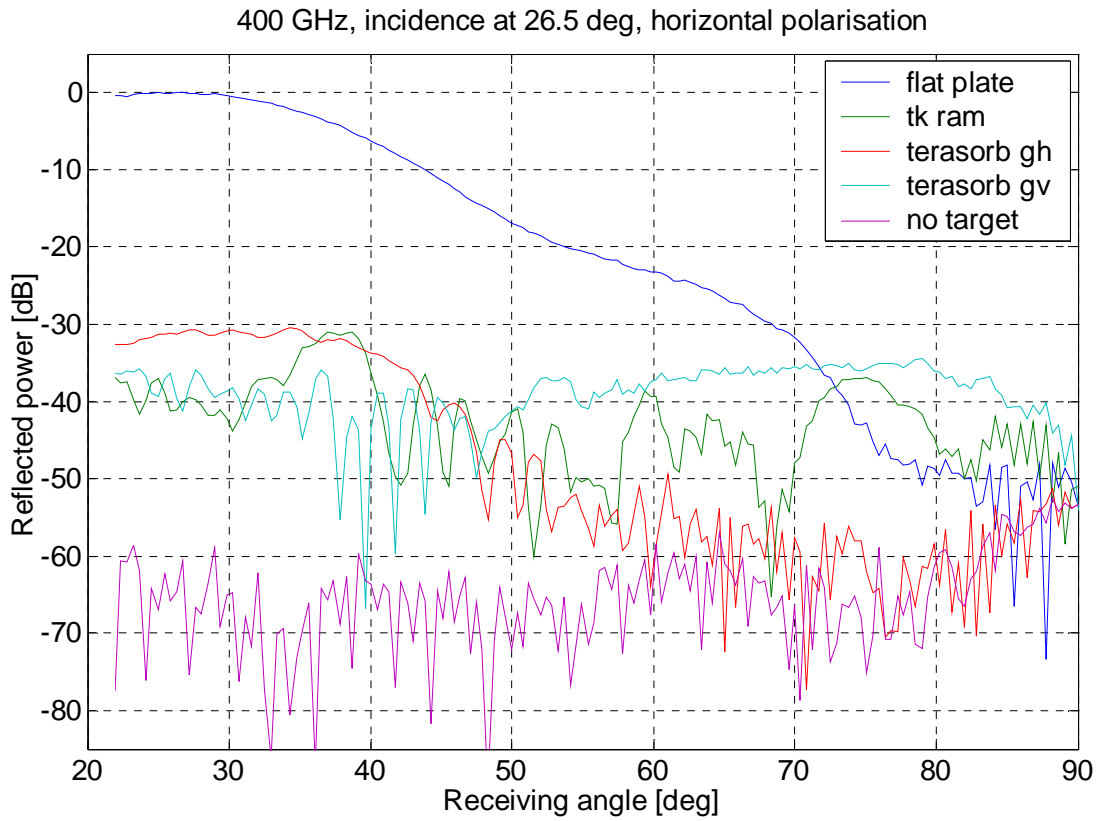


Figure 5.10 Scattered power as a function of the receiving angle (horizontal polarisation at 400 GHz, $\theta_i = 26.5^\circ$).

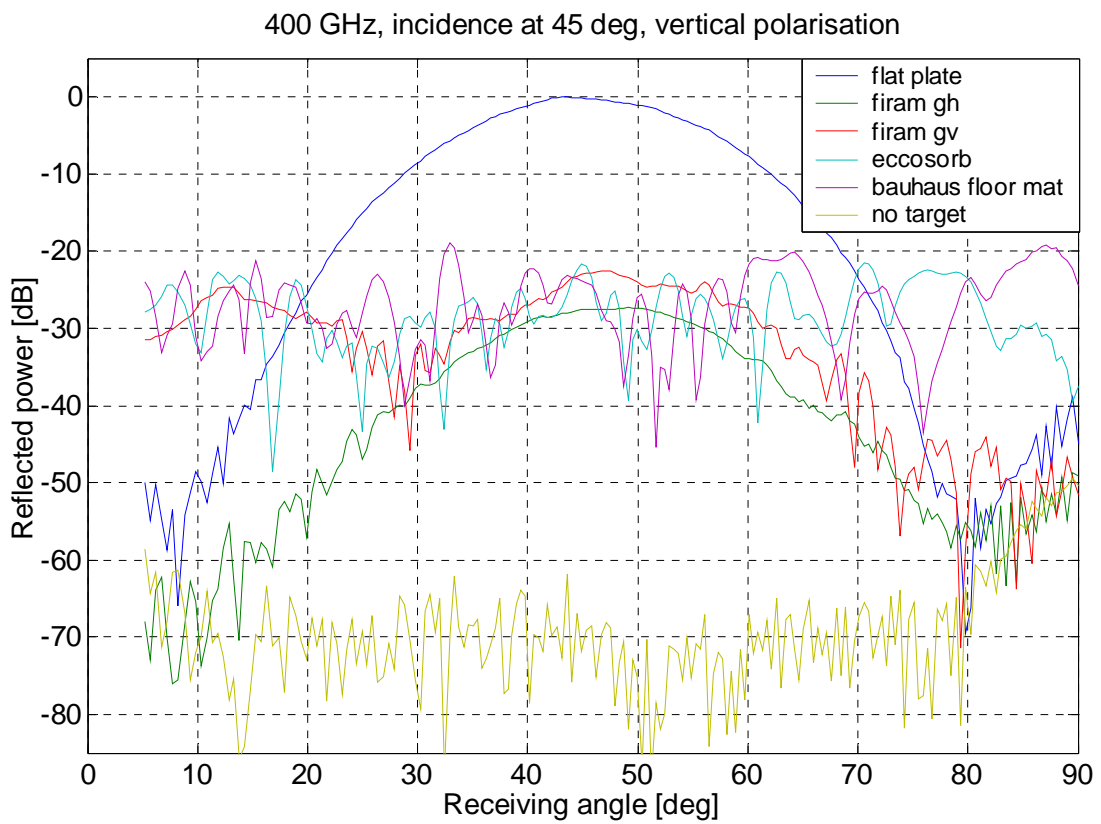
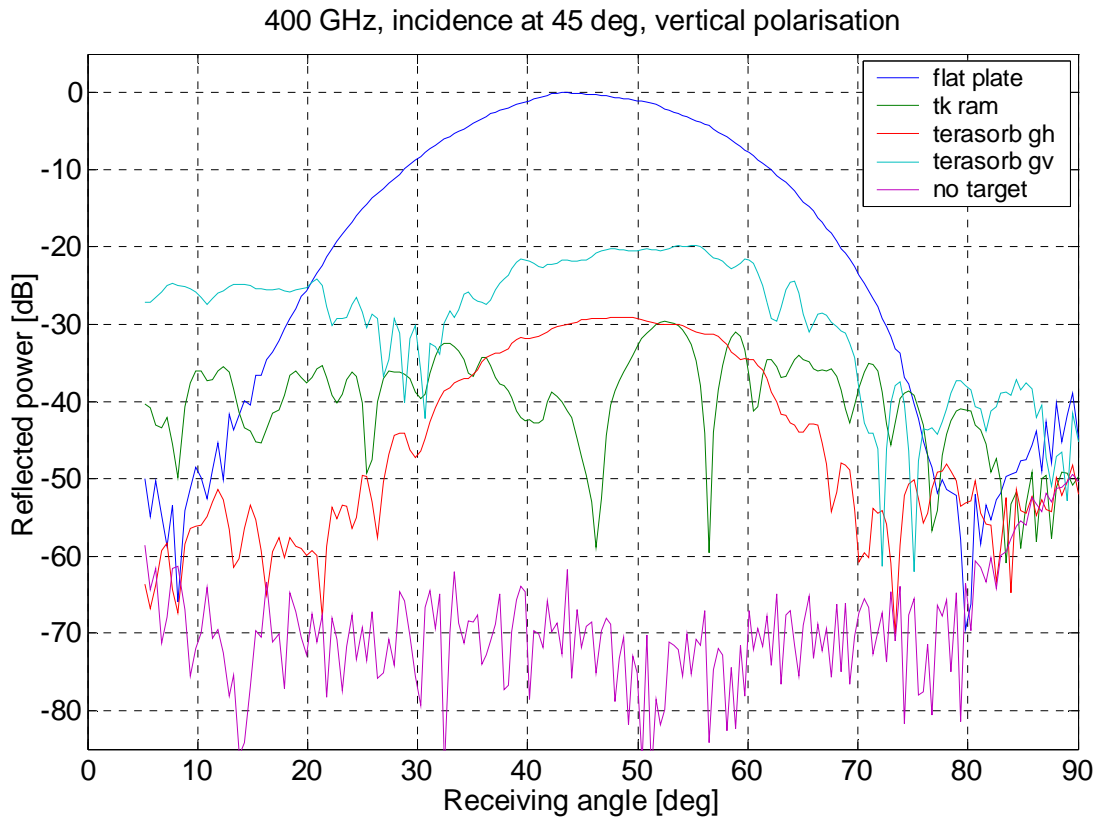


Figure 5.11 Scattered power as a function of the receiving angle (vertical polarisation at 400 GHz, $\theta_i = 45^\circ$).

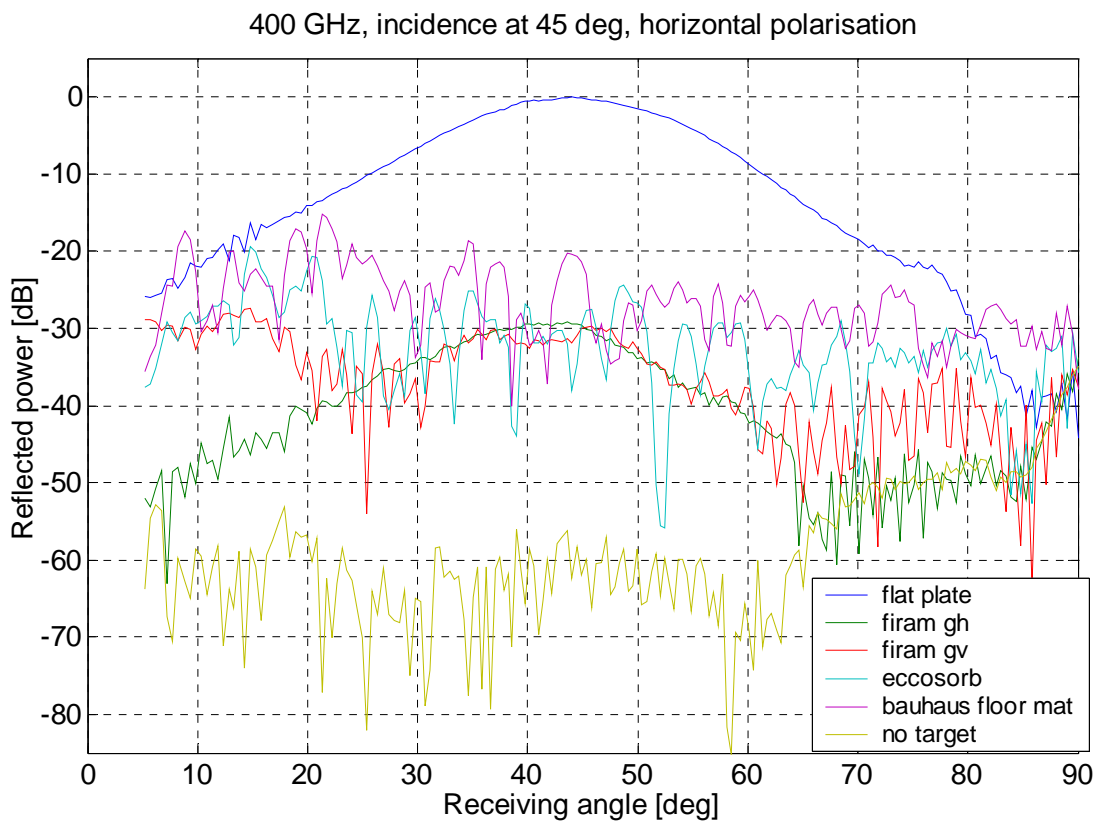
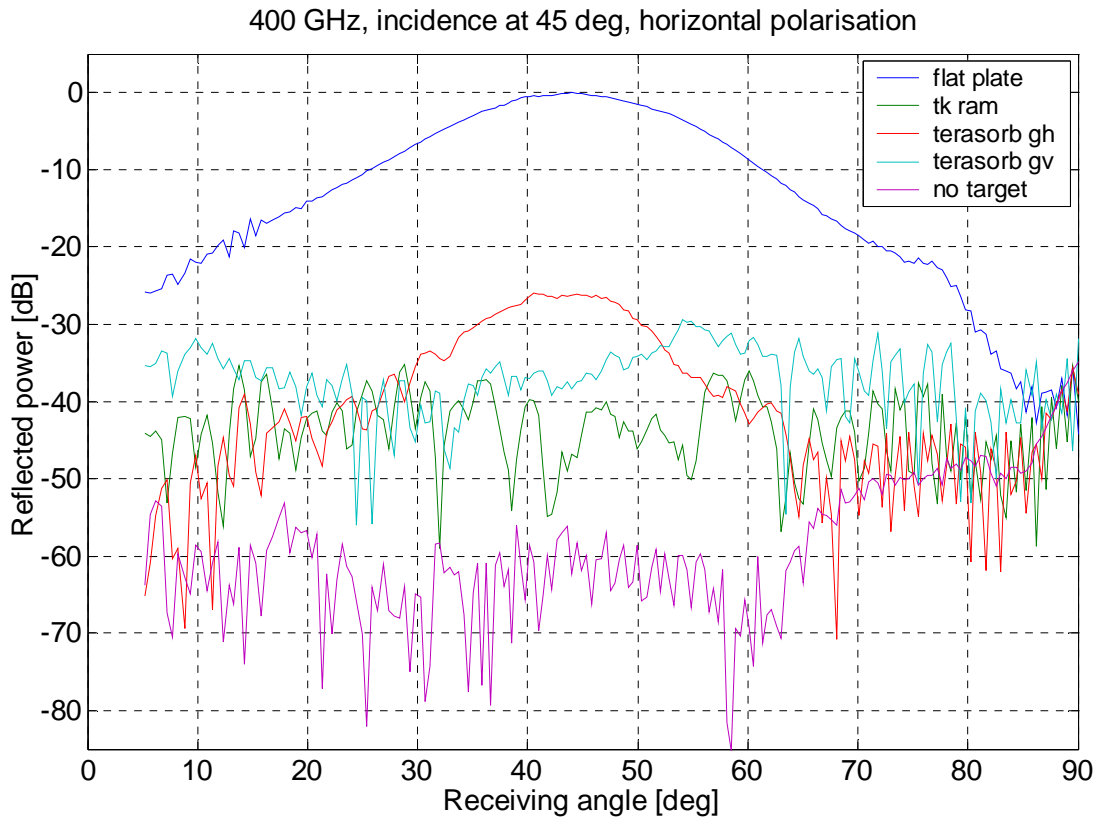


Figure 5.12 Scattered power as a function of the receiving angle (horizontal polarisation at 400 GHz, $\theta_i = 45^\circ$).

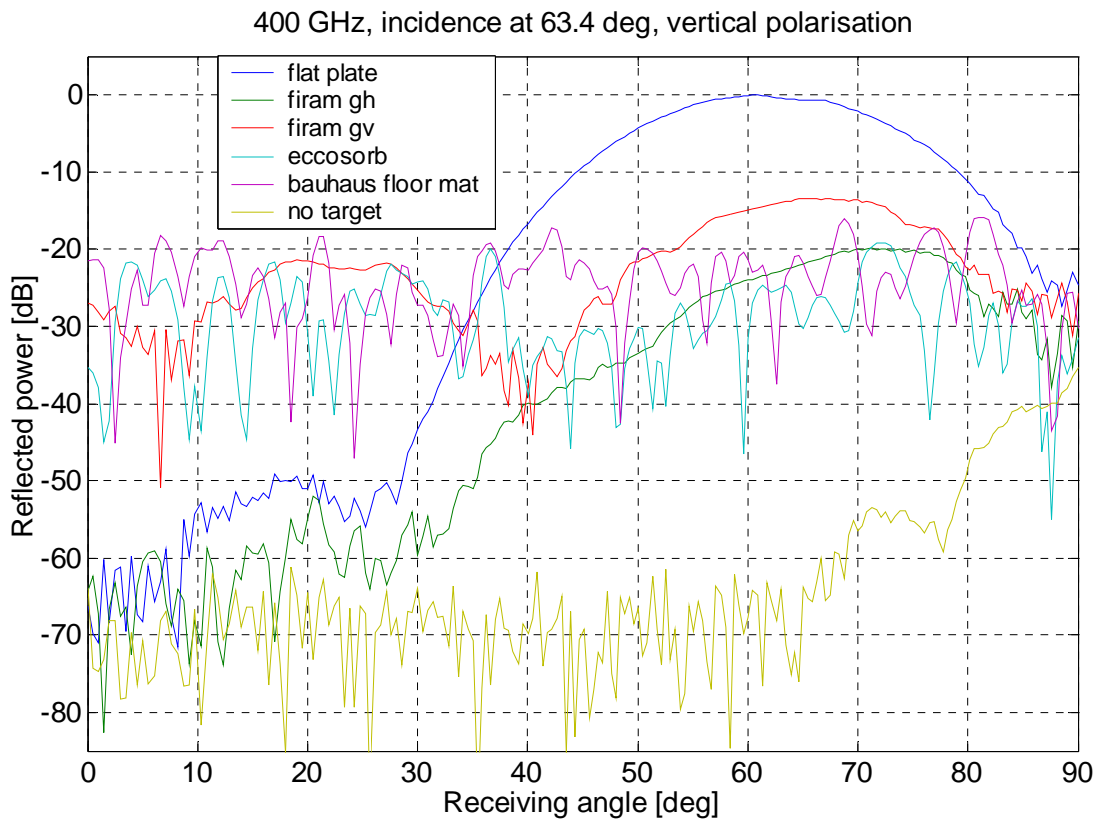
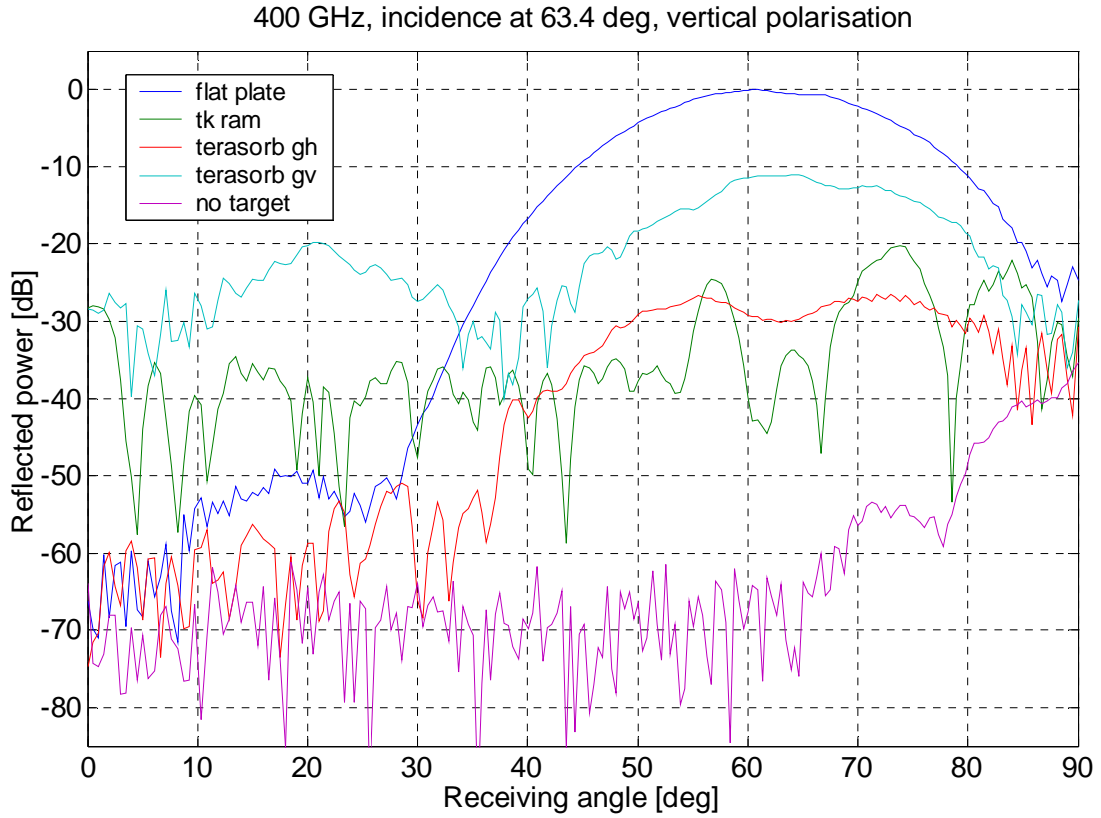


Figure 5.13 Scattered power as a function of the receiving angle (vertical polarisation at 400 GHz, $\theta_i = 63.4^\circ$).

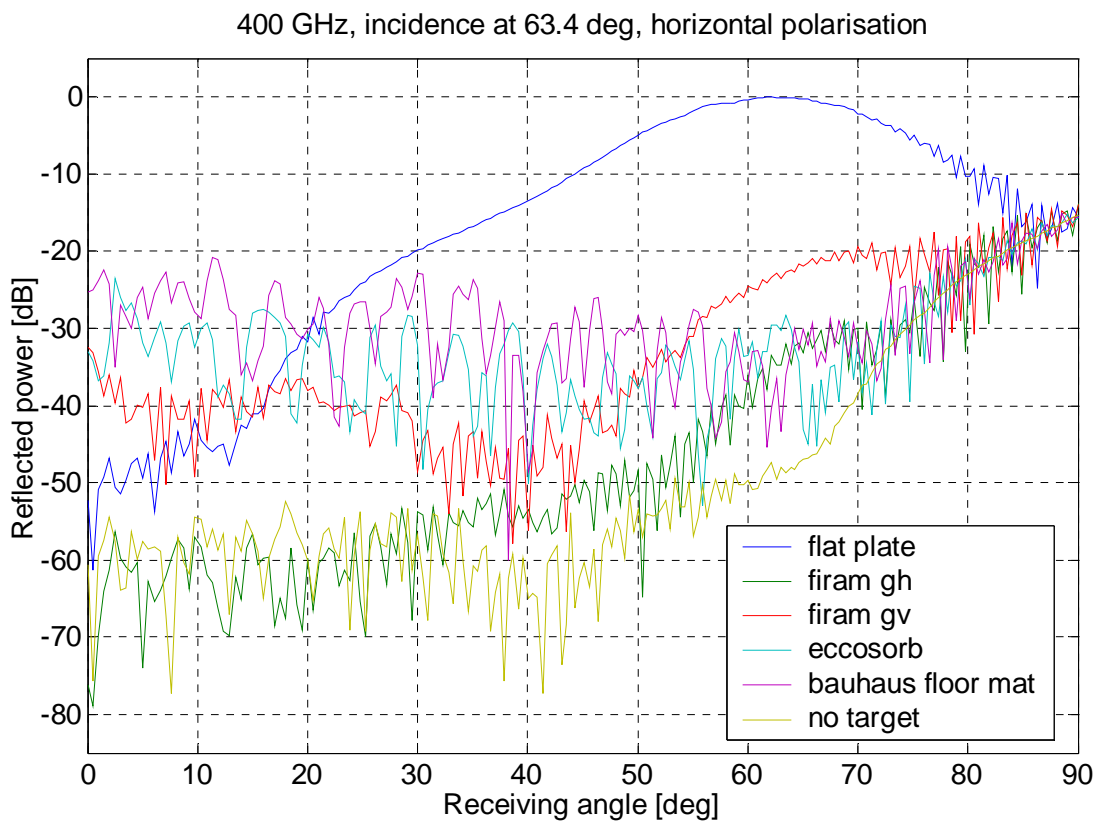
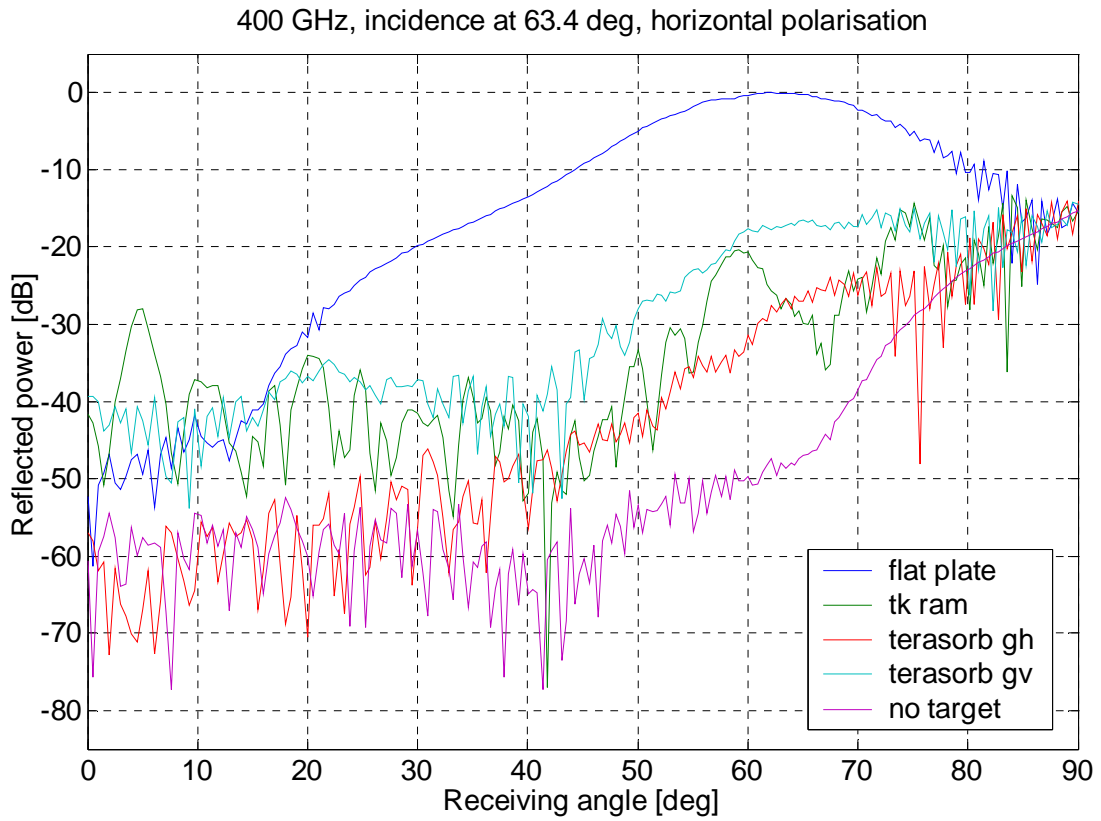


Figure 5.14 Scattered power as a function of the receiving angle (horizontal polarisation at 400 GHz, $\theta_i = 63.4^\circ$).

5.2.2 Effect of non-idealities

5.2.2.1 Direct coupling between the horn antennas

The pyramidal horn which is used at the receiver at 300 GHz with incident angle of 26.5° causes large direct coupling at horizontal polarisation. As mentioned earlier, a second (identical) corrugated horn was acquired for measurements at other incidencies and frequencies, resulting in significantly improved directly coupled power floor.

Further problems with directly coupled signals arise at high incident and receiving angles due to the wide Gaussian beam of the corrugated feed horns. The horns are designed for -3 dB beamwidth of 20° at 300 GHz. The wide beam is required for illuminating radio holograms in the CATR application.

At 400 GHz, the vertically and horizontally polarised beams from the corrugated horn are no longer symmetrical to each other like at 300 GHz. This is evident from the flat plate curves in Figures 5.11 and 5.12, where the horizontally polarised beam is widened and no longer has a Gaussian shape. One must not do direct comparisons between the vertically and horizontally polarised data at 400 GHz. The measured scattered powers can still be used to compare different materials at the same polarisation, however.

5.2.2.2 Pointing errors

The same error estimates discussed in Section 4.3.2.3 are valid, i.e. repeatability of ± 2 dB. The angle zero position calibration is performed after each sweep, and possible errors in single sweeps are not cumulative.

5.2.2.3 Effect of the receiver's distance on the results

The distance of the absorber sample in the tests is only 7 cm, and in order to be convinced that near-field effects really are minimal, the reflected power as a function of the receivers linear distance was measured. The receiver is mounted to the linear scanner, and a laser beam reflected from the flat plate and pointing to a target at the transmitter is used to calibrate the straightness of the linear travel. Figure 5.15 shows the test setup, where frequency of 300 GHz, incident angle of 45° , and vertical polarisation were chosen for simplicity and mechanical convenience. The step size in the linear sweep is 0.11 mm which equals to about $\lambda/10$.

The measurement results are shown in Figure 5.16. The flat plate curve shows some ripple due to standing waves between the plate and the antennas. The measured curves for TERASORB, FIRAM, and TK THz RAM are relatively smooth, indicating that the measurement distance is long enough to suppress fast (near-field) variations in the received signal. The measured ripples in the TERASORB and FIRAM with horizontal grooves and the TK THz RAM curves are about ± 1 dB in amplitude, and are a combination of standing waves and not-yet-decayed near-field components scattered by the sample.

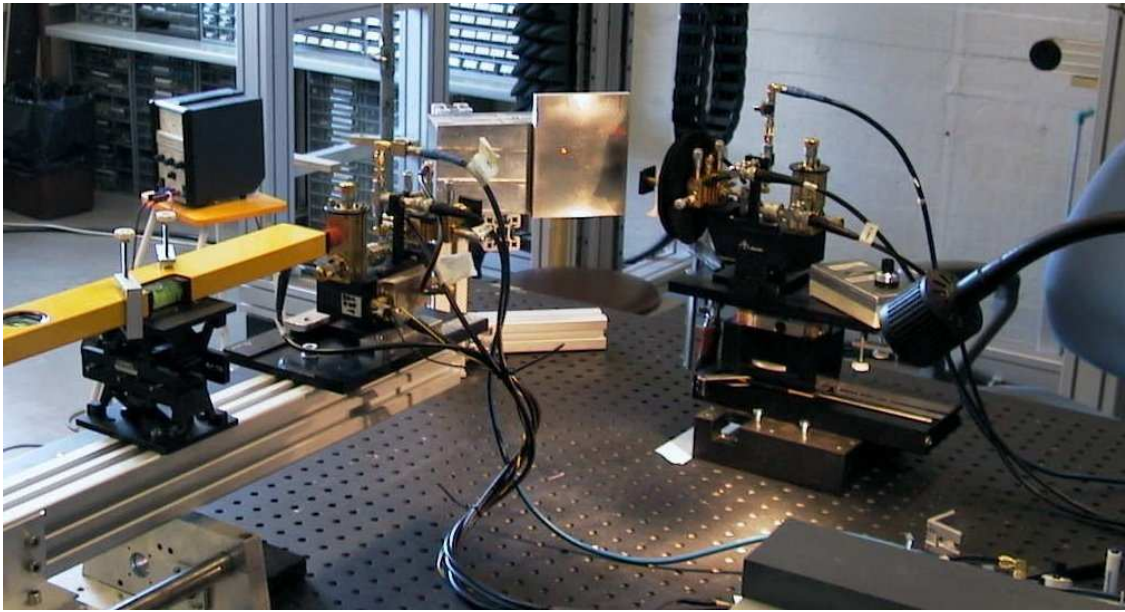


Figure 5.15 Test setup for varying the receivers linear distance from the sample.

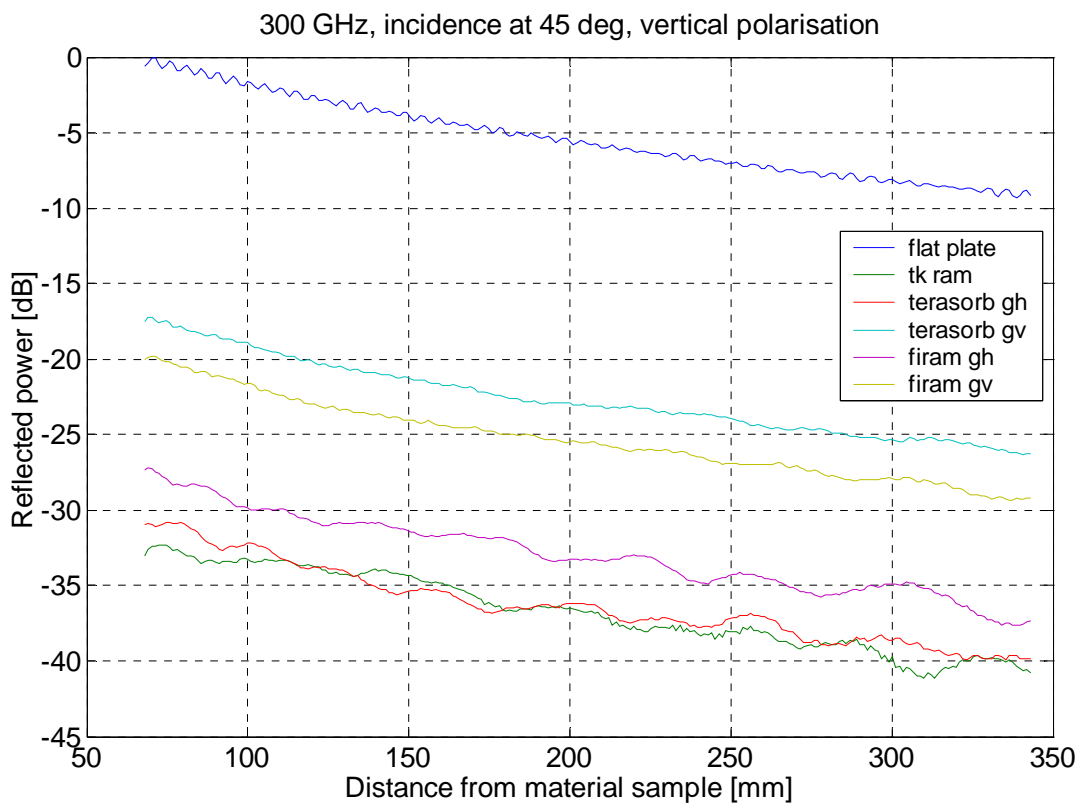


Figure 5.16 Reflected power as a function of the linear distance of the receiver from the sample (300 GHz, $\theta_i = \theta_o = 45^\circ$, vertical polarisation).

6 SUMMARY AND CONCLUSIONS

In this Report, the full angular scattering performance of several commercially available absorber materials (TK THz RAM, TERASORB-500, FIRAM-500, Eccosorb VFX-NRL-2) and some low-cost carpets (Bauhaus wool carpet, Bauhaus floor mat, Etola synthetic carpet) are presented. Specular scattering was measured between 200–600 GHz, and non-specular scattering between 300–400 GHz. Comparisons with the measured reflectivities in earlier studies with TK THz RAM [7,8] and FIRAM-500 [6,7] are made. In the author's view, this Report is the first publication in the open literature analyzing both the specular and non-specular scattering from a set of materials across a wide frequency range and has continuous angle coverage.

An introduction to the design of absorber materials is presented in Chapter 2. The loss mechanisms and principles of operation of single, multilayer and geometrical transition absorbing structures are discussed. Scattering theory, different scattering regimes, and simulation methods are presented in Chapter 3.

The constructed bistatic test bench for specular scattering measurements and the obtained results are presented in Chapter 4. The distance between the material sample and the receiver/transmitter horns is 7 cm. The measurements were performed between 200–600 GHz with a frequency step of 100 GHz. Angular range of the continuous angle sweep is 25° – 70° . According to the measurements, there are large variations in reflectivities as a function of the incident angle. TK THz RAM has the lowest specular reflectivity with most of the tested frequencies, being between $-50\dots -40$ dB in most cases. TERASORB-500 and FIRAM-500 are optimised for 500 GHz and above, and they clearly work better at 500–600 GHz than at 200–400 GHz. The flat side of the Eccosorb VFX-NRL-2 shows large variations in reflectivity due to some internal resonances, and is quite unpredictable in an antenna test range. The carpet materials (except Etola synthetic) have reflectivities below -15 dB in most cases.

Non-specular scattering measurements from the materials are presented in Chapter 5. The bistatic test bench was modified to allow continuous receiving angle sweep over 0° – 90° while the incident angle remains fixed. Tests were carried out at 300 and 400 GHz with three fixed incident angles of 26.5° , 45° , and 63.4° . The receiving angular ranges were 22.5° – 90° , 5° – 90° , and 0° – 90° , respectively. According to the measurements, the TERASORB-500 and FIRAM-500 with horizontal grooves have the best non-specular performance. The performance of these materials is consistent and predictable over the full angular range. In most tested cases, TK THz RAM features a sharp dip in scattered power close to the specular direction, and considerably higher lobes around this direction. The angular scattering pattern from TK THz RAM consists of sharp resonant-like minima and maxima.

In order to be confident about the far-field assumption in the measurements, a linear sweep of the receiving distance was performed at 300 GHz. The test showed that the ripple in reflectivity due to changing distance is about ± 1 dB, and most of the near-field components radiated by the absorbers are indeed decayed.

Finally, it can be concluded from the measurements that TK THz RAM has the best performance in applications where scattering only in the specular direction is of interest. The symmetrical nature of the pyramidal surface also permits operation on both the vertical and the horizontal polarisations without adjusting the absorbers. The findings of this report agree with the bistatic work presented earlier in [23] for microwave pyramidal absorbers. The pyramidal absorber works as an incoherent scatterer and has very wide angular scattering spectrum. The incoherent scattering from the pyramid tips is aggravated by the small size of the individual tiles and difficulties in aligning them with each other. Further, sharp grating peaks are observed in the angular spectrum of TK THz RAM as in [8] when the plane of incidence is parallel to the pyramid needle rows. The grating effect can be minimised by rotating the absorber around its surface normal.

TERASORB-500 and FIRAM-500 are the best if only one polarisation is used, and the scattered power into the surroundings should be minimised. The material panels can be rotated and tilted according to the used polarisation and the range geometry in order to provide scattering minima in the directions of most interest. Modeling and measurements of bistatic scattering from wedge absorbers at microwave frequencies are reported in [24]. The wedge absorber works as a coherent scatterer and has a clearly defined scattering pattern around the specular direction which drops off rapidly when moving to higher/lower angles.

Eccosorb VFX-NRL-2 with its large pyramids performs better than the flat side included in these tests by increasing the number of reflections. The low cost carpet materials with their better than -15 dB reflectivity can be used to reduce backscatter in a large antenna test range.

ACKNOWLEDGMENTS

The hologram CATR project is partly funded by ESA/ESTEC (Contract No. 13096/NL/SB), Tekes (Finland), and the Academy of Finland. The author wishes to thank Mr. Eino Kahra from the Radio Laboratory workshop for making the mechanical constructions and Dr Neal Erickson for suggestions concerning the measurements. The support received from the Nokia Foundation for the author's dissertation work is also greatly appreciated.

REFERENCES

- [1] P.R. Foster, D. Martin, C. Parini, A.V. Räsänen, J. Ala-Laurinaho, T. Hirvonen, A. Lehto, T. Sehm, J. Tuovinen, F. Jensen, K. Pontoppidan, "Mmwave antenna testing techniques – Phase 2", 1996, Maas report 304
- [2] E.F. Knott, J.F. Shaeffer, M.T. Tuley, *Radar Cross Section*, 2nd Edition, Artech House, Inc., Norwood, MA., USA, 1993, 611 pages
- [3] M.I. Skolnik, *Radar Handbook*, McGraw-Hill, Inc., New York, NY., USA, 1970
- [4] S. Janz, D.A. Boyd, R.F. Ellis, "Reflectance characteristics in the submillimeter and millimeter wavelength region of a vacuum compatible absorber", *International Journal of Infrared and Millimeter Waves*, Vol. 8, No. 6, 1987, pp. 627–635
- [5] B.E. Prewer, B. Milner, "Radiation absorber and method of making it", *U.S. Patent # 4,942,402*, Jul. 17, 1990
- [6] R.H. Giles, A.J. Gatesman, J. Fitzgerald, S. Fisk, J. Waldman, "Tailoring artificial dielectric materials at terahertz frequencies", *Proceedings of the 4th International Symposium on Space THz Technology*, Apr. 1993, Los Angeles, CA., USA
- [7] R.H. Giles, J.C. Dickinson, J. Waldman, W.E. Nixon, "Evaluation of submillimeter-wave anechoic materials at 500 GHz", *Project Report*, Submillimeter Technology Laboratory, University of Massachusetts Lowell, Feb. 1995, 20 pages
- [8] T.O. Klaassen, M.C. Diez, J.H. Blok, C. Smorenburg, K.J. Wildeman, G. Jakob, "Optical characterization of absorbing coatings for sub-millimeter radiation", *Proceedings of the 12th International Symposium on Space THz Technology*, Feb. 2001, San Diego, CA., USA, pp. 400–409
- [9] K.L. Ford, B. Chambers, "Tunable single layer phase modulated radar absorber", *Proceedings of the 11th International Conference on Antennas and Propagation*, 17–20 Apr., 2001, Manchester, UK, pp. 588–592
- [10] A.A. Abdelaziz, "A novel technique for improving the performance of Salisbury screen", *Proceedings of the 17th URSI National Radio Science Conference*, Feb. 22–24, 2000, Minufiya University, Egypt, pp. C27/1–8
- [11] B. Chambers, "Symmetrical radar absorbing structures", *Electronics Letters*, Vol. 31, No. 5, 1995, pp. 404–405

- [12] B. Chambers, A. Tennant, "Design of wideband Jaumann radar absorbers with optimum oblique incidence performance", *Electronics Letters*, Vol. 30, No. 18, Sept. 1994, pp. 1530–1532
- [13] F. Terracher, G. Berginc, R. Guynemer, "Thin electromagnetic absorber using frequency selective surfaces", *Proceedings of the 2000 IEEE International Symposium on Antennas and Propagation*, 16–21 July, Salt Lake City, UT, USA, Vol. 2, pp. 846–849
- [14] Emerson&Cuming Microwave Co., "Microwave absorber quick reference list", http://www.eccosorb.com/quick_reference.asp
- [15] Emerson&Cuming Microwave Co., "ECCOSORB® VHP-NRL VERY HIGH PERFORMANCE BROADBAND PYRAMIDAL ABSORBER", <http://www.eccosorb.com/catalog/anechoic/VHP.asp>
- [16] S. Chakravarty, R. Mittra, N.R. Williams, "On the application of the microgenetic algorithm to the design of broad-band microwave absorbers comprising frequency-selective surfaces embedded in multilayered dielectric media", *IEEE Transactions on Microwave Theory and Techniques*, Vol. 49, No. 6, Jun. 2001, pp. 1050–1059
- [17] P.L.E. Uslenghi (editor), *Electromagnetic Scattering*, Academic Press, Inc., New York, NY., USA, 1978, 801 pages
- [18] E.K. Miller, "A selective survey of computational electromagnetics", *IEEE Transactions on Antennas and Propagation*, Vol. 36, No. 9, Sept. 1988, pp. 1281–1305
- [19] P.H. Pathak, R.G. Kouyoumjian, "An analysis of the radiation from apertures in curved surfaces by the geometrical theory of diffraction", *Proceedings of the IEEE*, Vol. 63, No. 11, Nov. 1974, pp. 1438–1447
- [20] R.G. Kouyoumjian, P.H. Pathak, "A uniform geometrical theory of diffraction for an edge in a perfectly conducting surface", *Proceedings of the IEEE*, Vol. 63, No. 11, Nov. 1974, pp. 1448–1461
- [21] P. Goy, M. Gross, S. Caroopen, "Millimeter and submillimeter wave vector measurements with a network analyzer up to 1000 GHz. Basic principles and applications", *Proceedings of the 4th International Conference on Millimeter and Submillimeter Waves and Applications*, San Diego, CA, USA, July 20-23, 1998, 25 pages
- [22] SABOR: Software for the Analysis of Horns and Reflectors, homepage: <http://www.gr.ssr.upm.es/sabor.htm>
- [23] B.T. DeWitt, W.D. Burnside, "Electromagnetic scattering by pyramidal and wedge absorber", *IEEE Transactions on Antennas and Propagation*, Vol. 36, No. 7, July 1988, pp. 971–984

- [24] C.-F. Yang, W.D. Burnside, R.C. Rudduck, “A doubly periodic moment method solution for the analysis and design of an absorber covered wall”, *IEEE Transactions on Antennas and Propagation*, Vol. 41, No. 5, May 1993, pp. 600–609